# STM/STS INVESTIGATIONS OF TOPOLOGICAL SURFACE STATES ON Sb FILMS

**YAO GUANGGENG**

**NATIONAL UNIVERSITY OF SINGAPORE**

**2012**

# STM/STS INVESTIGATIONS OF TOPOLOGICAL SURFACE STATES ON Sb FILMS

**YAO GUANGGENG**

*(B.Sc, SHANDONG UNIV)*

A THESIS SUBMITTED

FOR THE DEGREE OF DOCTOR OF PHILOSOPHY

DEPARTMENT OF PHYSICS

NATIONAL UNIVERSITY OF SINGAPORE

2012

# ACKNOWLEDGEMENTS

It is my great pleasure to take this opportunity to thank those who have helped me to complete this thesis. Their support, assistance and encouragement are extremely precious to me at every stage of this long and enduring journey.

First and foremost, I would like to sincerely thank my main supervisor, Associate Prof. Wang Xue-sen, for his indispensable guidance, constant support and consistent encouragement throughout my PhD life. He led me into the fantastic world of nanoscience with his excellent expertise, wide knowledge and logical way of thinking. Prof. Wang always offered me many constructive suggestions and guidance every time when I came across failures or difficulties on the challenging road of exploration. With greatest diligence and patience, he always managed to open my mind through inspiring discussions of experiment results.

I am also grateful to my co-supervisor, Prof. Wu Yihong, for his generous and continuous support in the past four years. I am deeply impressed by his hard work and persistent help.

I would like to express my sincerest gratitude to Dr. Pan Feng, from whom I have benefited tremendously. Not only did Dr. Pan teach me the experimental skills involved in the UHV-STM system, but he also gave me lots of advice and stimulated me to make greater efforts to fulfill my project. Also, my sincere gratefulness is directed to Mr. Xu Wentao and Mr. Luo Ziyu. They are excellent group colleagues who have given me generous support, inspiring discussions and invaluable suggestions. In particular, the calculated data in this thesis were produced by Dr. Pan and Mr. Luo. I also sincerely thank Dr. Chu Xinjun who introduced me to the lab and taught me STM techniques.

Much appreciation also goes to Prof. Chen Wei for many constructive suggestions and interesting discussions on my research project. Furthermore, magnetic molecules used in the experiments of this thesis were supported by him.

My sincere gratefulness is also directed to other group members and all my friends in NUS. To Dr. Sun Jiatao, Dr. Qi Dongchen, Dr. Ou Hongwei, Dr. Lu Yunhao, Dr. Chen Shi, Dr. Xie Xianning, Dr. Chen Lan, Mr. Zhou Miao and Dr. Huang Han for their kind support and fruitful discussions; to Chen Xiao, Yuzhan, Junpeng, Hongwei, Yingying, Fusheng, Lanfei, Huihui, Yinghui, Cao Liang, Tianchao, Hongying, Chen Yu, Yanan, Wang Xiao, Mr. Ho and Mr. Wong for their cooperation and help.

Personally, I am appreciative to my parents for their everlasting love and unconditional understanding since I was born; to my brother who has been always selfless and supporting our parents. I also offer my honest thanks to my beloved fiancée, Qian, who has been always thoughtful to give me strength for the completion of the thesis.

Due to the limited space, I hereby express my deep appreciation to all the supportive people that I do not mention. Last but not the least, I would like to thank National University of Singapore for offering financial support to my PhD research.

# TABLE OF CONTENTS

## Chapter 2 Experimental setup and substrate description................... 33

## Chapter 3 STM/STS investigations of Sb (111) thick films................. 57

# ABSTRACT

Motivated by the unique electronic properties of Sb and its fascinating potential in the area of topological insulators (TIs), in this thesis, the topologically nontrivial Sb films were investigated using *in-situ* STM and STS. Specifically, the two surfaces of Sb films as well as the interaction between them play a vital role in determining the topological property of the material. Since one surface of Sb is next to vacuum and the other is next to the substrate, this substrate-film-vacuum system is worth investigating in three aspects, which construct the three main topics of this dissertation and will be listed as follows.

The first aspect is the analysis of topological properties of surface states (SSs) solely from the upper surface. In this case thick films which are bulk-like are needed. Then two types of defects, i.e. step edges and defects on terraces, were chosen to investigate 1D and 2D scatterings on the upper surface. According to the FT-STS method, the topological suppression for scatterings between opposite spin directions can be revealed. Besides, DFT simulations of the scattering patterns are consistent with the experimental results. Based on these two methods, the SSs of Sb(111) thick films can be confirmed as topological SSs (TSSs) which possess great backscattering suppression. Moreover, the magnetic response of TSSs on Sb(111) was also investigated by depositing magnetic molecules MnPc, but turned out to be unchanged

even in a high coverage magnetic molecular density, indicating that MnPc molecules may not break the local TR symmetry as expected.

The second aspect is the involvement of the lower surface. When the film is thin enough, the wavefunctions of the lower SSs are more spread over the whole films and couple easily with those on the upper surface. We firstly developed the growth method for Sb(111) ultrathin films using the cracked Sb source. Then using the FT-STS method again, we prove that on 9BL Sb thin films, part of SSs degenerate to quantum well states (QWSs) and lose their topological properties. Besides the ***k***-dependent diminishing process for the spin polarization from $\bar{\Gamma}$ to $\bar{\mathrm{M}}$, on several representative thicknesses, the evolutionary process of diminishing spin polarization from thick to thin films was also revealed. Additionally, STS measurements on ultrathin Sb(111) films from 6BL to 11BL were performed to investigate the subtle evolution of band structures.

The third aspect is the involvement of the substrate, because the substrate, especially those with large polar surfaces, might also play an important role in determining the physical properties of the upper structure. Since the CdSe(0001) polar surface may induce a larger electrical field, it can subsequently lead to new physical properties for the TI materials on top. Hence, the growth of CdSe on Si(111)-$\sqrt{3}\times\sqrt{3}$:Bi-β was investigated using LEED and STM. The growth method for the atomic flat CdSe(0001) films was shown based on a two-step growth procedure. The kinetic growth process of

CdSe(0001), and detailed analysis of the surface reconstruction were performed, indicating the Cd-vacancy 2×2 reconstruction is the energetically favorite configuration for this polar surface. This interesting surface might serve as the proper substrate for further investigations of TI materials.

# LIST OF TABLES

# LIST OF FIGURES

# ABBREVIATIONS

| | |
|---|---|
| 1D | one-dimentional |
| 2D | two-dimensional |
| 3D | three-dimentional |
| AES | Auger electron spectroscopy |
| ARPES | angle-resolved photoemission spectroscopy |
| BZ | Brillouin zone |
| CEC | constant energy contour |
| DFT | density functional theory |
| FT-STS | Fourier-transform scanning tunneling spectroscopy |
| LDOS | local density of states |
| LEED | low-energy electron diffraction |
| QCE | quantum confinement effect |
| QPI | quasiparticle interference |
| QSH | quantum spin Hall |
| QWS | quantum well state |
| RT | room temperature |
| SIA | structure inversion asymmetry |
| SOC | spin-orbit coupling |
| STM | scanning tunneling microscopy |
| STS | scanning tunneling spectroscopy |
| TI | topological insulator |
| TR | time reversal |
| TSS | topological surface state |
| UHV | ultrahigh vacuum |

# Chapter 1

# Introduction

In solid-state physics, a bulk crystal is usually treated as a system whose electronic structures are dominated by a periodic potential due to the regular arrangement of ion cores, while its dimensional boundaries have a negligible effect on that. However, since the crystal order is interrupted there, we can still expect that many mechanical, electronic, magnetic and chemical properties near the boundaries may vary from those of bulk. Specifically, the boundaries of solids with vacuum or gas phase are usually referred to as **surfaces**, while those with other solid materials are called **interfaces**. **Surfaces/interfaces** can induce stress, scatter carriers, and generate additional electronic states as well as fast channels of atomic migration, and hence are good or bad depending on our purposes, but in no way trivial. That’s why Wolfgang Pauli gave the famous comment: "God made solids, but surfaces (and interfaces) were the work of the devil." Take the electronic properties near the surface between crystals and vacuum as an example (which is an appropriate physical picture of this PhD project), we can easily find out the dramatic influence of that surface, which tunes the electron density to spill into vacuum in a smooth decreasing manner as shown in Fig. 1.1[1], based on the simple jellium model where the positive ion cores are smeared out and replaced by a uniform background charge density.

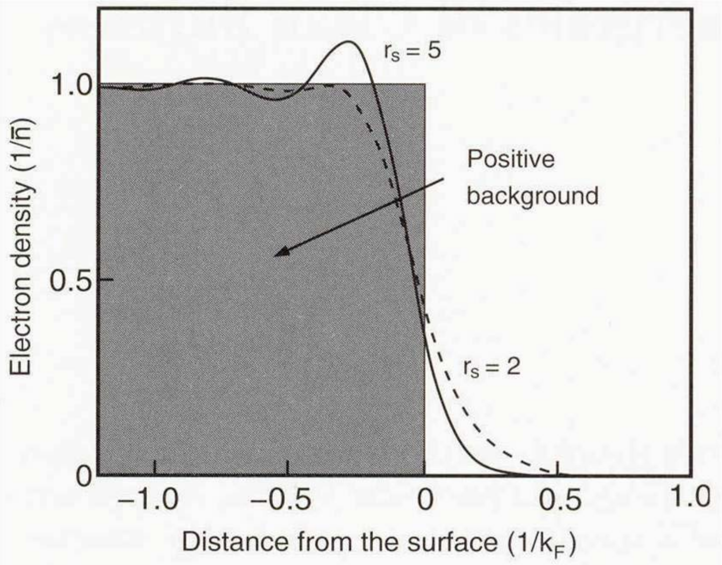

**Fig. 1.1** The self-consistent charge density near metal surface for $r_S$=2 and $r_S$=5 (reprinted from Ref. [1] by permission of the American Physical Society). Here $r_S$ is the electron density parameter defined as $\frac{4\pi}{3}(r_s a_0)^3 = 1/\bar{n}$, where $\bar{n}$ is the average ion charge and $a_0 = 0.529\,\text{Å}$ is the Bohr radius. The model is uniform positive background one, i.e. the jellium model.

Furthermore, surfaces/interfaces become more significant when the size of the crystal reduces. For example, when at least one dimension of the crystal approaches the electron's wavelength, complicated and interesting physical behaviors will show up, simply because electrons here feel not only the periodic potential but also effects of surfaces/interfaces, which can drastically restrict the allowed electron wavefunctions inside the crystal. This kind of confinement gives rise to the quantum confinement effect (QCE) that can lead to dramatic changes in properties such as surface energy[2,3], Hall effect[4,5], superconducting transition temperature[6,7], conductivity[8,9] and chemical reactivity[10,11].

The concept of QCE is essential also in another important research field called nanotechnology, which usually deals with nanomaterials with sizes ranging from 1nm to 100nm in one, two or even three dimensions, including nanowires, nanotubes, nanorods, ultrathin films, 2D islands, clusters and nanocrystallites. The realization of many surface-related physical properties in surface science becomes only available starting from 1960s with the advent of ultrahigh vacuum (UHV) and surface sensitive physical methods, and obviously cannot circumvent the interdependent relationship with nanoscience and nanotechnology. Till now, a whole arsenal of techniques is available to study the novel properties unprecedentedly that great scientists had in mind but were experimentally not yet accessible in their days. This project provides systematic studies of *in-situ* nanostructure growth and characterization mainly by one of those techniques, scanning tunneling microscopy (STM), to reveal the “plenty of room at the bottom”, as Richard Feynman anticipated in 1959.

The following sub-sections provide an overview of motivation, a general introduction to topological insulators, which are the key parts of this project, and the growth theory of materials as well as a synopsis of this thesis at last.

## 1.1 Motivation

As prototype model systems, nanostructures of various materials, such as semiconductors, semimetals and metals, deposited on semiconductor surfaces have attracted intensive attention due to their richness in condensed matter physics and potential applications in the practical field. Moreover, the characterization and controllability of nanostructures deposited on low index surfaces of Si, particularly (111) and (100), are explored intensively owing to the well-known roles of Si played in mass-producible device architecture. As the growth largely depends on the balance within various adsorbate-adsorbate and adsorbate-substrate interactions, nanostructures with different properties can be fabricated by changing combinations of adsorbates and substrates. Moreover, nanostructures on inert substrates are of particular interest since nearly free-standing nanostructures can be synthesized on such substrates, serving as model catalysts, quantum dots, and single-domain magnets among others. Since Si has relatively large surface energy, e.g. Si(111) still has 1.45 $J/m^2$ even after 7×7 reconstruction[12,13], the strong substrate effect causing changes in morphology and electronic structures of studied nanomaterials is undesirable for understanding their intrinsic physical properties. As a result, passivation of the widely used yet active surfaces is highly demanded. Here, the Si(111)-$\sqrt{3}\times\sqrt{3}$:Bi-β surface[14-18] is chosen as the basic substrate for achieving various nanostructures. The detailed descriptions of this substrate will be covered in Chap. 2.

## 1.2 Topological insulators: Theory and experiment

It is always a significant goal in condensed matter physics to search for new phases of matter, including insulating phases. Normally, an insulator, which is defined as a material lack of electrical conduction, has been best explained by the band theory of solids as one huge triumph of quantum mechanics in 20th century. In the past few years, one new kind of insulators called topological insulator (TI), whose band structure is topologically different from ordinary insulators, has been theoretically predicted and soon experimentally realized. A TI has an energy gap in the bulk but gapless states along edges or surfaces in 2D or 3D cases, respectively. These exotic states are a consequence of the topological order in the bulk bands, and offer lots of potential not only in the fundamental condensed matter physics area for realization of relativistic particles such as axions, dyons, imaging monopoles and Majorana Fermions, but also in the practical field for spintronic applications and error-tolerant quantum computing. In this part a general introduction to this new state will be covered, from both its theoretical origins and experimental realization.

### 1.2.1 Theory on topological insulators

#### *1.2.1.1 Phase transitions-from Landau theory to quantum Hall effect*

The mean-field theory has been used to explain successfully many kinds of phase transitions, such as the vapor-liquid transitions by van der Waals, paramagnetism-ferromagnetism transitions by Weiss, and superconducting phase transitions by Bardeen, Cooper and Schrieffer[19,20]. In 1937 Landau developed the theory of second-order phase transitions, which unifies various mean-field theories with great simplicity of formalism and interprets many fundamental phase transitions in different states of matter, e.g. crystalline solids, magnets, and superconductors. In his theory, usually a phase transition is associated with certain breakdown of symmetry. Therefore, the quantum states can be classified by the symmetries they spontaneously break[21], such as translational, rotational, and gauge symmetries, respectively, for the three quantum states mentioned above.

However, quantum Hall (QH) state[4], discovered in 1980, offered the first example of a quantum state which has no spontaneously broken symmetry. In contrast, it depends only on its topology and not on the geometry[22]. In the QH state, electrons in the 2D electron gas (2DEG) are circulated in quantized orbits caused by an external magnetic field perpendicular to the sample, which has an insulating bulk and conductive edge states, as described in Fig. 1.2(a) below. From Fig. 1.2(b), it is easy to find out that the Hall conductance follows precise quantization[23], only selecting integer values in unit of $e^2/h$, which is the quantum conductance, 3.88 μS. Its reverse can be referred as the quantum resistance, 25.8 kΩ. The total conductance is,

$$\sigma_{xy} = ne^2/h \tag{1.1}$$

where n is an integer. Furthermore, the Hall conductance is insensitive to smooth changes in material geometry as well as impurity levels. It cannot be changed unless a quantum phase transition takes place. In this sense it is topologically robust. So in the next part we need to find the origin of topology, firstly from mathematics.

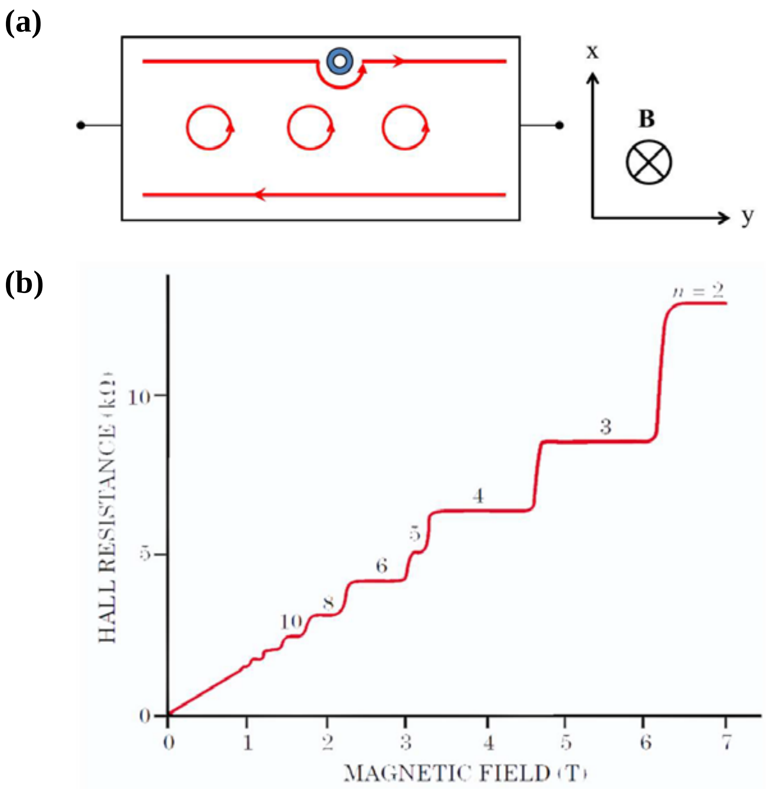

**Fig. 1.2 (a)** Schematic of classical orbits of electrons in a magnetic field for a finite-width 2DEG system, and **(b)** the integral quantum Hall effect, where 2DEG is imposed magnetic field normal to the gas plane as shown in (a). The quantized conductance as a function of gate voltage Vg can be obtained (adapted from Ref. [23] by permission of the American Physical Society).

#### *1.2.1.2 Topological invariant-from mathematics to physics*

For an object bound by surface *S*, the Gauss-Bonnet theorem gives:

$$\frac{1}{2\pi}\oint_S KdA = 2(1-g) \tag{1.2}$$

Here *K* is the local Gaussian curvature of the integrated surface *S* and *g* is an integer characterizing the genus, or more generally, the topology of the surface *S*. Therefore, we know that geometry and topology are intimately related, because the geometric components on the left side of the equation can be described as the topology on the right side, and hence the area integral of the curvature over the whole surface is “quantized”. Therefore, it is a topological invariant[24], which is defined as a quantity that does not change under continuous deformation. In this sense, the surface of an orange is topologically equivalent to that of a bowl, and so is that of a donut and a coffee cup[25,26], since those surfaces can be deformed into each other smoothly without generation of any holes.

The involvement of the concept, “topology”, from mathematics to physics emerges from a modern generalization by Shiing-shen Chern. He developed Gauss-Bonnet-Chern formula, which looks exactly like Eq. (1.2) but can be applied not only to the geometry of surfaces mathematically but also to that of eigenstates physically. Hence, the right side of the equation is still an integer and is given a new name, the Chern number, which is obviously topological because it is invariant under small deformations of the Hamiltonian in physics, just as the topological invariant under the geometric deformations in mathematics.

Specifically, by efforts of Hofstadter[27], Chern numbers were applied to the QH effect. Particularly, due to the discovery of Berry's phase[28,29] associated with the Bloch wavefunctions $|u(\boldsymbol{k})\rangle$, people realize that the quantized Hall conductance can be related to an analog of the curvature *K*, which is best understood in the Kubo formula below:

$$\frac{1}{2\pi}\int_{BZ}(\nabla\times \mathrm{A})d^2\boldsymbol{k}=n \tag{1.3}$$

Here $n$ is the Chern number. Just like a vector potential, $\mathbf{A}=i\langle u(\boldsymbol{k})|\nabla_{\boldsymbol{k}}|u(\boldsymbol{k})\rangle$ is called the Berry's connection for the state $|u(\boldsymbol{k})\rangle$. $\nabla\times\mathbf{A}$ refers to the Berry's curvature. So we can tell that the Chern invariant is the total Berry flux in the Brillouin zone (BZ), which has an explicit similarity to the description in Eq. (1.2). In this sense, the BZ and Berry's curvature $\nabla\times\mathbf{A}$ in physics play the roles of the surface *S* and local Gaussian curvature *K* in mathematics, respectively. Moreover, from the work of Thouless, Kohmoto, Nightingale, and den Nijs (TKNN)[30], we know that the Chern number *n* here is exactly the *n* in Eq. (1.1). Now, we can see that the topologically quantized physical quantities, such as the Hall conductance, can be expressed as invariant integrals over the frequency-momentum space, which are independent of small details.

### *1.2.1.3 With or without magnetic field-from QH to QSH state*

Because of the presence of the magnetic field, on one hand, it realizes the charge chirality which allows the flow of electrons along edges; however, on the other hand, it also breaks the time-reversal (TR) symmetry, leading to two negative consequences. One is that the transport properties are unrelated to spin, and this is not helpful for the advance of future devices as scientists in the field of spintronics expect. The other is that the requirement of a large magnetic field limits the real application for QH effect. So in the last few years efforts have been made to find a new class of quantum states that is invariant under TR protection. Inspiringly, the spin-orbit coupling (SOC) in 2D electron system is verified to take the role of an external magnetic field, driving spins of opposite directions counter-propagating along the edges. This close sibling of QH effect is called Quantum Spin Hall (QSH) effect, which is well developed by several theorists[31-34]. Next let us briefly introduce the evolution progress from QH to QSH states.

For a particle moving in magnetic field ***B***, which can be expressed in terms of vector potential, we know the Hamiltonian of the system can be written as

$$H=\frac{1}{2m}\left(\boldsymbol{p}-q\boldsymbol{A}\right)^2 \tag{1.4}$$

In Eq. (1.4) ***p*** is the particle momentum and ***A*** is the vector potential. Specifically, in the QH effect, the Lorentz force contributes a term proportional to $\boldsymbol{A}\cdot\boldsymbol{p}$. Choosing the coordinate as in Fig. 1.2(a), we use $\boldsymbol{A}=\frac{B}{2}(y,-x,0)$ in the symmetric gauge[33], and thus the Hamiltonian is proportional to $B(xp_y-yp_x)$.

Similarly, for a large SOC 2D electron system, due to Rashba splitting effect[35], the SOC term in the Hamiltonian is

$$H_R = \lambda_R \left( \nabla V \times \boldsymbol{p} \right) \cdot \boldsymbol{\sigma} \tag{1.5}$$

Here $\lambda_R$ is an element-dependent coefficient to describe the strength of Rashba effect, $\nabla V$ the electrical field and $\boldsymbol{\sigma}$ the Pauli matrices. Expand the equation and we can find that $H_R$ is proportional to $\lambda_R \sigma_z \left( x p_y - y p_x \right)$.

Compared with the expression in QH states, the Hamiltonian here has an explicitly similar form. In this sense, we may imagine a spin-dependent equivalent magnetic field induced by large SOC at boundaries, which, however, does not break the TR symmetry, and hence makes spin-related transport possible.

Indeed, protected by TR symmetry, the resultant 2D edge states are no longer spinless channels as those in QH states. They are robust and immune to backscattering caused by non-magnetic defects, because the directions of momentum and spin are “locked” under the TR operator, meaning if spin-up electrons move forward, spin-down electrons have to move backward. No longer referred as “chiral states” in QH effect, the spinful channels here are denoted “helical edge states”.

Scientists also made many efforts in search for materials for the realization of QSH effect, and the theoretical advance of this new class of quantum states was made by Kane and Mele[32], who proposed realistic models based on graphene and verified that stable helical edge states can survive in the 2D material, which are the first pioneer of 2D TI, or synonymously called the quantum spin Hall insulator (QSHI) to be understood. However, it can be achieved only if large SOC is artificially added. Then Bernevig, Hughes and Zhang predicted that a 2D TI would be realized in (Hg,Cd)Te quantum wells when the HgTe band structure is inverted[34], which was actually observed in the system[36] and further investigated[37] later. Other materials, such as one-bilayer bismuth[38,39] and the "broken-gap" type-II AlSb/InAs/GaSb quantum wells[40] are also believed to be good candidates for realizing 2D TIs. Specially, the latter one indeed has encouraging experimental implications[41]. All in all, the search for good 2D TIs has never stopped, and has become an important subject in the field of condensed matter physics.

#### *1.2.1.4 From 2D to 3D topological insulators*

In the case of QSHI, a $\mathbf{Z}_2$ invariant topological quantum number $\nu_0$ serves to distinguish 2 sub-groups of QSH states, just as the Chern number $n$ in QH states. When $\nu_0=0$ it is topologically trivial with an even number of pairs of edge states while when $\nu_0=1$ it is topologically nontrivial with odd number pairs of edge states. So a natural question was raised, i.e. can the QSHI be generalized to a 3D form? Indeed, it was proved by three theoretical groups[42-44] independently that the QSHI has a natural generalization in 3D form, where four $\mathbf{Z}_2$ invariant topological quantum numbers $(\nu_0; \nu_1 \nu_2 \nu_3)$, $\nu_i \in \{0,1\}$ are used to characterize and classify the 3D TIs. Here $\nu_0=0$ and $\nu_0=1$ are used to represent weak and strong TIs, respectively, while the extra triplet $(\nu_1 \nu_2 \nu_3)$ can be interpreted as Miller indices of the TR invariant momenta (TRIM) in the surface

BZ of a 3D crystal. To gain a strong SOC, heavy elements such as Au and Bi which possess large $\lambda_R$ in Eq. (1.5) are tested but proved to have $\nu_0$=0 topology. Then Fu and Kane[45] predicted that $Bi_{1-x}Sb_x$ within a certain range of $x$ when the band inversion occurs is a 3D TI, which is identified as the first 3D TI. Then driven by a simple model Hamiltonian, several materials such as $Bi_2Se_3$, $Bi_2Te_3$ and $Sb_2Te_3$, known as the "second generation"[46] of 3D TIs are theoretically predicted[47] and later experimentally confirmed[48-52] to have larger band gaps and simpler surface band structures than $Bi_{1-x}Sb_x$. It is remarkable that these common materials which are easy to fabricate and well-known for previous thermoelectric applications possess so amazing topological effects, and thus are moved to the forefront of research as the new quantum states of matter.

### 1.2.2 Experiment on topological insulators

#### *1.2.2.1 Methods*

The most direct probe for TIs is the transport measurement. Due to the existence of the bulk gap, transport should be dominated by edges (or surfaces) in 2D (or 3D) TIs at a low temperature. However, it requires extremely high quality of the tested materials, because in real TIs, the small gap and impurities of the samples usually lead to undistinguished edge (or surface) contributions from bulk states. Efforts must be made to tune the position of the Fermi level in order to extract and enhance the edge (or surface) conductance.

For 3D TIs, an alternative probe is to map the energy bands as a function of momentum parallel to the surface using angle-resolved photoemission spectroscopy (ARPES), or more precisely, by spin-resolved ARPES. By these methods, the hallmark for TIs, i.e. the nontrivial band topology, can be directly demonstrated by the gapless surface band associated with its spin textures, which supports a nonzero Berry's phase unlike ordinary large SOC materials (such as Au). One significant advantage for ARPES measurements is that using modulated photon energy, the signal of surface states (SSs) can be well isolated from that of the bulk states (BSs), because SSs do not disperse along a direction perpendicular to the surface whereas BSs do.

Another method is to employ STM/STS to characterize the local density of states (LDOS) on the 3D TI surfaces. Previous studies show that using Fourier-transform scanning tunneling spectroscopy (FT-STS), the detailed scattering processes on noble metals[53] or superconductors[54] can be obtained. In the case of topological surface states (TSSs), the quasi-particles interference (QPI)[55-59] between states of different momentum can give us a picture of the surface band structure as well as the spin textures, hence helping us understand the origins of the topological properties in these new quantum states of matter.

#### *1.2.2.2 Previous results*

The first experimentally confirmed TI materials are (Hg,Cd)Te quantum wells[36] in

2007, which belong to a family of semiconductors with strong SOC. A sandwich structure is proposed[34], where HgTe lies between layers of CdTe. When the HgTe layer thickness $d$ is larger than a critical value $d_c$= 6.3nm, the 2D band inverts, leading to QSH states. Then this phenomenon was confirmed by two-terminal conductance measurement[36]. Although it only achieved charge-transport data and could not illustrate the spin accumulation properties, it successfully verifies the existence of edge states.

In 2008, the first 3D TI to be identified experimentally[60,61] was $Bi_{1-x}Sb_x$ within a certain range of $x$. On (111) surface of $Bi_{0.9}Sb_{0.1}$, there are four TRIM in the surface BZ, which are $\overline{\Gamma}$ and three equivalent $\overline{\mathrm{M}}$ due to the three-fold symmetry. ARPES measurements[58] show its band structure along $\overline{\Gamma}-\overline{\mathrm{M}}$ has five surface band crossings between $\overline{\Gamma}$ and $\overline{\mathrm{M}}$, i.e. an odd number of surface band crossings between these two TRIM, which is direct evidence for $Bi_{1-x}Sb_x$ being a strong 3D TI with the predicted (1;111) topological class. Besides, the spin polarizations of the surface band were measured by spin-resolved ARPES[61] later, giving a further confirmation on the band topology.

Furthermore, the scatterings on the $Bi_{1-x}Sb_x$ surface were investigated using FT-STS[55], and were found to follow the spin-dependent channels due to protection of TR symmetry. However, a crucial challenge for $Bi_{1-x}Sb_x$ is that it has complicated surface bands where only one out of five carries the topological quantum number. Additionally, it has a small band gap and alloying disorder, which make it difficult to manipulate the charge carriers in the material for realizing high quality devices. Therefore, scientists have been searching for new TI materials with fewer yet odd-numbered surface band crossings and larger band gaps, leading to the discovery of the second generation of 3D TIs.

Obviously, the simplest number for odd-time crossings is, just one, which makes $Bi_2Se_3$, $Bi_2Te_3$ and $Sb_2Te_3$ come into our sights. In 2008, Hasan’s group discovered the hallmark signature of TIs, i.e. one single Dirac cone in the SSs of $Bi_2Se_3$(111) surface BZ using both ARPES and first-principles calculations[48]. One significant advantage of $Bi_2Se_3$ is that the band gap is as large as 0.3 eV, and thus can support the TI phase at room temperature (RT) from the viewpoint of applications. Another advantage is that, since $Bi_2Se_3$ is stoichiometric, the crystal has the naturally better quality than the alloy $Bi_{1-x}Sb_x$. So it can provide much stronger signals in the ARPES measurements, especially for testing the robustness of TSSs to artificially induced disorder and impurities. Therefore, due to its good preparation accessibility and simplest surface spectrum, so far $Bi_2Se_3$ has been used as the most suitable 3D TI materials to explore many exotic properties that TIs may possess, such as the response to magnetism: the observation of Landau quantization[62], the broken TR symmetry due to surface-doped magnetic layers[63], weak antilocalization (WAL) in TI thin films[64], Aharonov-Bohm (AB) effect[65] and Kondo effect[66] in TI nanorribons; and the response to optics, including terahertz magneto-optical Kerr measurements[67] and nonlinear optical measurements[68] for examinations on the existence of TSSs. Besides, unexpected superconductivity in Cu-doped $Bi_2Se_3$[69] and the phase transition towards 2D limit[70] have also been experimentally explored. To conclude, the tremendous discoveries in $Bi_2Se_3$ by all these different techniques have been driving the advance of TI areas and will continue to develop new directions.

In addition, quite different from $Bi_2Se_3$, $Bi_2Te_3$ has a hexagonal warping Fermi surface[49] rather than a circular one away from the Dirac point. The reason is that higher order terms proportional to $k^3$ are needed in the effective surface Hamiltonian[71], while in the simplest case like $Bi_2Se_3$, only $k$ terms are required[72]. Interestingly, the hexagonal deformation of the Fermi surface opens up new scattering channels, making the enhanced scattering patterns observable using STM/STS[56,57,73].

Moreover, in $Sb_2Te_3$, since it has a relatively weak bonding between Sb and Te, Sb vacancies and antisite defects can easily form. Therefore, usually $Sb_2Te_3$ is heavily $p$ doped with its Fermi energy buried in the bulk VB. Nevertheless, the single Dirac cone still exists[50], and recently the Landau quantization[52] was reported in this TI material.

Since the topological properties originate from the SOC-induced inverted band structures, scientists have been searching for new TIs among covalent compounds with narrow band gaps and heavy atoms. Based on this principle, many new TIs have been proposed, such as thallium-based III-V-$VI_2$ ternary chalcogenides. These materials, like $TlBiQ_2$ and $TlSbQ_2$ with Q=Te, Se, S, have the same rhombohedral crystal structure, and indeed, part of them have been confirmed experimentally to be 3D TIs[74,75].

Recently, quaternary chalcogenides ($I_2$-II-IV-$VI_4$) and ternary famatinite ($I_3$-V-$VI_4$) compounds[76,77] are examined to be 3D TIs by first-principle calculations as well. Due to the involvement of partially filled d- and f-electrons in these compounds, interplay of magnetism and superconductivity with the topological order becomes possible.

#### *1.2.2.3 Another look at Sb*

From the introduction above, we learn that as the parent compound in $Bi_{1-x}Sb_x$, Sb plays an important role in the development of TIs. Although the bulk is semimetal, Sb, especially in the form of thin films, is still worth exploring in this field. That's because firstly, Sb has a single Dirac cone (see detailed introduction in Chap. 3), which makes its SSs topologically nontrivial. So it belongs to the (1;111) topological class. This is exactly why Sb is introduced in $Bi_{1-x}Sb_x$ in which Bi is topologically trivial. In this sense, Sb alone is good enough for investigating TI-related properties. Secondly, the Dirac cone it possesses is rather distorted, which can create various scattering channels, where the spin information might be extracted, helping us understand the fundamental role the spin plays in the new quantum states. Thirdly, thin films with larger surface-to-volume ratios than bulk materials can manifest the surface effect significantly, giving a larger contribution from the surface and making it more observable. Fourthly, taking advantage of QCE, the negative indirect bandgap in bulk Sb can be tuned and transformed into a positive one, offering the possibility of making Sb a real TI. Lastly, compared with the well-studied compound TIs such as $Bi_2Se_3$, Sb is a single-element simple system, and hence Sb thin films may provide a straightforward demonstration for topological properties without considering the residual bulk carriers from self-doping states[49,78,79] or spatial fluctuations of charge and spin helicity[80].

In summary, both the experimental and theoretical progress in the investigations of TIs is answering and simultaneously, raising essential questions regarding exotic properties associated with the new quantum states in the field of condensed matter physics. Based on that, a variety of applications will hopefully realize the topological effect without the restrictions by extreme physical conditions such as very low temperature, reduced dimensionality and strong magnetic field. To access these fundamental and beneficial properties in this area, Sb is capable of offering a simple yet effective system, which has various advantages over other materials. Hence, a systematic study of Sb by STM/STS will be the main topic of this thesis, making effort to comprehensively observe, to thoroughly analyze, and to accurately understand the underlying principles.

## 1.3 Growth of thin films

From the discussion above, we know that TI materials of good quality are the cornerstone to obtain well-defined topological edge/surface states for the realization of TIs’ exotic properties, which needs the delicate growth methods to minimize the bulk carriers. Therefore, in the next part, the material growth theory is generally introduced, with emphasis placed on thermodynamic and kinetic properties in the growth processes, which are commonly applied in this project.

### 1.3.1 Thermodynamics in growth processes

One main motivation for the development of the vacuum system is the production need of various high-quality thin films, such as those on surfaces of mirrors and sunglasses in our daily life, where thin metallic film coatings on top are used for optical purposes. Most such films are examples of polycrystalline island growth on amorphous substrates. However, single crystalline films on a range of single crystal substrates are also highly required for more fundamental reasons, such as understandings of clean surfaces, surface reactions with adsorbates and basic growth principles. So using laboratory-based methods as the initial step, efforts have been made extensively to perform the studies in this field.

Specifically, sometimes a thin film is required to grow in a unique lattice orientation with respect to the substrate crystal, and that is called epitaxial growth, which needs a relatively close matching between the lattices of the substrate and deposited materials. From the view of thermodynamics, a uniform film growth needs a strong bonding between the two materials. These requirements can be met easily in homoepitaxy where the substrate and deposited materials are identical. In heteroepitaxy where they are different, three different growth modes can be classified, i.e. layer-by-layer growth (Frank-van der Merwe mode), islanding growth (3-D mode or Volmer-Weber mode), and layer-by-layer followed by islanding growth (Stranski-Krastanov mode). When the lattice mismatch is small and the interface binding is strong, the film follows layer-by-layer growth. If the interface bonding is weak, the deposited material grows in 3D islanding mode. When there is interface stress between the deposited material and a strong-bonding substrate, after a critical thickness by layer-by-layer growth, the further deposited material takes the islanding growth mode. For example, the growth of Ge on Si[81] is in Stranski-Krastanov mode. The initial wetting layer formed by Ge grows in the lattice constant of Si, and thus has the elastic strain, which raises strain energy with the film thickness. The strain energy is released by formation of 3D islands at certain point, and eventually by formation of misfit dislocations at lager thickness. Fig. 1.3(a), (b) and (c) illustrate the three growth modes, respectively.

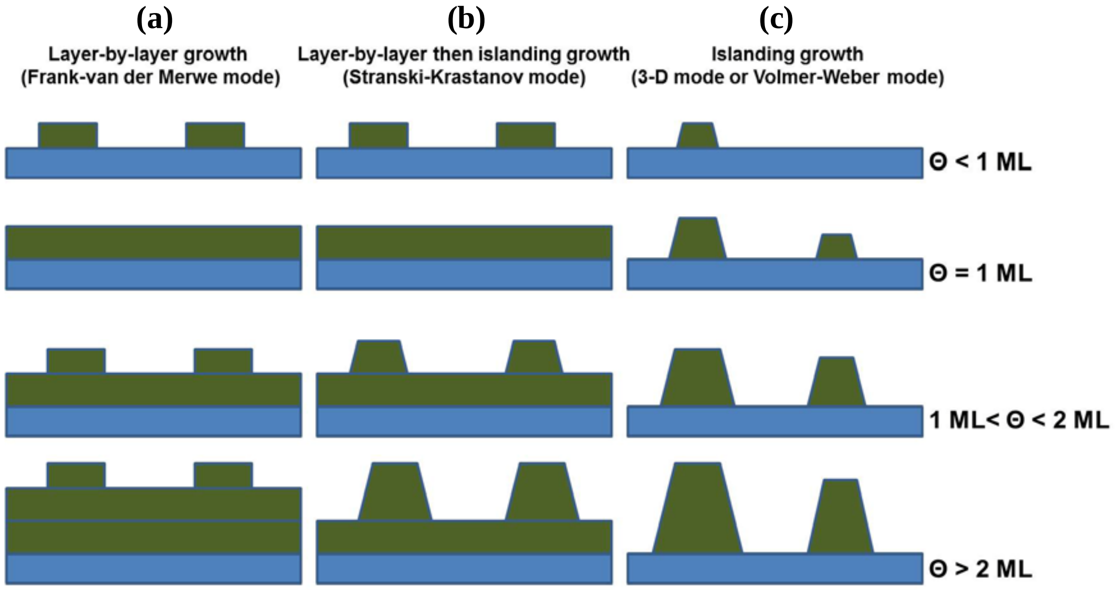

**Fig. 1.3** Growth modes under thermodynamic equilibrium condition: **(a)** layer-by-layer growth (Frank-van der Merwe mode), **(b)** layer-by-layer followed by islanding growth (Stranski-Krastanov mode), and **(c)** islanding growth (3-D mode or Volmer-Weber mode). The coverage is represented by Θ.

### 1.3.2 Kinetics in growth processes

Many growth processes, however, are not in thermodynamic equilibrium due to different depositing fluxes and diffusion speeds. For example, growth carried out in ultra-high vacuum (UHV) is usually under the pressure at around $10^{-10}$ Torr., while the equilibrium vapor pressure of the deposition flux is much higher than that. Therefore, we need to consider the detailed kinetic processes, such as adsorption, diffusion, desorption, nucleation of atoms on terraces and the inter-layer migration of them across steps. The first several factors determine the lateral uniformity of the film, and the last one leads to 2D or 3D growth modes. Next we will discuss the processes in sub-monolayer and multilayer regimes, respectively.

As the first step of growth, the sub-monolayer regime begins with the landing of deposited atoms. They migrate on the surface until arriving at stable trapping sites with stronger binding energy, such as step edges. Sometimes they may bond together to form a cluster, which also migrates on the surface but is more immobile than the individual atom. If atoms in the cluster do not re-evaporate for a period of time, additional atoms may attach and eventually form a stable island. The shape of the island is related to positions of attached atoms, which is ultimately determined by the temperature and deposition flux. The higher the substrate temperature is, the more thermal energy the deposited atoms have. So they can overcome the diffusion barrier to form a compact shape. In the same sense, lower flux can allow atoms to sufficiently migrate to kink sites before others arrive, leading to a more compact shape. In contrast, at a lower temperature and higher flux, the atoms hit and subsequently stick to the island but with little further motion, which leads to a ramified fractal shape.

When the deposition amount increases, the probability of atoms landing on an existing island becomes significant. After that, they may migrate to island edges or the top of the first-layer to form the second-layer island. Here the concept of Ehrlich-Schwoebel (ES) barrier is introduced, which indicates the additional barrier for an adatom jumping down a step edge due to fewer neighbors than that at a regular terrace site. If the ES barrier is large, atoms prefer intra-layer transport which results in the 3D, or multilayer growth mode, while if it is small, atoms prefer inter-layer transport which results in the 2D, or layer-by-layer growth mode. Shown in Fig. 1.4(a), (b) and (c) are three kinetic growth modes, i.e. step-flow growth, layer-by-layer growth, and multilayer growth. Specifically, to achieve a smooth film, step-flow growth is desirable since deposited atoms can quickly migrate to step edges before island nucleation, even in a system with a higher ES barrier.

To conclude, in this project, to achieve nanostructures of good quality is the first step for further investigations. So during the growth process, the substrate temperature and deposition flux are precisely controlled, leading to formation of the desired thin films, which unambiguously demonstrates the importance of kinetics principles.

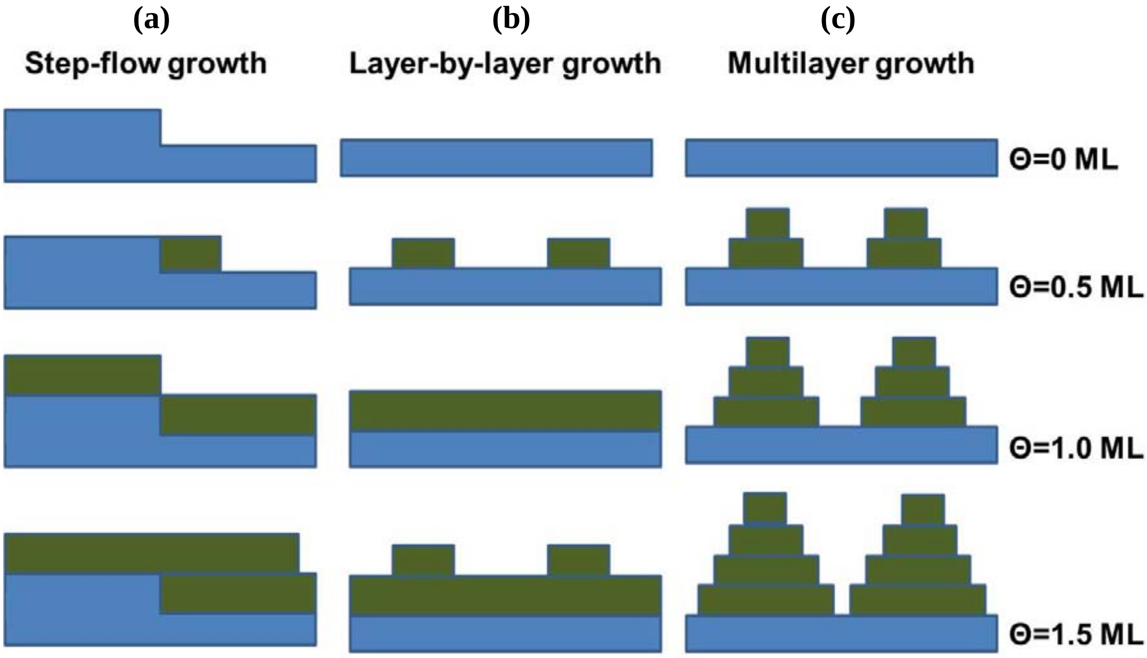

**Fig. 1.4** Three kinds of kinetic growth mode. **(a)** step-flow growth, **(b)** layer-by-layer growth, and **(c)** multilayer growth.

## 1.4 Synopsis of chapters

In Chap. 3, the results of our *in-situ* STM study of the growth of thick Sb films (up to 30BL) are given, which can be confirmed by both morphology and characteristic STS results. By two kinds of defects, i.e. step edges and atomic defects at terraces, 1D and 2D scattering patterns can be gained, showing that Sb(111) thick films indeed have TSSs. The examination of the exotic properties will be discussed in detail using the FT-STS method (covered in Chap. 2).

In Chap. 4, a new deposition method for formation of Sb ultrathin films using a cracking Sb source is introduced. We show that only after cracking of $Sb_4$ flux through a reflecting Ta foil of high temperature (900$^{o}$C), the outgoing flux can have an increasing composition of $Sb_2$ molecules and Sb atoms while a decreasing composition of $Sb_4$ molecules. This is ideal for obtaining Sb thin films since $Sb_4$ molecules favor the multiplayer growth mode. Then the detailed comparison of the two resultant structures will be illustrated. The achievement of Sb ultrathin films opens the possibility of studying the coupling of TSSs on the opposite two surfaces using STM/STS, and of characterizing thickness dependent band structures of Sb(111) films using ARPES in the future. Next I will present the scattering patterns of TSSs on Sb (111) ultrathin films, identifying origins of distinct scattering channels which are in excellent agreement with our theoretical simulations. The dramatic changes of QPI patterns indicate that unlike the intra-surface interference in thick films as described in Chap. 3, here in ultrathin films the inter-surface interference is dominant.

In Chap. 5, to better understand the substrate effect in TI materials, I will introduce a strong polar surface of II-VI semiconductor material CdSe, which is quite different from the inert surface of Si(111)-$\sqrt{3}\times\sqrt{3}$:Bi-β. The kinetic growth process of CdSe(0001) is examined using Auger electron spectroscopy (AES), low-energy electron diffraction (LEED) and STM. Atomically smooth and single crystalline wurtzite CdSe thin films can be obtained by physical vapor deposition. A growth model can be developed which illustrates Se atoms act as the wetting layer, and dominate the initial stage. Then CdSe grows in the layer-by-layer mode along (0001) direction on this wetting layer. Besides, detailed measurements on the reconstruction of (0001) surfaces are performed, revealing the well-known 2×2 reconstruction by STM for the first time, which is in good agreement with our theoretical calculations. This material may serve as an interesting substrate for TI materials, because the effective electrical potential induced by the polar surface on that should give rise to a lager structure inversion asymmetry for Sb or $Bi_2Se_3$ above, and subsequently might remove the degeneracy of two Dirac cones on opposite surfaces, leading to more interesting and exotic properties associated with TIs.

# References

1 Lang, N. D. & Kohn, W. Theory of Metal Surfaces: Charge Density and Surface Energy. *Phys. Rev. B* **1**, 4555-4568 (1970).

2 Upton, M. H., Wei, C. M., Chou, M. Y., Miller, T. & Chiang, T. C. Thermal Stability and Electronic Structure of Atomically Uniform Pb Films on Si(111). *Phys. Rev. Lett.* **93**, 026802 (2004).

3 Czoschke, P., Hong, H., Basile, L. & Chiang, T. C. Quantum size effects in the surface energy of Pb/Si(111) film nanostructures studied by surface x-ray diffraction and model calculations. *Phys. Rev. B* **72** (2005).

4 von Klitzing, K., Dorda, G. & Pepper, M. New Method for High-Accuracy Determination of the Fine-Structure Constant Based on Quantized Hall Resistance. *Phys. Rev. Lett.* **45**, 494-497 (1980).

5 Zheng, H. Z., Choi, K. K., Tsui, D. C. & Weimann, G. Observation of Size Effect in the Quantum Hall Regime. *Phys. Rev. Lett.* **55**, 1144-1147 (1985).

6 Orr, B. G., Jaeger, H. M. & Goldman, A. M. Transition-Temperature Oscillations in Thin Superconducting Films. *Phys. Rev. Lett.* **53**, 2046-2049 (1984).

7 Guo, Y. *et al.* Superconductivity Modulated by Quantum Size Effects. *Science* **306**, 1915-1917 (2004).

8 Trivedi, N. & Ashcroft, N. W. Quantum size effects in transport properties of metallic films. *Phys. Rev. B* **38**, 12298-12309 (1988).

9 Makarov, N. M., Moroz, A. V. & Yampol'skii, V. A. Classical and quantum size effects in electron conductivity of films with rough boundaries. *Phys. Rev. B* **52**, 6087-6101 (1995).

10 Valden, M., Lai, X. & Goodman, D. W. Onset of Catalytic Activity of Gold Clusters on Titania with the Appearance of Nonmetallic Properties. *Science* **281**, 1647-1650 (1998).

11 Chen, M. S. & Goodman, D. W. The Structure of Catalytically Active Gold on Titania. *Science* **306**, 252-255 (2004).

12 Zhao, Y. F., Yang, H. Q., Gao, J. N., Xue, Z. Q. & Pang, S. J. Local dimer-adatom stacking fault structures from 3×3 to 13×13 along Si(111)-7×7 domain boundaries. *Phys. Rev. B* **58**, 13824-13829 (1998).

13 Štich, I., Payne, M. C., King-Smith, R. D., Lin, J. S. & Clarke, L. J. Ab initio total-energy calculations for extremely large systems: Application to the Takayanagi reconstruction of Si(111). *Phys. Rev. Lett.* **68**, 1351-1354 (1992).

14 Wan, K. J., Guo, T., Ford, W. K. & Hermanson, J. C. Initial growth of Bi films on a Si(111) substrate- 2 phases of √3×√3 low-energy-electron-diffraction pattern and their geometric structures. *Phys. Rev. B* **44**, 3471-3474 (1991).

15 Park, C., Bakhtizin, R. Z., Hashizume, T. & Sakurai, T. Scanning tunneling microscopy of √3×√3-Bi reconstructon on the Si(111) surfaces. *Jpn. J. Appl. Phys. Part 2 - Lett.* **32**, L290-L293 (1993).

16 Shioda, R., Kawazu, A., Baski, A. A., Quate, C. F. & Nogami, J. Bi on Si(111): Two phases of the √3×√3 surface reconstruction. *Phys. Rev. B* **48**, 4895 (1993).

17 Kuzumaki, T. *et al.* Re-investigation of the Bi-induced Si(111)-(√3×√3) surfaces by low-energy electron diffraction. *Surf. Sci.* **604**, 1044-1048 (2010).

18 Gierz, I. *et al.* Silicon Surface with Giant Spin Splitting. *Phys. Rev. Lett.* **103**, 046803-046804 (2009).

19 Feng, D. *Introduction to Condensed Matter Physics.* (World Scientific, 2005).

20 Bardeen, J., Cooper, L. N. & Schrieffer, J. R. Theory of Superconductivity. *Phys. Rev.* **108**, 1175-1204 (1957).

21 Anderson, P. W. *Basic Notions of Condensed Matter Physics.* (Benjamin/Cummings Pub. Co., 1984).

22 Avron, J. E., Osadchy, D. & Seiler, R. A Topological Look at the Quantum Hall Effect. *Phys. Today* **56**, 38-42 (2003).

23 Paalanen, M. A., Tsui, D. C. & Gossard, A. C. Quantized Hall effect at low temperatures. *Phys. Rev. B* **25**, 5566-5569 (1982).

24 Nakahara, M. *Geometry, Topology, and Physics.* 2nd edn, (Institute of Physics Publishing, 2003).

25 Qi, X.-L. & Zhang, S.-C. Topological insulators and superconductors. *Rev. Mod. Phys.* **83**, 1057-1110 (2011).

26 Hasan, M. Z. & Kane, C. L. Colloquium: Topological insulators. *Rev. Mod. Phys.* **82**, 3045 (2010).

27 Hofstadter, D. R. Energy levels and wave functions of Bloch electrons in rational and irrational magnetic fields. *Phys. Rev. B* **14**, 2239-2249 (1976).

28 Berry, M. V. Quantal phase factors accompanying adiabatic changes. *P. Roy. Soc. Lond. A-Mat.* **392**, 45-57 (1984).

29 Berry, M. Anticipations of the Geometric Phase. *Phys. Today* **43**, 34-40 (1990).

30 Thouless, D. J., Kohmoto, M., Nightingale, M. P. & den Nijs, M. Quantized Hall Conductance in a Two-Dimensional Periodic Potential. *Phys. Rev. Lett.* **49**, 405-408 (1982).

31 Kane, C. L. & Mele, E. J. $Z_2$ topological order and the quantum spin Hall effect. *Phys. Rev. Lett.* **95**, 146802 (2005).

32 Kane, C. L. & Mele, E. J. Quantum Spin Hall Effect in Graphene. *Phys. Rev. Lett.* **95**, 226801 (2005).

33 Bernevig, B. A. & Zhang, S. C. Quantum spin Hall effect. *Phys. Rev. Lett.* **96**, 106802 (2006).

34 Bernevig, B. A., Hughes, T. L. & Zhang, S. C. Quantum spin Hall effect and topological phase transition in HgTe quantum wells. *Science* **314**, 1757-1761 (2006).

35 Bychkov, Y. A. & Rashba, E. I. Properties of a 2D electron gas with lifted spectral degeneracy. *JETP Letters* **39**, 78-81 (1984).

36 Konig, M. *et al.* Quantum spin Hall insulator state in HgTe quantum wells. *Science* **318**, 766-770 (2007).

37 Roth, A. *et al.* Nonlocal Transport in the Quantum Spin Hall State. *Science* **325**, 294-297 (2009).

38 Murakami, S. Quantum Spin Hall Effect and Enhanced Magnetic Response by Spin-Orbit Coupling. *Phys. Rev. Lett.* **97**, 236805 (2006).

39 Wada, M., Murakami, S., Freimuth, F. & Bihlmayer, G. Localized edge states in two-dimensional topological insulators: Ultrathin Bi films. *Phys. Rev. B* **83**, 121310 (2011).

40 Liu, C., Hughes, T. L., Qi, X.-L., Wang, K. & Zhang, S.-C. Quantum Spin Hall Effect in Inverted Type-II Semiconductors. *Phys. Rev. Lett.* **100**, 236601 (2008).

41 Knez, I., Du, R. R. & Sullivan, G. Finite conductivity in mesoscopic Hall bars of inverted InAs/GaSb quantum wells. *Phys. Rev. B* **81**, 201301 (2010).

42 Fu, L., Kane, C. L. & Mele, E. J. Topological insulators in three dimensions. *Phys. Rev. Lett.* **98**, 106803 (2007).

43 Moore, J. E. & Balents, L. Topological invariants of time-reversal-invariant band structures. *Phys. Rev. B* **75**, 121306(R) (2007).

44 Roy, R. Topological phases and the quantum spin Hall effect in three dimensions. *Phys. Rev. B* **79**, 195322 (2009).

45 Fu, L. & Kane, C. L. Topological insulators with inversion symmetry. *Phys. Rev. B* **76**, 045302 (2007).

46 Moore, J. Topological insulators: The next generation. *Nat. Phys.* **5**, 378-380 (2009).

47 Zhang, H. *et al.* Topological insulators in $Bi_2Se_3$, $Bi_2Te_3$ and $Sb_2Te_3$ with a single Dirac cone on the surface. *Nat. Phys.* **5**, 438-442 (2009).

48 Xia, Y. *et al.* Observation of a large-gap topological-insulator class with a single Dirac cone on the surface. *Nat. Phys.* **5**, 398-402 (2009).

49 Chen, Y. L. *et al.* Experimental Realization of a Three-Dimensional Topological Insulator, $Bi_2Te_3$. *Science* **325**, 178-181 (2009).

50 Hsieh, D. *et al.* Observation of Time-Reversal-Protected Single-Dirac-Cone Topological-Insulator States in $Bi_2Te_3$ and $Sb_2Te_3$. *Phys. Rev. Lett.* **103**, 146401 (2009).

51 Wang, G. A. *et al.* Atomically smooth ultrathin films of topological insulator $Sb_2Te_3$. *Nano Res.* **3**, 874-880 (2010).

52 Jiang, Y. *et al.* Landau Quantization and the Thickness Limit of Topological Insulator Thin Films of $Sb_2Te_3$. *Phys. Rev. Lett.* **108**, 016401 (2012).

53 Petersen, L. Direct imaging of the two-dimensional Fermi contour: Fourier-transform STM. *Phys. Rev. B* **57**, R6858-R6861 (1998).

54 Hoffman, J. E. Imaging quasiparticle interference in $Bi_2Sr_2CaCu_2O_{8+\mathrm{delta}}$. *Science* **297**, 1148-1151 (2002).

55 Roushan, P. *et al.* Topological surface states protected from backscattering by chiral spin texture. *Nature* **460**, 1106 (2009).

56 Alpichshev, Z. *et al.* STM Imaging of Electronic Waves on the Surface of $Bi_2Te_3$: Topologically Protected Surface States and Hexagonal Warping Effects. *Phys. Rev. Lett.* **104**, 016401 (2010).

57 Zhang, T. *et al.* Experimental Demonstration of Topological Surface States Protected by Time-Reversal Symmetry. *Phys. Rev. Lett.* **103**, 266803 (2009).

58 Gomes, K. K. *et al.* Quantum imaging of topologically unpaired spin-polarized Dirac fermions. *arXiv:0909.0921v2* (2009).

59 Kim, S. *et al.* Surface Scattering via Bulk Continuum States in the 3D Topological Insulator $Bi_2Se_3$. *Phys. Rev. Lett.* **107**, 056803 (2011).

60 Hsieh, D. *et al.* A topological Dirac insulator in a quantum spin Hall phase. *Nature* **452**, 970-974 (2008).

61 Hsieh, D. *et al.* Observation of unconventional quantum spin textures in topological insulators. *Science* **323**, 919-922 (2009).

62 Cheng, P. *et al.* Landau Quantization of Topological Surface States in $Bi_2Se_3$. *Phys. Rev. Lett.* **105**, 076801 (2010).

63 Wray, L. A. *et al.* A topological insulator surface under strong Coulomb, magnetic and disorder perturbations. *Nat. Phys.* **7**, 32-37 (2011).

64 Chen, J. *et al.* Gate-Voltage Control of Chemical Potential and Weak Antilocalization in $Bi_2Se_3$. *Phys. Rev. Lett.* **105**, 176602 (2010).

65 Peng, H. L. *et al.* Aharonov-Bohm interference in topological insulator nanoribbons. *Nat Mater* **9**, 225-229 (2010).

66 Cha, J. J. *et al.* Magnetic Doping and Kondo Effect in $Bi_2Se_3$ Nanoribbons. *Nano Lett.* **10**, 1076-1081 (2010).

67 Jenkins, G. S. *et al.* Terahertz Kerr and reflectivity measurements on the topological insulator $Bi_2Se_3$. *Phys. Rev. B* **82**, 125120 (2010).

68 Hsieh, D. *et al.* Nonlinear Optical Probe of Tunable Surface Electrons on a Topological Insulator. *Phys. Rev. Lett.* **106**, 057401 (2011).

69 Hor, Y. S. *et al.* Superconductivity in $Cu_xBi_2Se_3$ and its Implications for Pairing in the Undoped Topological Insulator. *Phys. Rev. Lett.* **104**, 057001 (2010).

70 Zhang, Y. *et al.* Crossover of the three-dimensional topological insulator $Bi_2Se_3$ to the two-dimensional limit. *Nat. Phys.* **6**, 584-588 (2010).

71 Fu, L. Hexagonal Warping Effects in the Surface States of the Topological Insulator $Bi_2Te_3$. *Phys. Rev. Lett.* **103**, 266801 (2009).

72 Liu, C. X. *et al.* Model Hamiltonian for topological insulators. *Phys. Rev. B* **82**, 19 (2010).

73 Alpichshev, Z., Analytis, J. G., Chu, J. H., Fisher, I. R. & Kapitulnik, A. STM imaging of a bound state along a step on the surface of the topological insulator $Bi_2Te_3$. *Phys. Rev. B* **84**, 041104 (2011).

74 Chen, Y. L. *et al.* Single Dirac Cone Topological Surface State and Unusual Thermoelectric Property of Compounds from a New Topological Insulator Family. *Phys. Rev. Lett.* **105**, 266401 (2010).

75 Kuroda, K. *et al.* Experimental Realization of a Three-Dimensional Topological Insulator Phase in Ternary Chalcogenide $TlBiSe_2$. *Phys. Rev. Lett.* **105**, 146801 (2010).

76 Wang, Y. J., Lin, H., Das, T., Hasan, M. Z. & Bansil, A. Topological insulators in the quaternary chalcogenide compounds and ternary famatinite compounds. *New J. Phys.* **13** (2011).

77 Chen, S. *et al.* Band structure engineering of multinary chalcogenide topological insulators. *Phys. Rev. B* **83**, 245202 (2011).

78 Hsieh, D. *et al.* A tunable topological insulator in the spin helical Dirac transport regime. *Nature* **460**, 1101-1105 (2009).

79 Analytis, J. G. *et al.* Bulk Fermi surface coexistence with Dirac surface state in $Bi_2Se_3$ : A comparison of photoemission and Shubnikov-de Haas measurements. *Phys. Rev. B* **81**, 205407 (2010).

80 Beidenkopf, H. *et al.* Spatial fluctuations of helical Dirac fermions on the surface of topological insulators. *Nat. Phys.* **7**, 939-943 (2011).

81 Williams, R. S., Medeiros-Ribeiro, G., Kamins, T. I. & Ohlberg, D. A. A. Equilibrium Shape Diagram for Strained Ge Nanocrystals on Si(001). *J. Phys. Chem. B* **102**, 9605-9609 (1998).

# Chapter 2

# Experimental setup and substrate description

## 2.1 Experimental setup

In order to explore different types of surfaces and nanostructures, many surface sensitive analysis techniques, including SPM, LEED, AES and PES are normally employed. In this project, STM, AES and LEED are used to characterize the substrates, and Sb or CdSe films. Thus the description of the working principle of these techniques is presented here first. Besides, multi-component UHV chambers which are equipped with these techniques will also be introduced.

### 2.1.1 STM/STS

Generally speaking, many instruments for the exploration of surfaces, thin films and nanostructures depend on two kinds of working principles. One is based on the diffraction or interference between probing particles (such as photons and electrons) after scattering with the periodically structural arrangement in the studied material. For instance, X ray diffraction (XRD) and LEED are representatives of the first kind, which can capture the average information of the reciprocal space. The other is based on microscopy techniques, such as the high resolution optical microscopy, transmission electron microscopy (TEM) and field-ion microscopy (FIM), which are capable of detecting local properties in real space. However, the disadvantage for those techniques is that it has relative low resolutions due to the limitation of particles' wavelength or the beam size.

In 1982, the first STM was built by Gerd Binnig and Heinrich Rohrer in IBM Research Laboratory, where they successfully revealed real-space atomic-scale image of Si(111)-7×7. The new type of microscopy has a lateral resolution as high as 1 Å and a vertical resolution 0.1 Å. More importantly, it reflects information of the real space rather than that of the reciprocal space. Since then, STM has been widely used to investigate the atomic structures and physical or chemical processes on the various surfaces[1,2], and subsequently stimulated many other microscopy techniques, such as atomic force microscopy (AFM), magnetic force microscopy (MFM) and near-field scanning optical microscopy (NSOM). Therefore, in 1986 Binnig and Rohrer as well as inventors of scanning electron microscopy (SEM) were rewarded Nobel Prize in physics for their pioneer work.

As shown in Fig. 2.1, a STM can simply be treated as a metal-vacuum-metal junction, where one metallic electrode is an atomic sharp metallic tip mounted on a piezoelectric tube scanner with electrodes, voltage control circuit, feedback control circuit, signal amplifier, data processing and display terminal, while the other is the conducting sample.

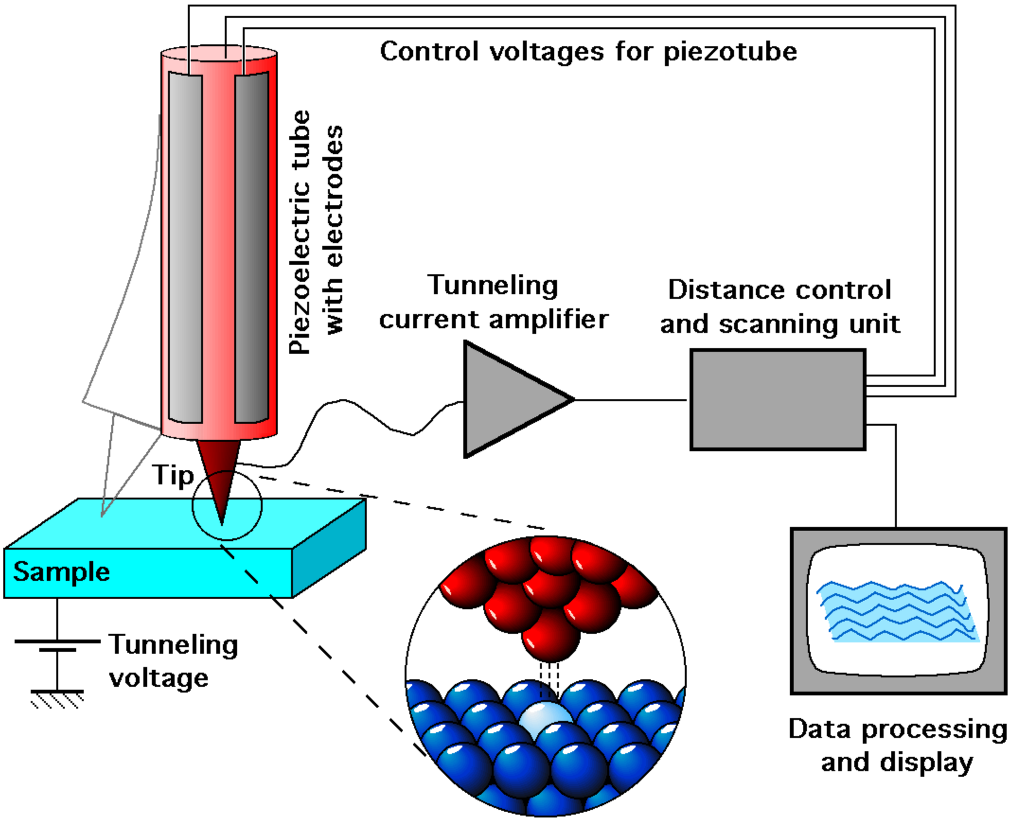

**Fig. 2.1** The schematic of a STM system. The inset shows the zoom-in junction formed by both the tip and sample [adapted from Wikimedia Commons file “File:ScanningTunnelingMicroscope schematic.png "].

#### *2.1.1.1 Theory and working principle of STM*

From classical physics we know that a particle of energy $E$ cannot pass through a region with the potential energy $U$ if $U>E$. However, from quantum mechanics we learn that the wavefunction of the particle in the classical “forbidden region” may be non-zero, which means a particle has some probability to pass through that potential barrier. This phenomenon is called tunneling.

Specifically, within the 1D tunneling junction formed by the tip and sample in STM as shown in the inset of Fig. 2.1, the motion of an electron of Energy $E$ under the potential $U(z)$ needs to satisfy Schrodinger equation:

$$-\frac{\hbar^2}{2m}\frac{d^2}{dz^2}\psi(z)+U(z)\psi(z)=E\psi(z) \tag{2.1}$$

In the region where $E<U(z)$, we have

$$\psi(z)=\psi(0)e^{-kz} \tag{2.2}$$

Here
$$k=\frac{\sqrt{2m\phi}}{\hbar} \tag{2.3}$$

is the decay constant if we define $\phi=U-E$, and $\phi$ is the work function. So Eq. (2.2) indicates that the wavefunction of the electron decays exponentially into the vacuum region from the tip or sample surface along the $z$ direction. Given that m=9.1× $10^{-31}$ kg, $\hbar=1.05\times10^{-34}\,\mathrm{J\cdot s}$ and typical metal work function of 4 eV, the k value is approximately 1 $Å^{-1}$.

If the work functions for tip and sample are the same, i.e. $\phi_{tip}=\phi_{sample}=\phi$, when no voltage is applied, although the electrons can tunnel between the two electrodes, there are no net tunneling current as shown in Fig. 2.2(a). However, if the sample is positive biased and the tip is grounded, the Fermi level of the tip will be shifted upward and electrons will tunnel from the occupied states of the tip to the unoccupied states (above Fermi level) of the sample, as shown in Fig. 2.3(b). On the other hand, if the sample is negative biased, the electrons will tunnel from the occupied states of the sample to the unoccupied states of the tip [Fig. 2.2(c)]. In general, all wavefunctions $\psi_n$ with energy $E_n$ between $E_F-eV$ and $E_F$ have certain probabilities to tunnel to the tip.

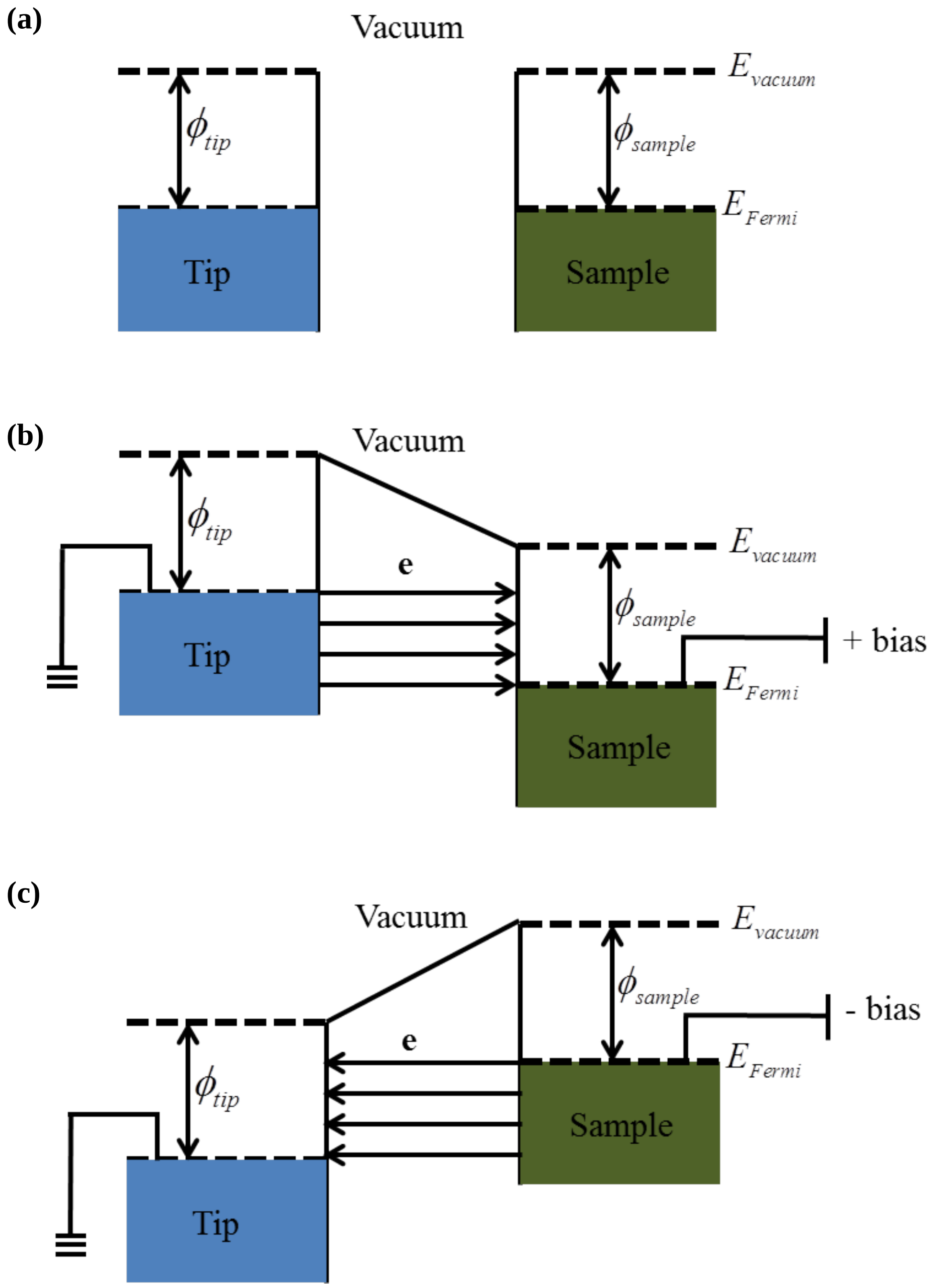

**Fig. 2.2** Energy level diagram for **(a)** independent tip and sample; **(b)** positive sample biased system; and **(c)** negative sample biased system.

Assuming that the bias is much smaller than the work function, we know almost all the states that may involve in the tunneling process should lie very close to the Fermi level, and thus we can conclude the tunneling current is proportional to the probability of electrons tunneling to the tip, which is the square of the wavefunction in Eq. (2.2). Including all the wavefunctions with energy $E_n$ between $E_F - eV$ and $E_F$, we can get

$$I \propto \sum_{E_n = E_F - eV}^{E_F} \left|\psi(0)\right|^2 e^{-2kz} \tag{2.4}$$

From Eq. (2.4), since the tunneling probability decays exponentially as the barrier width increases, the tunneling current is extremely sensitive to the sample-tip distance *z*. If the distance increases by 1 Å, which is the typical value of $k^{-1}$, the current will decrease by a factor of $e^2$, i.e. 7.4, meaning that the current comes from only a few atoms at the most forefront of the tip.

### *2.1.1.2 Basic Principles of STS*

STM is also applied for spectroscopy measurements, i.e. STS, which can reveal the local density of states (LDOS) of the sample. To obtain the local electronic structure, the tunneling current *I* is measured as a function of applied sample bias voltage *V*. Based on the first-order perturbation theory of the tunneling current in Bardeen's formalism[3] we have

$$I = \frac{2\pi e}{\hbar} \int \rho_s(E_F - eV + \varepsilon)\rho_t(E_F + \varepsilon)\left[ f(E_F - eV + \varepsilon) - f(E_F + \varepsilon)\right]\left|M\right|^2 d\varepsilon \tag{2.5}$$

where $V$ is the sample bias with respect to the tip, $f(E)$ is the Fermi-distribution function and $M$ is the tunneling matrix element between the wavefunctions of two states[4].

We neglect the contribution of reverse tunneling here. Besides, for simplicity, the tunneling tip is regarded as a point probe, the sample bias voltage is small and the temperature is low enough, so the Fermi-distribution function can be replaced by a step function, Eq. (2.5) becomes

$$I = \frac{2\pi e}{\hbar}\int_0^{eV} \rho_s(E_F - eV + \varepsilon)\rho_t(E_F + \varepsilon)\left|M\right|^2 d\varepsilon \tag{2.6}$$

To further simplify the expression, we assume the tunneling matrix remain constant in the measurement range, and get

$$I \propto \frac{2\pi e}{\hbar}\int_0^{eV} \rho_s(E_F - eV + \varepsilon)\rho_t(E_F + \varepsilon) d\varepsilon \tag{2.7}$$

Since the LDOS measurement usually corresponds to a very limited energy range, from the derivative form of Eq. (2.7) we get

$$\frac{dI}{dV} \propto \rho_s(E_F - eV) \tag{2.8}$$

where $\rho_s$ is the surface LDOS of the sample.

#### ***2.1.1.3 FT-STS method***

In condensed matter physics, nearly every important physical quantity is related in one way or another to the band structure, especially that near the Fermi surface. Hence, a lot of efforts have been made to reveal the band structure, helping us understand and manipulate the physical properties associated with it. Specifically, for surfaces and other 2D systems, ARPES has been used widely to map the energy bands as a function of momentum parallel to the cleaved surface. Besides, FT-STS is also a powerful tool, which can image the real-space scatterings on the surface to reflect the band structure. At certain energy level, scattering patterns caused by defects or impurities are actually an amplitude modulation of LDOS through a scattering vector, $\mathbf{q} = \mathbf{k}' - \mathbf{k}$, where interference of incoming and outgoing waves at momenta $\mathbf{k}$ and $\mathbf{k}'$ leads to the change of LDOS. This change can be directly observed by STM/STS. Hence, after fast Fourier transform, the real-space scatterings can be visualized as a distribution of $\mathbf{q}$ in the momentum space, offering us detailed information of the constant energy contour (CEC) at a given energy. Moreover, the dispersion relationship can also be extracted based on a series of CECs[5-8].

However, it is worth noting that ARPES can reveal the dispersion directly, i.e. E vs. $\boldsymbol{k}$, whereas since FT-STS relies on the scattering vector $\mathbf{q}$, it only offers the dispersion “indirectly”, i.e. E vs. $\boldsymbol{\Delta k}$. Nevertheless, sometimes scatterings are explicitly related to spin directions of initial and final momenta and they are well confined by the spin conservation law. In this sense, FT-STS is capable of unveiling the picture of the surface band structure as well as the associated spin texture. That’s why it has been used widely in the fields of TIs[8-14]. A detailed process of obtaining a FT-STS image on our Sb films will be introduced in Chap. 3.

### 2.1.2 LEED

We know that XRD based on Bragg's law is widely used to characterize the diffraction of the bulk in a crystal. The diffraction can be obtained at certain angles where the path difference is integer values in unit of the incident wavelength $\lambda$.

Yet the X-ray is incapable of detecting the diffraction from the surface, because it penetrates deep into the sample and thereby obtains diffraction averaged over the bulk. So the surface diffraction needs a minimal penetration length into the sample in case the bulk information may obscure the surface one. Scientists find that electrons are best candidates for this task, which have much shorter penetration depth compared to the X-ray. Next we need to calculate the wavelength appropriate for the surface diffraction. Using de Broglie relationship, $\lambda$ is given by

$$\lambda = \frac{h}{p} = \frac{h}{\sqrt{2m_e E_k}} = \frac{12.25}{\sqrt{E_k}} \text{Å} \tag{2.9}$$

where $E_k$ is the kinetic energy of electrons in unit of eV. Since the atomic spacing in solid is typically a few Å, normally the electron energy smaller than 150 eV is proper. Moreover, electrons with energy of around 100eV have the minimal escape depth, which is defined as the distance electrons can travel without losing energy. Therefore electrons in this low energy range are ideal for surface diffraction as measured in LEED.

A typical LEED instrument is shown in the schematic drawing [Fig. 2.3(a)]. Basically, there should be an electron gun, which generates a well collimated mono-energetic electron beam[15] to normally hit the sample surface; a fluorescent screen which carries a high positive bias to be visible after being collided by diffracted electrons; and energy filtering grids, which select only electrons with the same kinetic energy as the primary electrons. There are two kinds of backscattered electrons, i.e. elastically and inelastically scattered electrons. The latter are not useful and largely suppressed by grids $G_2$, $G_3$ and $G_4$, which are held at an adjustable negative bias in case inelastically scattered electrons arrive at the fluorescent screen to form a bright background and diffuse the useful information, while the former are accelerated by positive high voltage and excite the fluorescence on the screen to form bright spots. Fig. 2.3(b) shows an example of LEED pattern of Si(111)-7×7. In general, LEED provides a snapshot of the 2D reciprocal lattice of the near-surface layers.

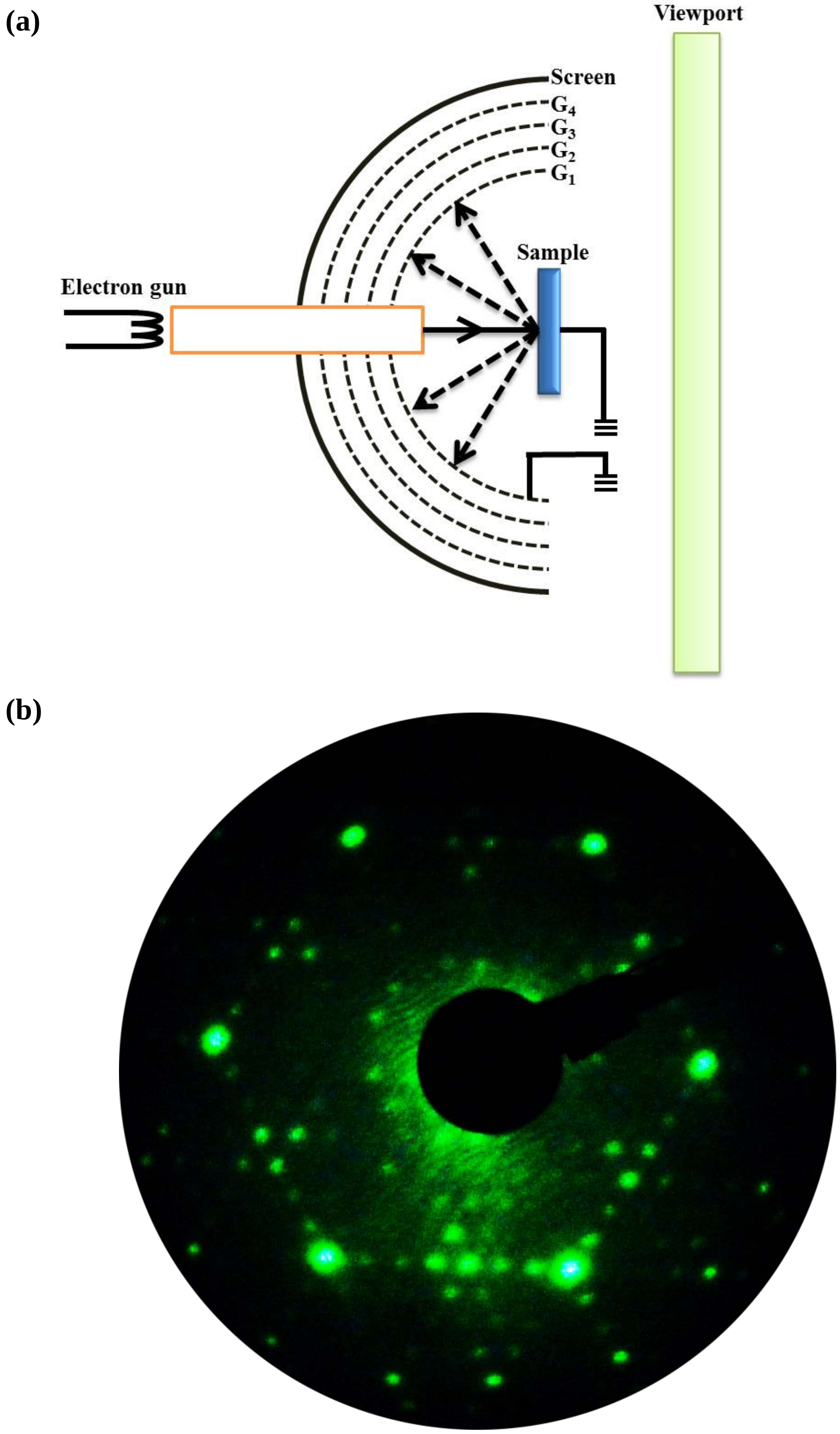

**Fig. 2.3 (a)** Schematic of the LEED, and **(b)** the image of a LEED pattern of Si(111)-7×7.

### 2.1.3 AES

In 1925, the Aüger emission was discovered by Pierre Aüger when he worked with X-rays. Based on that, AES was well developed in the late 1960's when UHV techniques were widely used. By AES we can determine the elemental composition of the surface. The principle of the generation process of Aüger electrons is illustrated in Fig. 2.4, where the electron energy levels (K, L, ...) are represented by horizontal lines, and occupied/unoccupied electronic states are represented by the solid/open circles. We can see that two steps are involved in the process. One is excitation of a K level electron and the other is de-excitation of that. After the excitation, the atom has a hole in core level and thereby is unstable. So an electron from a higher state tends to fill it, which induces the de-excitation. Normally there are two ways to realize it. One is that an electron from the $L_{III}$ level fills it by emitting a photon with the energy (E(K)- E($L_{III}$)). The other is significant for this technique, where the core level hole is filled by the transition of an electron from a higher level $L_I$. As a result, the energy difference (E(K)-E($L_I$)) is available as excess kinetic energy given to another electron either in the same level or in a more shallow level, whereupon the second electron ($L_{III}$) is ejected. And this process is called Auger emission.

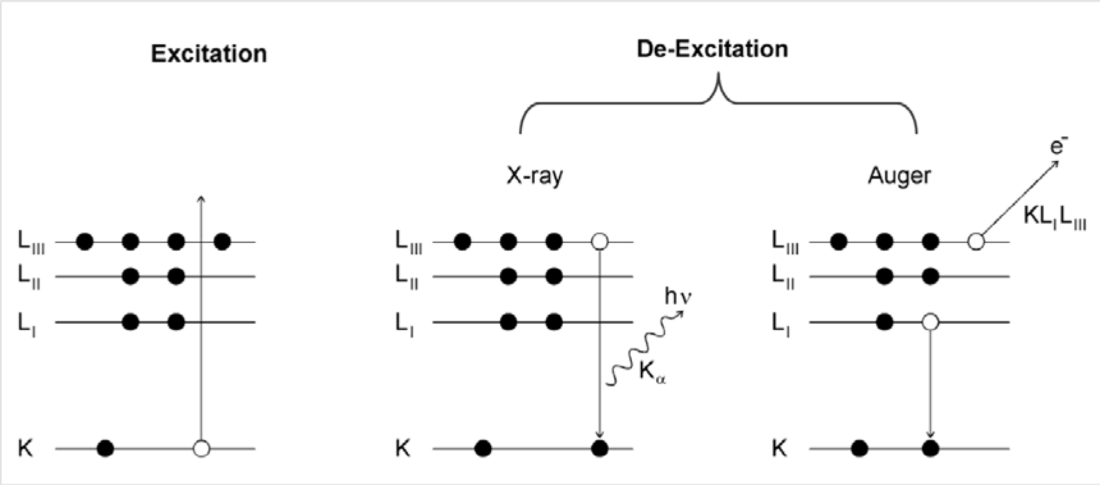

**Fig. 2.4** Schematic of the generation process of Aüger electrons.

After the emission of Aüger electrons, we need to analyze them, which is a technical problem dealing with charged particles with high sensitivity. Usually a cylindrical mirror analyzer (CMA) is used to capture them and the resultant signal is then sent to the data processing unit. However, normally the collected Aüger signal is buried in the broad secondary electron background spectrum, so a derivative mode, which highlights the peaks by modulating the electron collection energy from an AC voltage is required to enlarge the useful information.

Since the kinetic energy of Auger electrons is a function only of atomic energy levels, each element has a unique set of Auger energies as there are no two elements with identical set of binding energies. Thus AES is perfect for elemental identification. Besides, the strong inelastic scattering occurring at energies of interest (50 eV~2500 eV) guarantees that AES is extremely sensitive to surface species.

### 2.1.4 Multi-component UHV-STM Chambers

The *in-situ* experiments were performed in an Omicron multi-chamber UHV system with a RT-STM [Fig. 2.5(a)] as well as a Unisoku multi-chamber UHV system with a LT-STM [Fig. 2.5(b)]. The base pressure for both systems is $\sim 7\times10^{-11}$ mbar. To maintain the vacuum level, the mechanical pump, turbo-molecular pump (TMP), titanium sublimation pump (TSP), and ion pump are used. The pressure was measured by commercial ion gauges.

To explicitly illustrate the UHV system, we use the widely used Omicron system as an example. It consists of an analysis chamber (A chamber), preparation chamber (P chamber) and load-lock chamber (LL chamber) separated by gate valves. The load-lock chamber for loading samples and tips is equipped with a small TMP, while the other two are equipped with TSPs and ion pumps.

In terms of sample and tip transfer inside the system, two X-Y-Z-manipulators in A and P, two magnetic transfer arms between LL and P as well as between P and A, and the wobble stick in A are used.

In terms of sample preparation, two manipulators are used for degassing, cleaning and deposition purposes. The sample holders on both manipulators have two different heating methods, i.e., (1) resistive filament heating, for sample temperature up to 800 °C; (2) electron beam (e-beam) bombardment heating, for sample temperature up to 1400 °C. Tantalum-boats, which are stable with low cost, are used to evaporate most flake or granular sources, such as Bi, Sb, Mn, Ge, CdSe and CdS, while tungsten-filaments are used for wired materials, such as Au, Ag, Fe, Cu and In.

In terms of sample characterization, a RT-STM, LEED and AES are used in A chamber.

The Unisoku multi-chamber UHV system has a similar setup except that a cryostat filled with liquid nitrogen ($LN_2$) or liquid helium (LHe) is equipped outside the STM head, which can provide much lower thermal vibrations and thus a better resolution.

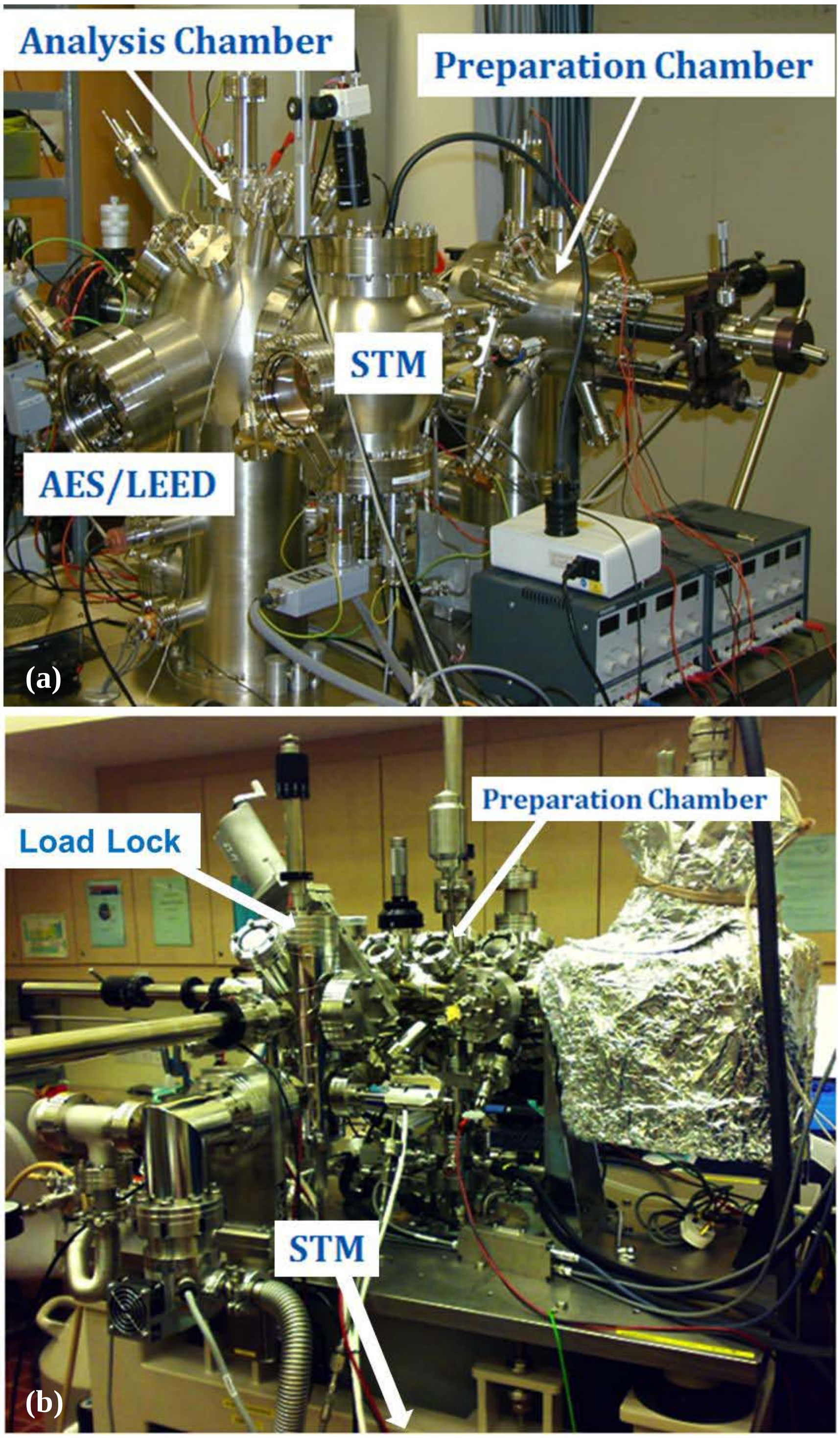

**Fig. 2.5 (a)** Photo of Omicron UHV RT-STM system. **(b)** Photo of Unisoku UHV LT-STM system.

## 2.2 Substrate description

### 2.2.1 Si(111)-7×7

Si belongs to the face-centered cubic (FCC) group with a unit-cell edge length of a=5.43 Å. Atoms in the bulk Si have four nearest neighbors with a tetrahedral bond angle of $109^{\circ}28''$, which form the $sp^3$ hybridization. Si(111) [Fig. 2.6] as one of the low index surfaces is generally used, but due to the dangling bonds on the surface it is energetically unfavorable. Si(111) with lattice constant 3.84 Å, has the surface reconstruction to minimize the number of dangling bonds and hence the surface energy. The most stable reconstruction is 7×7, which is depicted with the well-accepted dimer-adatom-stacking faults (DAS) model[16]. The first real space observation of this structure came from STM by Binnig *et al.* in 1983[17]. The DAS model of Si(111)-7×7 is shown in Fig. 2.7(a~b), where atoms in deeper layers are represented by spheres of progressively reduced sizes. The lattice constant here is 26.9 Å, i.e. 7× 3.84 Å. A typical STM image of the surface is shown in Fig. 2.7(c), in which the upper half and lower half are unoccupied-state and occupied-state images, respectively. For comparison, the unit cells are marked with yellow dashed lines.

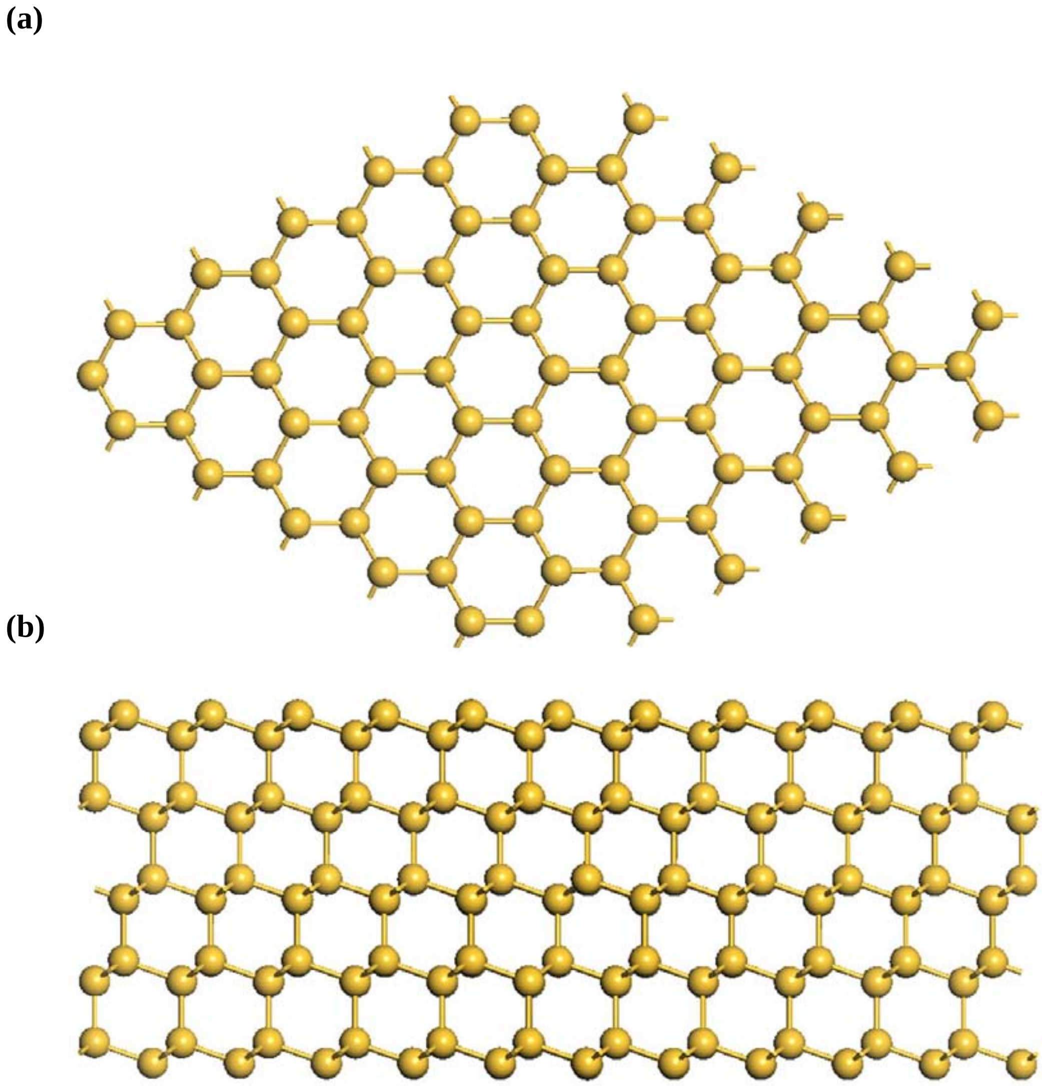

**Fig. 2.6 (a)** Top view and **(b)** side view of unreconstructed Si(111) surface. The yellow balls represent Si atoms.

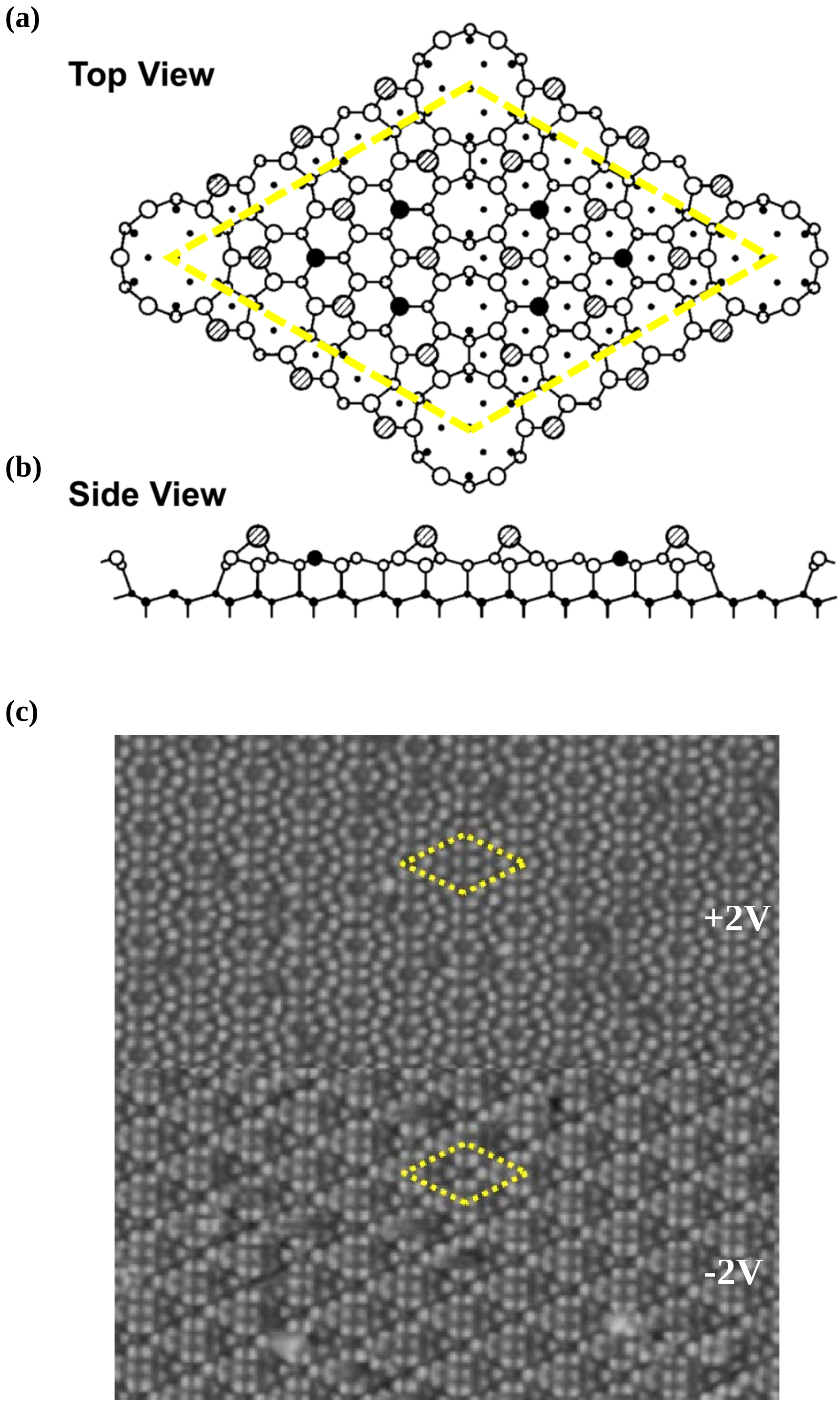

**Fig. 2.7** Comparison of the model and real structure with marked unit cells (adapted from Ref. [16], with permission from Elsevier). **(a)** Top view and **(b)** side view of Si(111) 7×7. **(c)** A 50nm×50nm STM image shows the unoccupied/occupied states taken with positive/negative bias on the tip.

### 2.2.2 Si(111)-√3×√3:Bi-β

The (√3×√3)R30° (called √3×√3 hereafter) reconstruction can be easily formed when group III, IV and V elements as well as noble metals adsorb on a Si(111) surface. Especially, group III and V atoms are of great interest since they can fully passivate the dangling bands on the surface. Particularly, Bi-induced √3×√3 reconstructed surface is one of those passivated structures that we require. It has two phases which depend on the Bi coverage. One is α-phase with coverage of 1/3 monolayer (ML) and the other is β-phase with 1 ML. In the former case single Bi atoms adsorb on the $T_4$ position of Si(111), while in the latter case Bi atoms form trimers centered on the $T_4$ position[18-22]. The schematic configurations of α and β phases are shown in Fig. 2.8(a) and (b), where the yellow balls represent Si atoms while the purple ones represent Bi atoms. The real space and reciprocal space information are shown in Fig. 2.8(c) and (d), respectively. Besides, the atomic resolution image in the inset of Fig. 2.8(c) illustrates the periodic arrangement for the reconstruction which is ultimately determined by the underlying threefold symmetry. Moreover, the Si 1×1 spots in Fig. 2.8(d) are marked by yellow circles for reference, and the sharp LEED spots reflect a good overall quality of the reconstructed surface.

Besides the passivation of this surface, another significant advantage for this reconstructed surface is that it possesses a giant spin splitting[22], because the inversion symmetry breaking in the plane due to the trimers can lead to a large in-plane potential gradient $\nabla V$ as well as large $\lambda_R$ as described in Eq. (1.5), which can enhance the spin splitting effect essentially.

To get this Si(111)-√3×√3:Bi-β surface, firstly clean Si(111)-7×7 surface is needed as the substrate, which is achieved by degassing at 500°C overnight and subsequent flashed up to 1200°C for several times. Then 2ML Bi is deposited on Si(111)-7×7 sample at room temperature, followed by annealing at about 450°C for 10 min.

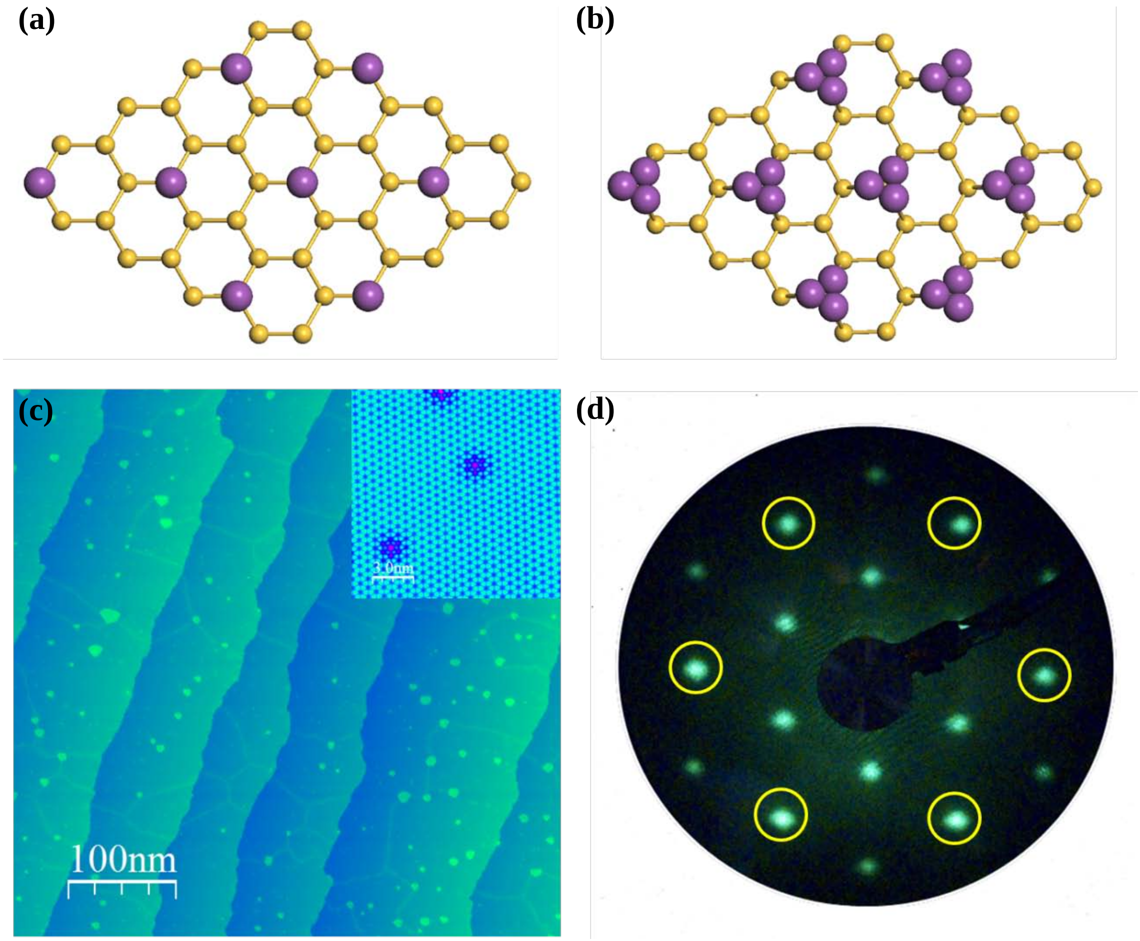

**Fig. 2.8** Structural model of two phases of Si(111)-√3×√3:Bi. **(a)** α-phase with single Bi atoms adsorbed on the $T_4$ and **(b)** β-phase with trimer Bi atoms adsorbed on the $T_4$. **(c)** Surface of Si(111)-√3×√3:Bi-β with the inset showing the atomic resolution image of 15 nm × 15 nm, and **(d)** the LEED pattern of Si(111)-√3×√3:Bi-β. The Si Si 1×1 spots are marked by yellow circles for reference.

# References

1 Neddermeyer, H. Scanning tunnelling microscopy of semiconductor surfaces. *Rep. Prog. Phys.* **59**, 701-769 (1996).

2 Besenbacher, F. Scanning tunnelling microscopy studies of metal surfaces. *Rep. Prog. Phys.* **59**, 1737-1802 (1996).

3 Bardeen, J. Tunnelling from a Many-Particle Point of View. *Phys. Rev. Lett.* **6**, 57 (1961).

4 Tersoff, J. & Hamann, D. R. Theory of the scanning tunneling microscope. *Phys. Rev. B* **31**, 805 (1985).

5 Hoffman, J. E. *et al.* Imaging quasiparticle interference in $Bi_2Sr_2CaCu_2O_{8+delta}$. *Science* **297**, 1148-1151 (2002).

6 Seo, J. *et al.* Transmission of topological surface states through surface barriers. *Nature* **466**, 343-346 (2010).

7 Okada, Y. *et al.* Direct Observation of Broken Time-Reversal Symmetry on the Surface of a Magnetically Doped Topological Insulator. *Phys. Rev. Lett.* **106**, 206805 (2011).

8 Gomes, K. K. *et al.* Quantum imaging of topologically unpaired spin-polarized Dirac fermions. *arXiv:0909.0921v2* (2009).

9 Roushan, P. *et al.* Topological surface states protected from backscattering by chiral spin texture. *Nature* **460**, 1106 (2009).

10 Kim, S. *et al.* Surface Scattering via Bulk Continuum States in the 3D Topological Insulator $Bi_2Se_3$. *Phys. Rev. Lett.* **107**, 056803 (2011).

11 Stróżecka, A., Eiguren, A. & Pascual, J. I. Quasiparticle Interference around a Magnetic Impurity on a Surface with Strong Spin-Orbit Coupling. *Phys. Rev. Lett.* **107**, 186805 (2011).

12 Zhang, T. *et al.* Experimental Demonstration of Topological Surface States Protected by Time-Reversal Symmetry. *Phys. Rev. Lett.* **103**, 266803 (2009).

13 E. van Heumen *et al.* Multiband quasiparticle interference in the topological insulator $Cu_xBi_2Te_3$. *arXiv:1110.4406* (2011).

14 Beidenkopf, H. *et al.* Spatial fluctuations of helical Dirac fermions on the surface of topological insulators. *Nat. Phys.* **7**, 939-943 (2011).

15 Chutjian, A. Geometries and focal properties of two electron-lens systems useful in low-energy electron or ion scattering. *Rev. Sci. Instrum.* **50**, 347-355 (1979).

16 Takayanagi, K., Tanishiro, Y., Takahashi, S. & Takahashi, M. Structure analysis of Si(111)-7 × 7 reconstructed surface by transmission electron diffraction. *Surf. Sci.* **164**, 367-392 (1985).

17 Binnig, G., Rohrer, H., Gerber, C. & Weibel, E. 7 × 7 Reconstruction on Si(111) Resolved in Real Space. *Phys. Rev. Lett.* **50**, 120-123 (1983).

18 Wan, K. J., Guo, T., Ford, W. K. & Hermanson, J. C. Initial growth of Bi films on a Si(111) substrate- 2 phases of $\sqrt{3}\times\sqrt{3}$ low-energy-electron-diffraction pattern and their geometric structures. *Phys. Rev. B* **44**, 3471-3474 (1991).

19 Park, C., Bakhtizin, R. Z., Hashizume, T. & Sakurai, T. Scanning tunneling microscopy of $\sqrt{3}\times\sqrt{3}$-Bi reconstructon on the Si(111) surfaces. *Jpn. J. Appl. Phys. Part 2 - Lett.* **32**, L290-L293 (1993).

20 Shioda, R., Kawazu, A., Baski, A. A., Quate, C. F. & Nogami, J. Bi on Si(111): Two phases of the $\sqrt{3}\times\sqrt{3}$ surface reconstruction. *Phys. Rev. B* **48**, 4895 (1993).

21 Kuzumaki, T. *et al.* Re-investigation of the Bi-induced Si(111)-($\sqrt{3}\times\sqrt{3}$) surfaces by low-energy electron diffraction. *Surf. Sci.* **604**, 1044-1048 (2010).

22 Gierz, I. *et al.* Silicon Surface with Giant Spin Splitting. *Phys. Rev. Lett.* **103**, 046803-046804 (2009).

# Chapter 3

# STM/STS investigations of Sb (111) thick films

## 3.1 Introduction

### 3.1.1 Lattice Structure of Sb(111)

Antimony (Sb) is a prototypical group-V semimetal with the rhombohedral A7 structure in normal conditions, which can be derived by a slight distortion of a cubic lattice, as shown in Fig. 3.1(a). The angle between the rhombus base vectors [**a**, **b** and **c** in Fig. 3.1(a)] is 57.1 °, only 2.9 ° smaller than 60 °, and the latter corresponds to the fcc lattice. Although scientists may choose pseudo-cubic or 4-digit hexagonal index to describe the Sb lattices[1,2], here we use 3-digit rhombohedral index to denote them which is more commonly used.

Since each Sb atom forms covalent bonds with three nearest neighbors within the bilayer with the bond angle 95.6 ° which is slightly larger than 90 °, when we particularly look at Sb(111) surface formed by ABC stacking of covalent-bonded (111) bilayers [Fig. 3.1(b)], we can find that each bilayer forms a “stretched graphene”-like construction, implying a similar structure as graphene except the two sets of sublattices are not within the same plane. The atomic resolution image shown in Fig. 3.1(d) illustrates the hexagonal arrangement of Sb atoms on the (111) surface without any reconstruction.

Besides, as shown in Fig.3.1 (c), there are dangling bonds on bulk-terminated Sb(110) surface with a rectangular surface unit cell.

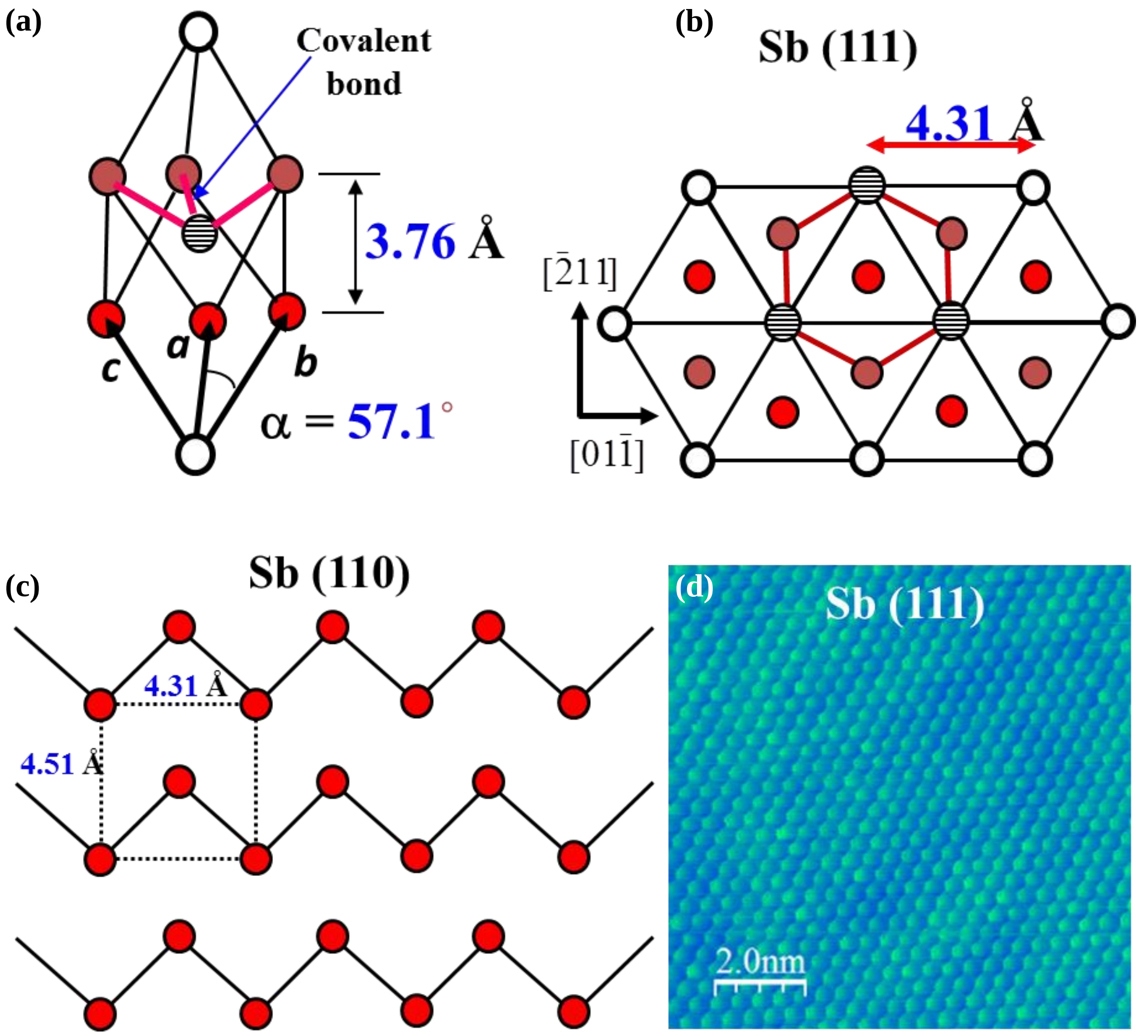

**Fig. 3.1 (a)** Schematic of the rhombohedral lattice for bulk Sb crystals in a unit cell with base vectors marked as **a**, **b** and **c. (b)** Top view of Sb(111) and **(c)** Sb(110) plane. **(d)** a 10nm×10nm atomic resolution image of Sb(111).

### 3.1.2 Growth mechanics of Sb

The growth mechanism of Sb has been extensively studied, especially on the inert substrate highly oriented pyrolytic graphite (HOPG)[3-6]. Since in the PVD process Sb comes out mostly as $Sb_4$ molecules, the size of $Sb_n$ largely determines the islands shape from compact spheres to ramified fractals, which can be explained in terms of the interplay of $Sb_n$ arriving rate at an existing island and the time it takes for the cluster and island to coalesce. Additionally, considering the diffusion and nucleation of chemisorbed $Sb_4$ besides physisorbed $Sb_4$, 1D nanorods, 2D crystalline islands and 3D islands can also be formed[6], as shown in Fig. 3.2(a). In the same sense, Sb also has different phases when deposited on Si(111)-$\sqrt{3}\times\sqrt{3}$:Bi-β. For example, in Fig. 3.2(b) Sb(110) nanorods and Sb(111) islands coexist on the substrate, and the nanorods tend to grow in parallel and form bundles, which are as thick as 5nm [Fig. 3.2(c)]. A possible scenario for formation of the bundles is that since Sb clusters remain quite mobile on the substrate, the trapping of nuclei of new rods by the existing ones can be significant in this situation. Therefore, the compact nuclei can find nearby existing rods and migrate along their edges.

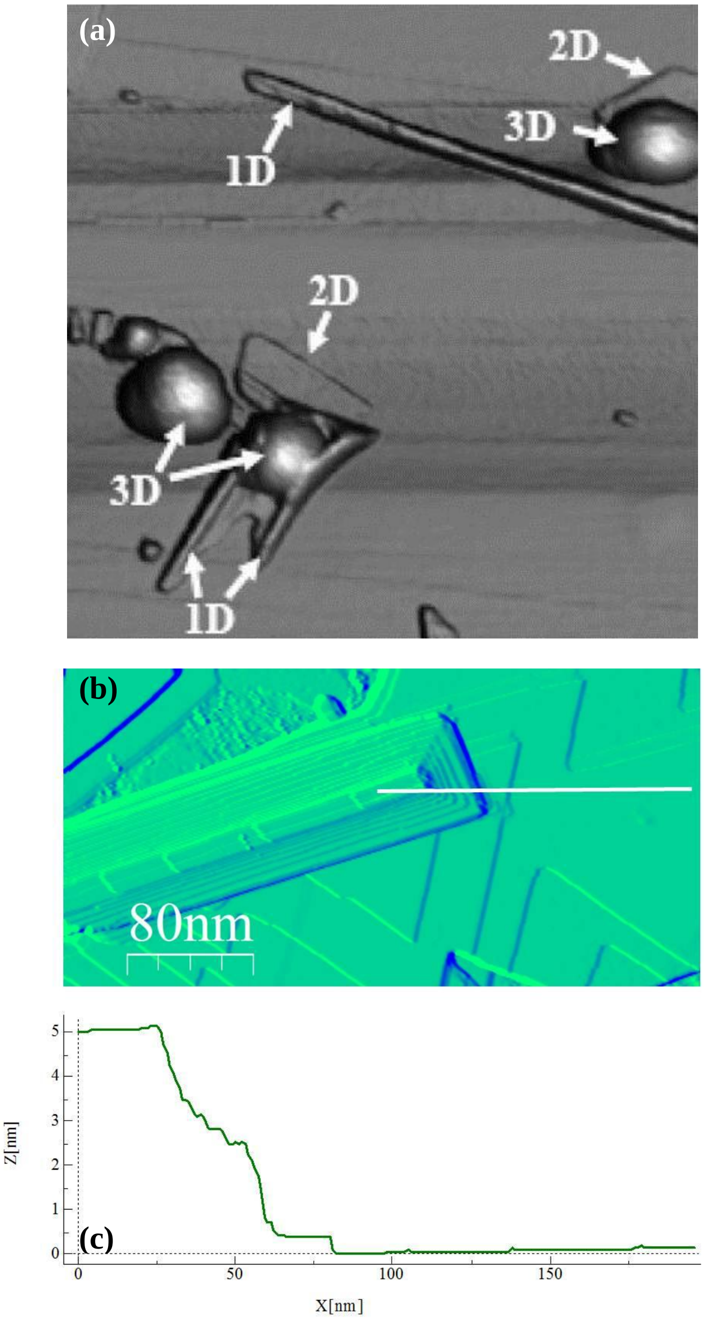

**Fig. 3.2 (a)** STM image of Sb deposited on HOPG at RT with three different types of Sb nanostructures labeled as 1D, 2D and 3D (reprinted from Ref. [6] with permission by American Institute of Physics). **(b)** a 400 nm × 200 nm STM image of coexistence of Sb(110) nanorods and Sb(111) islands. **(c)** The line profile corresponding to the white dotted line in (b) shows the Sb(110) bundles can be as high as 5nm.

### 3.1.3 Band Structure of Sb(111)

Although Sb is semimetal in bulk due to its negative indirect bandgap, it has a vital band inversion[7-10]. Due to this band inversion, recently Sb has attracted much attention and was confirmed to possess topological surface states (TSSs)[8-11] which have potential functionalities for TI-based devices aiming at the realization of spintronics and quantum computation. Unlike a well-known Dirac system such as graphene with sub-lattice pseudospin texture, TSSs in Sb and other TIs exhibit real helical spin textures confirmed by surface-sensitive experiments such as ARPES and STM, which has been well summarized in the review article[12]. Moreover, Since TSSs can be regarded as metallic states, possessing Dirac dispersion in a spin-polarized manner due to a strong spin-orbit coupling effect, the scattering between TSSs or even between TSS and bulk states (BSs) can result in QPI, which is accessible by the aforementioned techniques.

Specifically, for the potential device applications, Sb as the “parent”[9] of the first generation[13] 3D TIs $Bi_{1-x}Sb_x$, has its own advantages because on one hand, it is a simple elemental material compared with compound TIs such as $Bi_2Se_3$, $Bi_2Te_3$ and $Sb_2Te_3$, yet it has a single Dirac cone, which makes its SSs topologically nontrivial. Therefore, Sb is a good candidate for developing TI-based practical applications in a more straightforward way. On the other hand, from the ARPES measurement of Sb(111) [Fig. 3.3(a-b)], we can easily find that it has a highly warped Dirac cone, opening up new scattering channels, which is impossible for a “standard” linear Dirac cone as in $Bi_2Se_3$, because in that case due to the spin conservation law there are no available states for electrons from one band to scatter into. In this sense, it is ideal to perform FT-STS on Sb for investigating the scatterings. In this project, for comparison, first-principles electronic structure calculations based on density functional theory (DFT) using the VASP package[14] carried out by Dr. Pan Feng and Mr. Luo Ziyu in our group are also introduced, which were performed with a plane wave basis and a $5 \times 5$ ***k***-point sampling of the Brillouin zone. In all calculations, generalized gradient approximation (GGA) in Perdew-Burke-Ernzerhof (PBE) format[15] was included. The vacuum region of 10 Å along the [111] direction was employed.

Fig. 3.3(c) shows the calculated band structure of 15BL Sb(111), and Fig. 3.3(d) gives the zoom-in structure around $\bar{\Gamma}$ near the Fermi energy $E_F$. Spin directions of the bands are marked as red and blue arrows. Scatterings marked as green arrows are possible to be observed in FT-STS because they take place between SSs of the same spin direction.

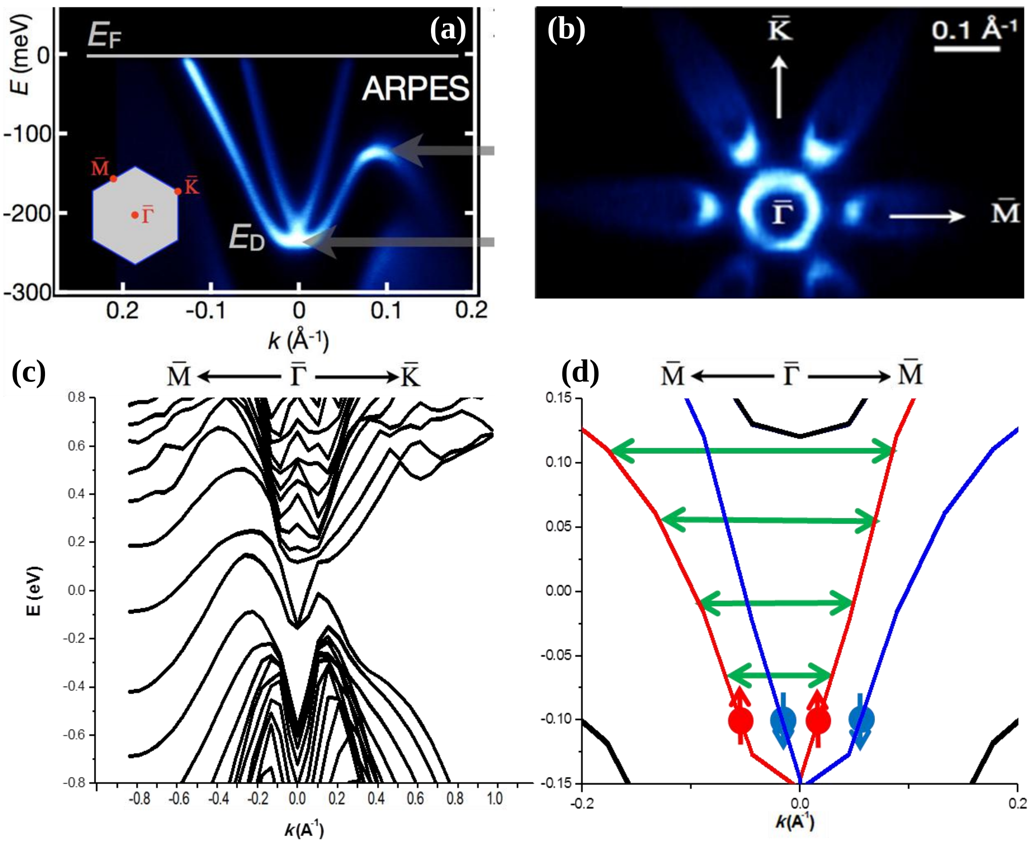

**Fig. 3.3 (a)** ARPES shows the band structure along $\overline{\mathrm{M}}-\overline{\Gamma}-\overline{\mathrm{K}}$. $E_D$ is the energy level corresponding to the Dirac point. The lower part of the Dirac cone is distorted upward resulting into a highly warped Dirac cone. Brighter parts marked with the grey arrow means lager LDOS at turning points of bands in the *k* space. **(b)** Fermi energy contour shows the Fermi surface is composed of a central electron pocket around the $\overline{\Gamma}$ point, surrounded by 6 hole pockets along $\overline{\Gamma}-\overline{\mathrm{M}}$. (Both images are reprinted from Ref. [10]). **(c)** The calculated band structure of 15BL Sb(111) along $\overline{\mathrm{M}}-\overline{\Gamma}-\overline{\mathrm{K}}$. **(d)** Zoom-in structure of the bands in (c) around $\overline{\Gamma}$ near $E_F$. Spin directions of the bands are marked as red and blue arrows while possible scatterings are marked as green arrows.

### 3.1.4 Process of FT-STS on Sb(111) surface

Besides ARPES mentioned above, FT-STS can also reveal the surface band structure as well as the associated spin texture as described in Chap. 2. Specifically, on the surface of 3D TIs, since the spin conservation plays an important role, FT-STS measurements are the ideal method, because QPI patterns induced by defects or impurities result in an amplitude modulation of LDOS, which can be directly observed by STM/STS through a scattering vector $\mathbf{q} = \mathbf{k}' - \mathbf{k}$, where the spin information of the involved momenta is the dominant factor in the scattering process. To gain FT-STS mapping of Sb(111), firstly we need to maintain a stable and reliable tip-sample condition by employing an area with large terraces, as shown in Fig. 3.4(a). As evidence of the good tip condition, the characteristic STS spectrum on that is also needed [Fig. 3.4(b)], which agrees well with the data previously reported[10,11]. Secondly the directions in momentum space needs to be determined, normally by atomic resolution images or even the directions of steps. Here in Fig. 3.4(c-d) the atomic resolution image of selected area and FFT of that image are shown. Then using directions provide by the FFT of real space images, we can tell the characteristic *k* directions such as $\overline{\Gamma}-\overline{\mathrm{M}}$ and $\overline{\Gamma}-\overline{\mathrm{K}}$ (shown in the lower right corner in Fig. 3.4(d)). Thirdly, the *dI/dV* mapping using a lock-in technique is obtained simultaneously with the recording of STM images. For example, in the mapping at +5 mV as shown in Fig. 3.4(e), due to impurities or defects on the surface, the interference patterns can be generated and explained as the modulation of LDOS at +5 meV around scattering centers. Then again, the FFT of that mapping [Fig. 3.4(f)] allows us to relate the LDOS in real space with a scattering vector **q** in the momentum space. Additionally, combined with the directions recognized in Fig. 3.4(d), we can actually determine the direction-dependent scattering events in momentum space. For instance, from Fig. 3.4(f) we know that the dominant scattering events occur along $\overline{\Gamma}-\overline{\mathrm{M}}$ because of the stronger intensity represented by the brighter color.

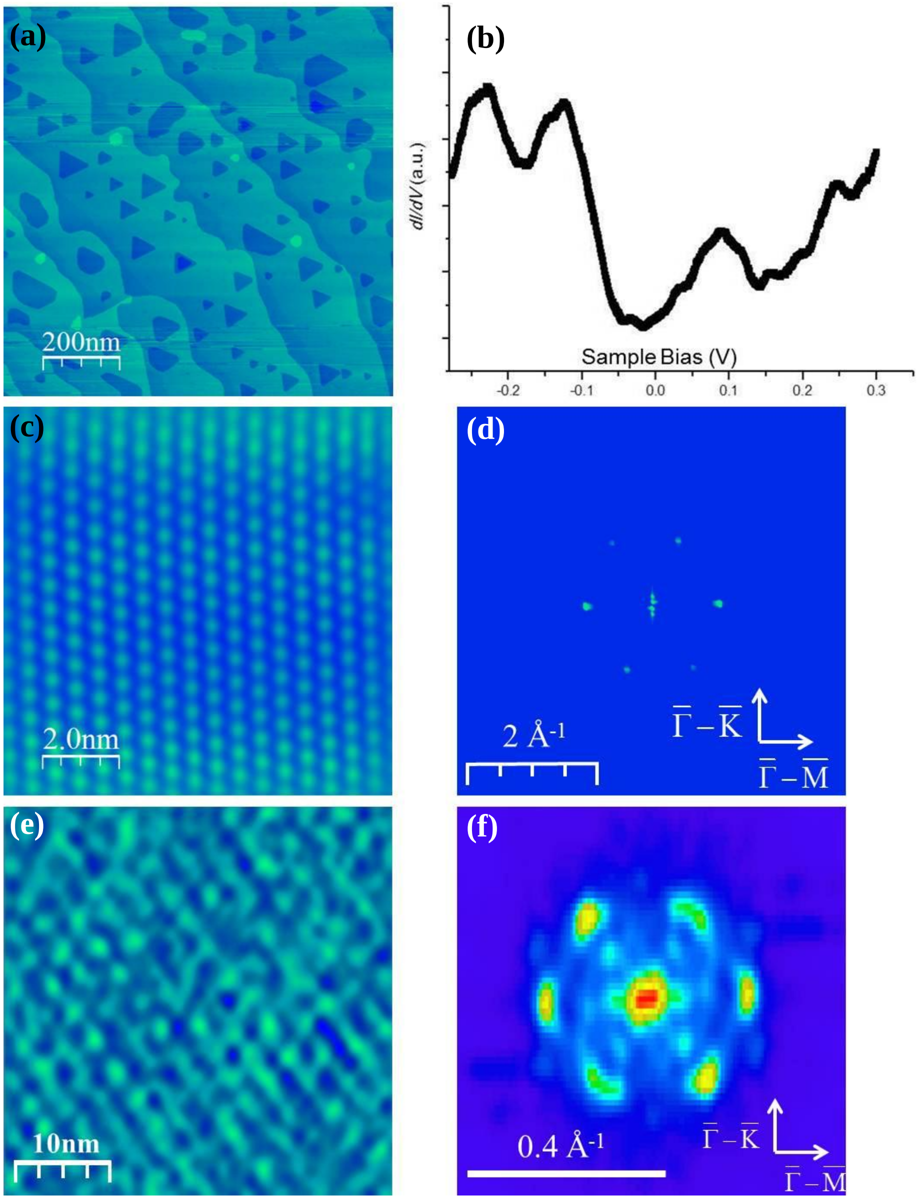

**Fig. 3.4** The process of obtaining a FT-STS image. **(a)** STM topographic image of 1 μm × 1 μm shows terraces separated with 3.7Å, which is the single atomic step. **(b)** The STS spectrum on the terrace shows the LDOS. **(c)** The 10 nm × 10 nm atomic resolution image of Sb(111) and **(d)** the corresponding FFT image. They provide the coordinate in *k* space. **(e)** The *dI/dV* mapping (40 nm × 40 nm) taken at +5 meV and **(f)** the corresponding FT-STS image. The former and latter show the scattering patterns in real and *k* space, respectively.

### 3.1.5 Outline

In this chapter, the results of our *in-situ* STM/STS investigation of the Sb(111) thick films (referred to 30BL in thickness) in UHV systems under different growth conditions are given below. Firstly, in order to yield well-ordered films of large scale which can generate more precise FT-STS signal, Sb is deposited on Si(111)-√3×√3:Bi. Then via two kinds of defects, i.e. step edges and atomic defects at terraces, 1D and 2D scattering patterns can be observed, respectively. The detailed analysis of the results unambiguously shows that the SSs of Sb(111) are indeed TSSs which possess great backscattering suppression ultimately determined by the surface band structure and the associated spin texture. Finally, the magnetic response of TSSs on Sb(111) is investigated by depositing magnetic molecules, manganese phthalocyanine (MnPc), on the films for introducing magnetic defects which may break TR symmetry. It is found that there is no difference in QPI patterns with or without MnPc molecules, which can be interpreted by the inability of detecting magnetic-impurity-induced backscattering by normal STM which lacks spin resolution, as discussed in recent papers[16,17].

## 3.2 Experimental Method

The experiments were carried out in a Unisoku UHV system equipped with a LT-STM which can perform measurements at $LN_2$ or LHe temperature. The base pressure is $7\times10^{-11}$ Torr. Si(111)-√3×√3:Bi-β serves as the growth substrate, and the method to obtain this surface was illustrated in Chap.2. The quality of Si(111)-√3×√3:Bi-β surface can be determined by both STM and LEED. High purity (99.999%) Bi and Sb were deposited at RT and $LN_2$ temperature. MnPc was deposited onto Sb(111) at $LN_2$ temperature. Prior to the deposition, MnPc was purified twice by gradient vacuum sublimation. Then all sources were degassed at appropriate temperatures for a few hours in order to remove contamination. The flux was calibrated using STM. STM images were carefully calibrated and the scanner drift was corrected. The dI/dV spectrum was acquired using a lock-in amplifier with the bias voltage modulated at a frequency of 700 Hz and a peak-to-peak amplitude of 5 mV.

## 3.3 Results and Discussion

### 3.3.1 1D scattering at step edges of Sb (111) films

From the growth mechanism discussed above, we know the composition of $Sb_n$, mainly $Sb_4$ molecules from the source, tends to form 3D clusters and other thick structures, which are often uneven, irregular and generally undesirable. Since this project focuses on 2D structures as a means of studying the TSSs properties, an alternative method needs to be found, which will be introduced in Chap. 4. Yet, the area covered mainly by Sb(111) extended islands can be selected for further investigations.

Fig. 3.5(a) shows a 250 nm × 200 nm STM image of Sb(111) islands formed on Si(111)-√3×√3:Bi-β surface maintained at 100 ℃. The islands form a screw dislocation and all steps run in three equivalent directions, which are ultimately determined by the underlying symmetry of the substrate as well as Sb(111). Under large deposition amount the height of the islands increases significantly and can be as large as 11.0 nm which correspond to 30BL of Sb (111). Since the steps perform as scattering centers when the QPI patterns are measured, a crucial problem should be raised: Do the atoms at steps have any type of reconstruction, which may influence the LDOS distributions and therefore modify the patterns and make the signature of QPI undeterminable? So the atomic resolution image along a step is shown in Fig. 3.5(b). To enhance the atomic signal over the step height difference in *z* direction, the derivative image is given in Fig. 3.5(c), from which we can confirm there is no reconstruction near the edge. Thus any observable standing waves can be regarded as the modulation of LDOS solely due to the step defects, just as the Friedel oscillation[18] along steps in a 2DEG system realized on metal surfaces at low temperature[19-23]. Besides, the step is confirmed running along $[01\bar{1}]$, which is the close-packed atom rows corresponding to $\bar{\Gamma}-\bar{K}$ in the momentum space. Therefore, it can be predicted that the standing waves due to the atomic step should propagate along $[\bar{2}11]$, and that direction corresponds to $\bar{\Gamma}-\bar{M}$.

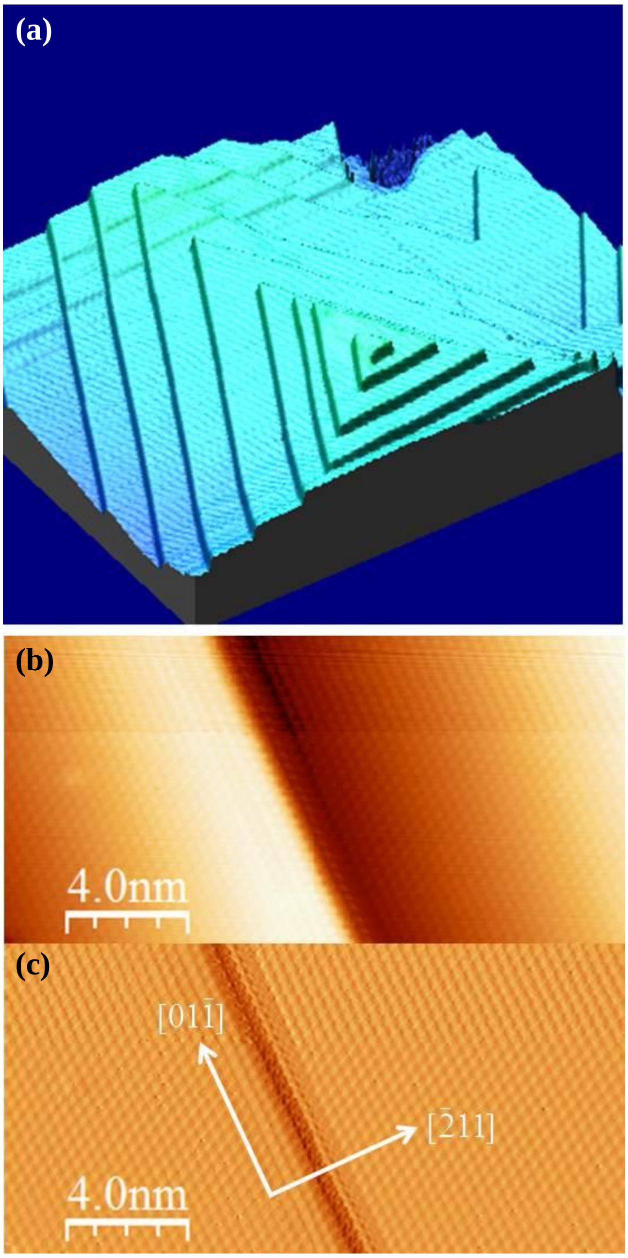

**Fig. 3.5** Sb(111) on Si(111)-$\sqrt{3}\times\sqrt{3}$:Bi-β: **(a)** a 250 nm × 200 nm image shows an island with a screw dislocation. **(b-c)** a 20 nm × 10 nm atomic resolution image along a step. (b) A constant current image. (c) The corresponding derivative image shows 1 × 1 of Sb (111) lattice without any reconstruction. The directions are marked as the white arrows.

Indeed, from Fig. 3.6, where Fig. 3.6(a) illustrates the topography of several Sb steps (80nm × 10nm) while Fig. 3.6(b) shows the simultaneously taken dI/dV mapping at a sample bias of 380 mV, we can see the standing waves are generated between steps, with $\boldsymbol{q}$ in the $[\bar{2}11]$ direction. The straight and zigzag steps coexist in this area. Interestingly, the lower steps on the right side form kinked edges, along which the standing waves exactly follow. This phenomenon confirms the fundamental role the steps play in the formation of standing waves.

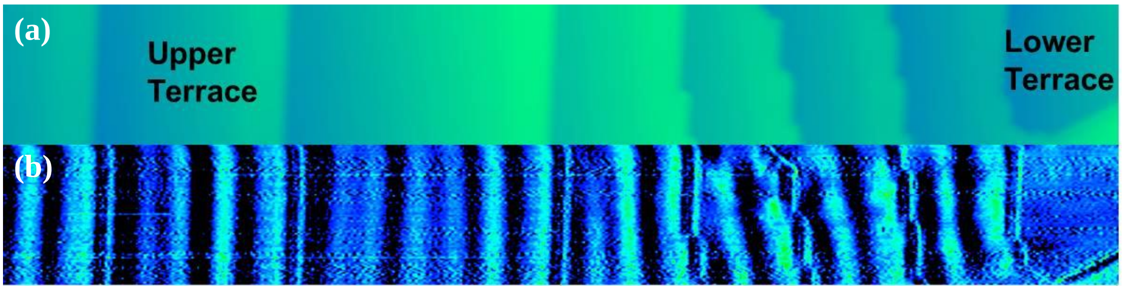

**Fig. 3.6 (a)** STM topography of multiple steps on Sb (30BL). **(b)** Representative *dI/dV* mapping at 380 mV shows the standing waves propagate exactly along the step edges.

Next, we display a series of bias-dependent *dI/dV* mapping in Fig. 3.7(b-s) in the same area where multiple steps exist, as the topography (100 nm × 10 nm) shown in Fig. 3.7(a). Then the dispersion relationship can be analyzed. It is obvious that on each terrace marked as (1-6), the wavelength λ of all standing waves changes with the energy level, especially on terrace (6), since the size is wide enough for the propagation of standing waves. Another interesting aspect is that the strength of waves decays when they are further away from the Fermi energy. Above 250mV and below -140mV the standing waves become very weak. Besides, the strength of waves also decays when they are further away from step edges.

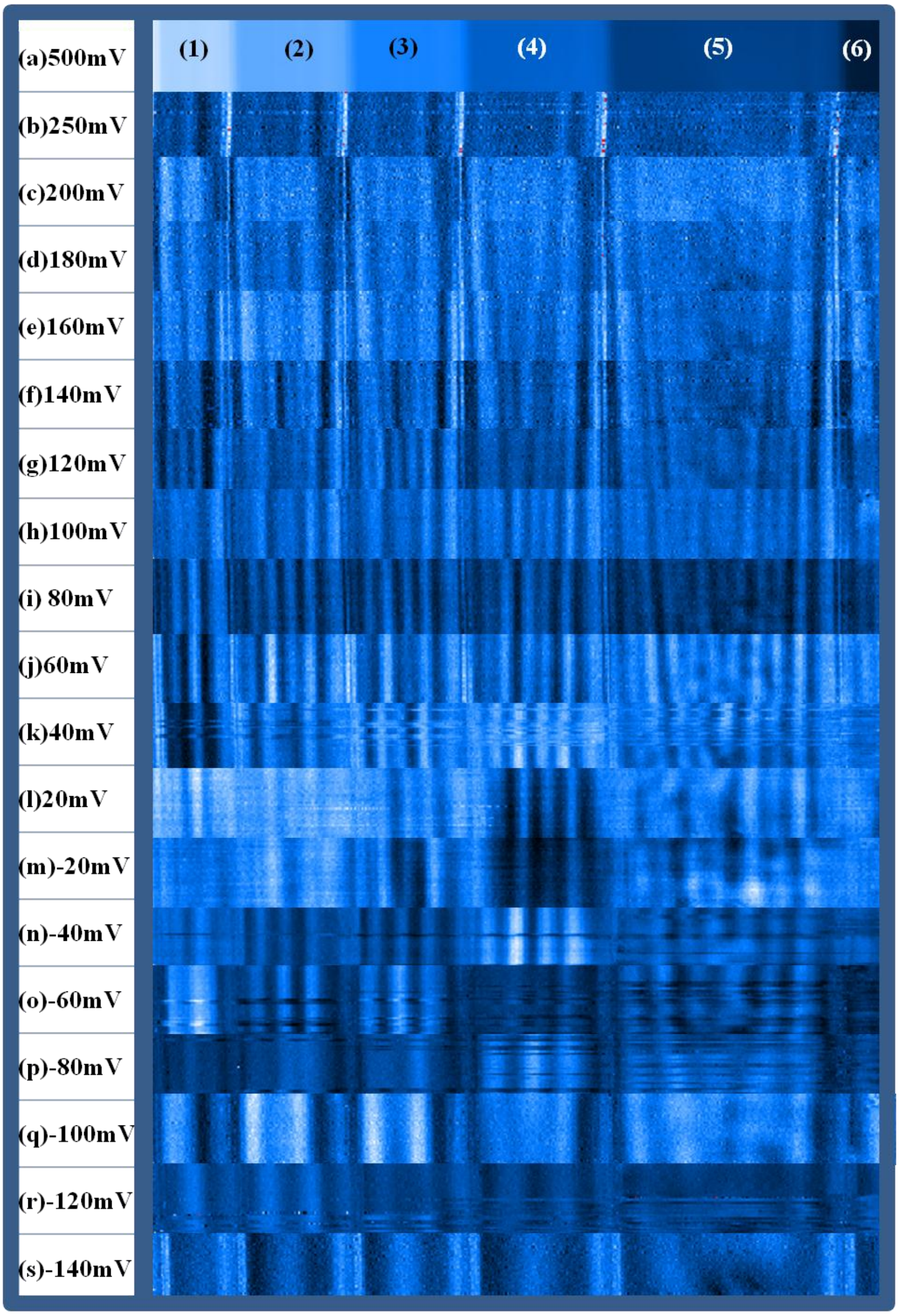

**Fig. 3.7** Standing waves due to step edges. **(a)** the STM topography (100 nm × 10 nm) of a region with multiple steps on 30BL Sb(111) surface. **(b-s)** *dI/dV* mapping shows standing waves. All of the images were taken at various bias voltages of the same area in Fig. 3.7(a).

Then the wavelength λ and the corresponding scattering vector ***q*** can be extracted from the mapping, which are averaged over scatterings at all terraces for each energy, and then listed in Table 3.1. These ***q*** values actually correspond to the scatterings occurring within the same spin direction channel marked as the green arrows in Fig. 3.3(d). Since the peaks become weaker when far away from the Fermi energy, only the mapping images taken in the energy range between -80mV and 140mV are selected. Then the linear fitting line of E vs. ***q*** is plotted in Fig. 3.8, with a slope of 1.18 eVÅ, which is in excellent agreement with the data previously reported (1.2 eVÅ)[8,11]. However, further investigations are still required, because till now it is still unknown whether these surface bands have topological properties.

**Table 3.1** The energy vs. scattering vectors ***q*** obtained by the wavelength according to ***q=2π/λ***.

| **E (eV)** | 0.14 | 0.12 | 0.10 | 0.08 | 0.06 | 0.04 | 0.02 | -0.02 | -0.04 | -0.06 | -0.08 |
|---|---|---|---|---|---|---|---|---|---|---|---|
| **λ (nm)** | 2.00 | 2.26 | 2.51 | 2.76 | 2.96 | 3.26 | 3.51 | 4.01 | 4.26 | 4.82 | 5.33 |
| ***q* ($Å^{-1}$)** | 0.31 | 0.28 | 0.25 | 0.23 | 0.21 | 0.19 | 0.18 | 0.16 | 0.15 | 0.13 | 0.12 |

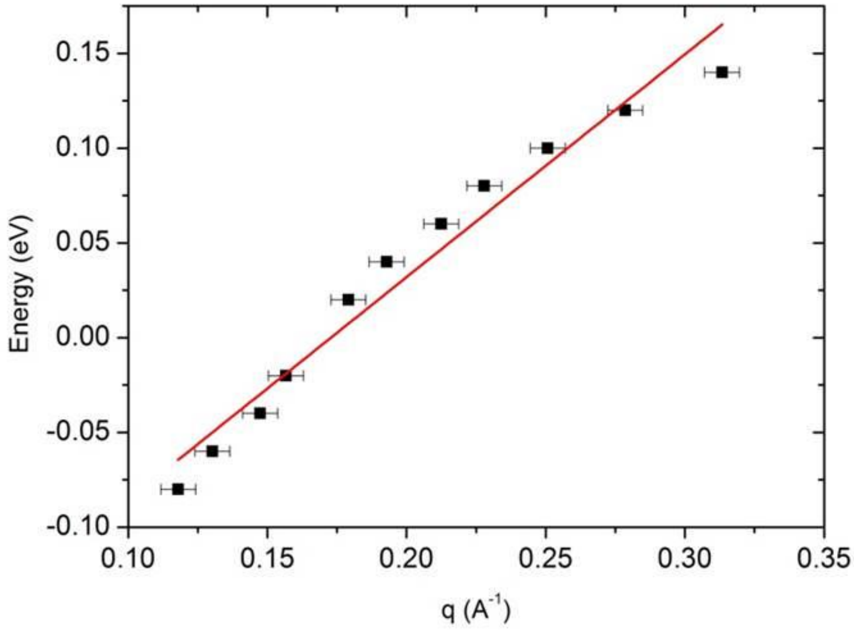

**Fig. 3.8** Energy dispersion as a function of scattering vectors ***q*** derived from Table 3.1. Here the error bar corresponds to 0.002π Å$^{-1}$, which is determined by (2π/100) nm$^{-1}$.

Omitting higher orders in momentum *k*, we get the dispersion relationship from

$$E = \hbar v_F k \tag{3.1}$$

Thus the Fermi velocity on the surface of Sb(111) is $1.79\times10^5$ m/s, which is much lower than that of bulk carriers. Therefore, it leads to a considerably higher DOS at the Fermi level. In this sense, we can conclude that the SSs of Sb(111) support more metallic SSs. Besides, according to Fig. 3.8, the wavelength $\lambda_0$ (or scattering vector $\boldsymbol{q_0}$ ) around the Fermi energy is 36.8Å (or 0.17 Å$^{-1}$), which is much smaller than that of typical Friedel oscillations at Fermi energy on the surface of metals[20], where $\boldsymbol{q}= 2\boldsymbol{k_F}$ for the SS band ( and here $k_F$ denotes Fermi wavevectors).

Although the *dI/dV* mapping mentioned above can visualize the standing waves in real space, it requires repeated scanning under different biases to reveal energy-dependent quantization. Actually, since the modulation of LDOS has the translational symmetry along the running direction of the steps if parallel and straight ones are selected, the resultant standing waves should depend solely on the direction perpendicular to the steps. Therefore another method[11,24] can be used, which records a series of STS spectra along a line in the direction perpendicular to steps simultaneously with the scanning of STM images, and thus obtains the spatial-and energy-resolved *dI/dV* spectrum. This method is more straightforward compared with *dI/dV* mapping because it can integrate the information in both real space and energy in the same figure. In the following the result of inter-step scattering on a 30BL Sb(111) is given. In Fig. 3.9(a) the chosen line is marked as the white dashed one in the topography image. The corresponding *dI/dV* spectrum is shown in Fig. 3.9(b), where the horizontal axis is the distance starting from the right step edge, the vertical one is the energy and the brightness is the intensity of LDOS, i.e. the darker the color, the lower LDOS. The striking aspect of this figure is the coexistence of interference in space and quantization in energy. The “ground state” is located at around -200 meV, above which the quantized resonances and standing waves begin to appear. The Fourier transform [Fig. 3.9(c)] of the *dI/dV* spectrum [Fig. 3.9(b)] reveals two different scattering vectors, $q_A$ and $q_B$, both with a slope of 1.20 eVÅ and a corresponding Fermi velocity of $1.82\times10^5$ m/s, which are comparable with the data gained using *dI/dV* mapping. The detailed analysis of the origin of these two vectors will be covered in the next part.

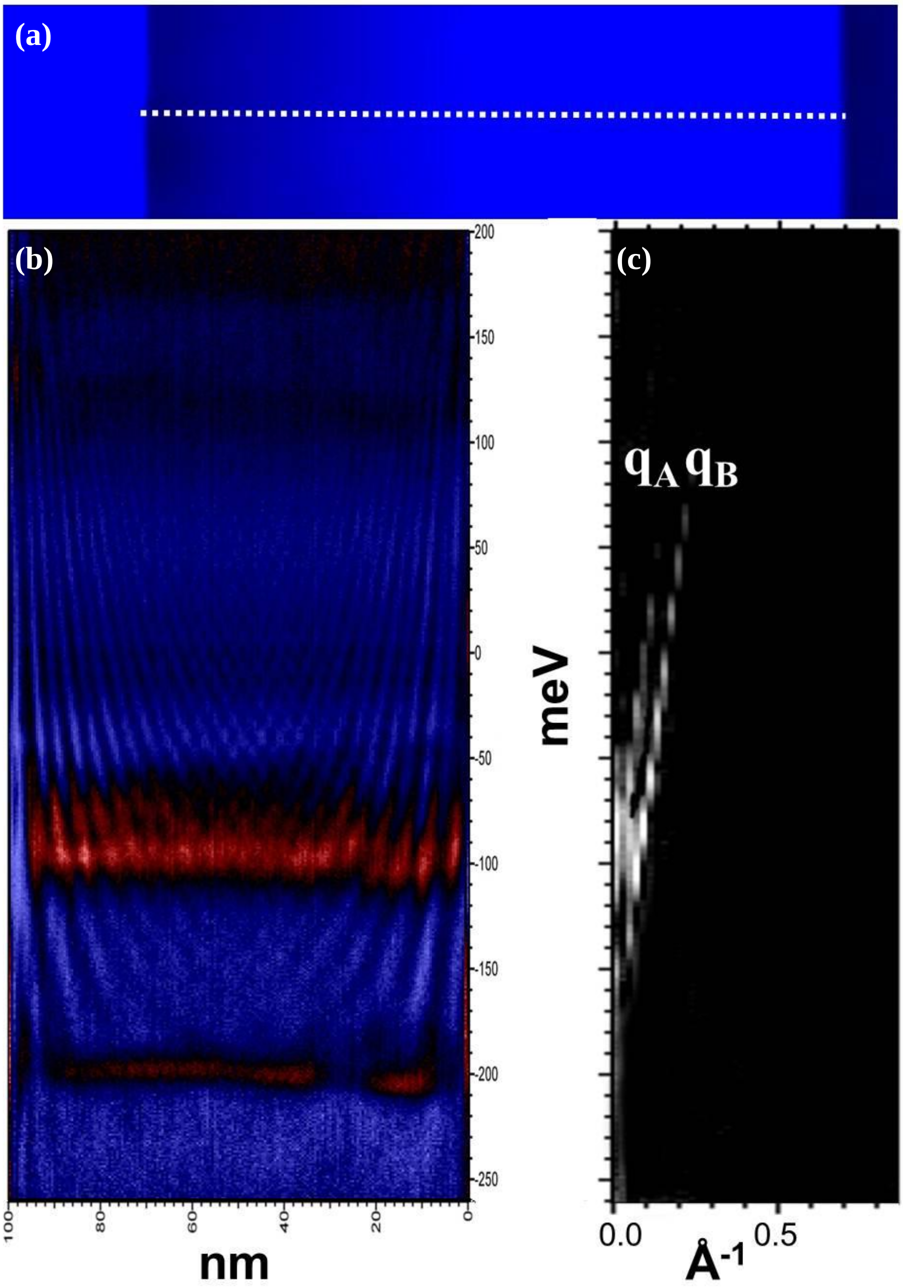

**Fig. 3.9 (a)** The STM topography (120 nm × 30 nm) of the Sb(111) surface. **(b)** Spatial-and energy-resolved *dI/dV* spectrum along the white dashed line perpendicular to step edges in (a), displaying interference in space and quantization in energy. The distance of this measurement is 100nm with 400 equal-space example spots, meaning the distance resolution is 2.5 Å. **(c)** Energy-resolved FFT of (b) shows quantization of scattering wave and the two linear dispersion relations both have a slope of 1.2eVÅ.

The confinement caused by the terrace width $L$ is key to determine the allowed scattering vectors, which should be constrained as $q_n=2\pi n/L$ (where n is a positive integer) and hence induce the quantized energy $E_n$ due to Eq. (3.1). Besides, the lifetime of the state is of interest as it determines the mean free path of the SSs electrons. If each resonant peak extracted from Fig. 3.9(b-c) is fitted to a Lorentzian function, the peak-width value, $\Gamma$, at Fermi energy can be determined to be about 5 meV, which leads to the lifetime, $\tau$, to be 132 fs since $\Gamma \approx \hbar / \tau$, subsequently yielding a mean free path, $l$, of about 24 nm, provided that $l = v_F \cdot \tau$. Compared with Seo's work[11], where the peak-width of a 11 nm terrace is 19.4 mV and that of a 15 nm one is 14.3 mV, $\Gamma$ here at a 100 nm terrace is still underestimated to some extent since the lock-in amplifier is modulated at a peak-to-peak amplitude of 5 mV, giving the upper limit. Nevertheless, this resultant mean free path is still believed to be less than the terrace size, 100 nm in our Sb(111) films, indicating that although step edge act as the scattering source here, there are other fundamental factors to contribute in the inelastic scattering process and to reduce the mean free path significantly. As suggested in 3D TIs $Sb_2Te_3$[25], $Bi_2Se_3$[26,27] and even noble metals[24], electron-electron interaction (EEI) accounts quite well for the enhanced energy width broadening and thus the reduced mean free path. This is striking given the fact that EEI stills plays a dominating role in determining the inelastic scattering even in a system with a gap and Dirac dispersion, where the gap limits the SSs-BSs scattering while the Dirac dispersion constrains the SSs-SSs scattering because of the spin conservation law. Considering 30BL Sb(111) can be regarded as the bulk material and thus is a semimetal with a distorted Dirac point, the EEI effect can be also explicitly assigned to the main factor that induces the significantly reduced mean free path for the SSs electrons of Sb(111). Here, the semimetal property provides more channels for SSs-BSs scattering while the distorted Dirac point provides more channels for SSs-SSs scattering.

### 3.3.2 2D scattering via defects on terraces of Sb (111) films

In the presence of nonmagnetic point and edge impurities for TSSs, the topological suppression of ***q*** corresponding to scatterings between opposite spin directions can be revealed using FT-STS. The 1D scattering via step edges is shown in the last part but lacks other scattering directions in momentum space, since it just reflects the scattering perpendicular to step edges, which only corresponds to the $\overline{\Gamma}-\overline{\mathrm{M}}$ direction. The information of that along $\overline{\Gamma}-\overline{\mathrm{K}}$ is also helpful to unveil the underlying scattering principles. So next the 2D scattering via defects on terraces using FT-STS will be covered in this part, aiming at identifying the origins of distinct scattering channels both along $\overline{\Gamma}-\overline{\mathrm{M}}$ and $\overline{\Gamma}-\overline{\mathrm{K}}$.

The principle of FT-STS has been introduced before. Here the coexistence of atomic resolution and QPI patterns on 30BL Sb(111) can be seen in Fig. 3.10(a). Shown in Fig. 3.10(b) is the FFT of Fig. 3.10(a), which obviously demonstrates both the atomic and QPI signals, where the former corresponds to the outer six points while the latter corresponds to the inner patterns near the center $\bar{\Gamma}$. The FBZ is marked as the yellow-line hexagon. The first remarkable aspect is that the values of scattering vectors are normally less than 0.4 Å$^{-1}$. Compared with the size of FBZ (0.84 Å$^{-1}$ along $\bar{\Gamma}-\bar{\mathrm{M}}$ and 0.97 Å$^{-1}$ along $\bar{\Gamma}-\bar{\mathrm{K}}$), they are very small. Since the QPI patterns are our main concern, the detailed investigation of the inner part in Fig. 3.10(b) will be performed next. The second remarkable aspect is that the dominating scattering channels are along $\bar{\Gamma}-\bar{\mathrm{M}}$, and the reason will be introduced later.

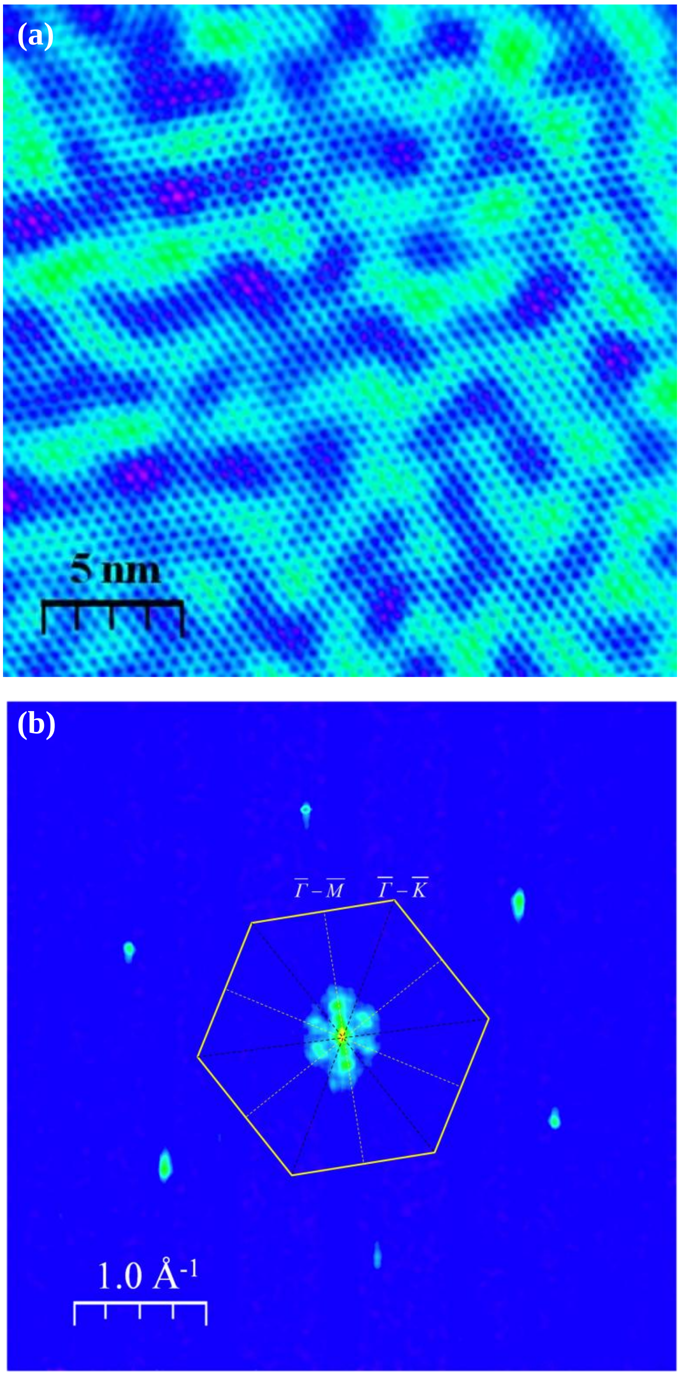

**Fig. 3.10 (a)** The *dI/dV* mapping (20nm×20nm) taken at +40mV, 120pA and **(b)** the corresponding FT-STS image. FBZ as well as the high symmetry directions $\bar{\Gamma}-\bar{M}$ and $\bar{\Gamma}-\bar{K}$ is marked to help understand the range for the scattering events.

A series of QPI patterns under different biases are given in Fig. 3.11, and the directions are marked in Fig. 3.11(a) for reference. All these images (with the bias applied on the sample) are obtained at the same area (40 nm × 40 nm) on 30BL Sb(111), so it is natural for us to consider that they are formed on the upper surface of bulk Sb only, since the lower surface has little effect on the patterns achieved here due to the localized SSs on each surface. In this sense, we can treat the QPI patterns in Fig. 3.11 as the intra-surface interference.

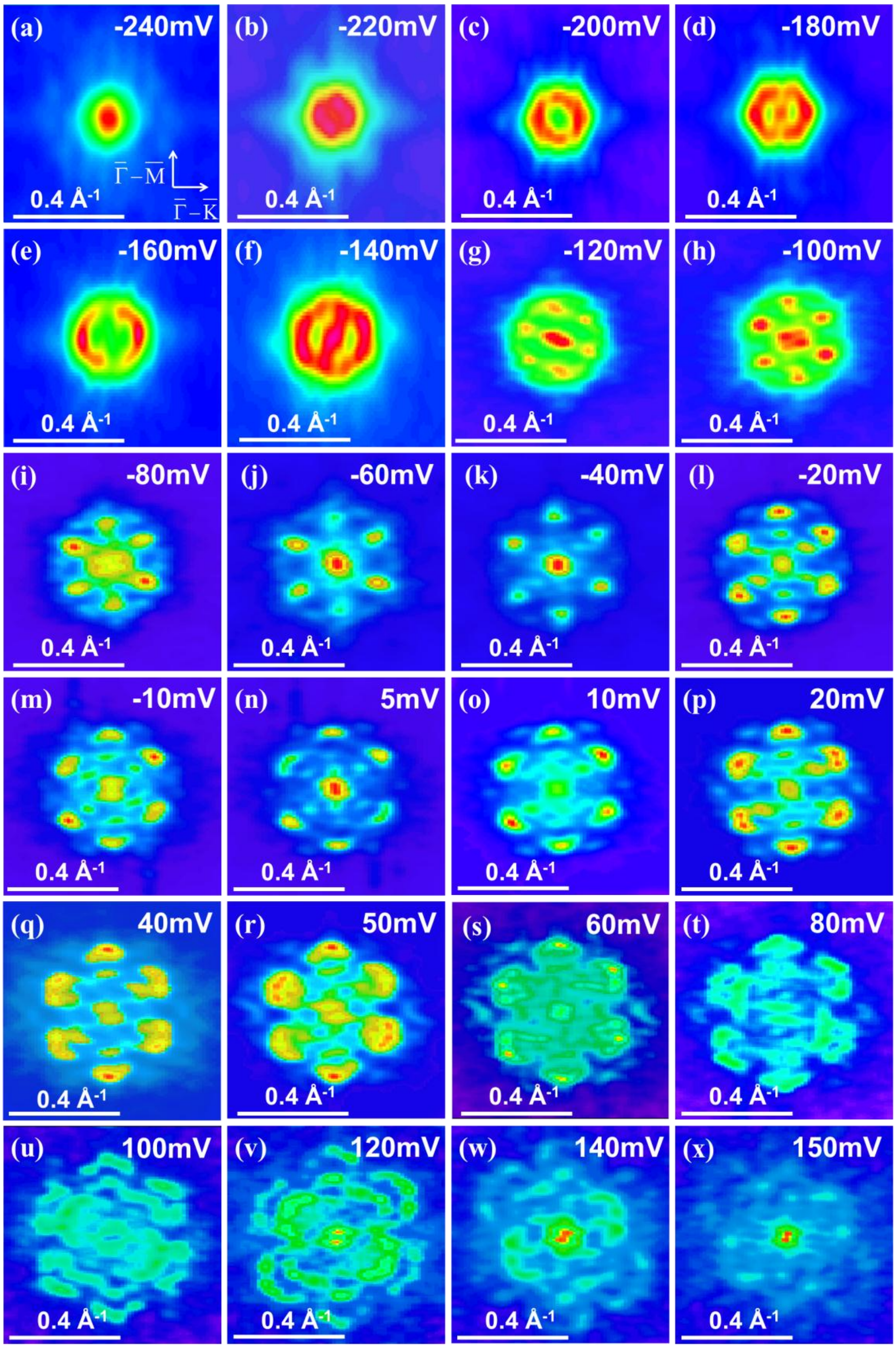

**Fig. 3.11** Bias-dependent FT-STS measurements on 30BL Sb (111). **(a)** A circular pattern indicates the position of the Dirac point. **(b-x)** The evolution of the QPI patterns. From (g) -120meV, all patterns consist of six strong intensities along $\bar{\Gamma}-\bar{M}$ and weak intensities along $\bar{\Gamma}-\bar{K}$.

Above the threshold energy around the position of the Dirac point, here -240 meV [Fig. 3.11(a)], which corresponds to a small circular pattern, six-fold symmetric patterns with dominating intensity along the $\bar{\Gamma}-\bar{\mathrm{M}}$ directions can be revealed in the FT-STS power spectra. Specifically, unlike $Bi_2Se_3$ and $Bi_2Te_3$, here we can observe weaker intensity distributions along $\bar{\Gamma}-\bar{\mathrm{K}}$ as well which are ultimately determined by the Sb band structure and the spin texture associated with it. Remarkably, at energies starting around -40 meV [Fig. 11(k)], an inner set of patterns also along $\bar{\Gamma}-\bar{\mathrm{M}}$ appear. For TSSs, it is generally accepted that, without magnetic field or magnetic impurities, scatterings between states must obey spin conservation. That is, the scattering intensity of an electron from the state of wave vector $\boldsymbol{k}$ and spin $\boldsymbol{S_k}$ to the state of $\boldsymbol{k'}$ and $\boldsymbol{S_{k'}}$ depends on $\theta_{s_{k'}}-\theta_{s_k}$, the angle between $\boldsymbol{S_k}$ and $\boldsymbol{S_{k'}}$, as[10,28]:

$$P(\boldsymbol{k},\boldsymbol{k'}) \propto \left|\left\langle \boldsymbol{S}_{\boldsymbol{k'}} \middle| \boldsymbol{S}_{\boldsymbol{k}} \right\rangle\right|^2 = \cos^2\left[\left(\theta_{s_{k'}}-\theta_{s_k}\right)/2\right] \tag{3.2}$$

The two characteristic CECs both above the Dirac point are schematically shown in Fig. 3.12(a) and (b). Specifically, the latter is taken under a lower energy level which is nearer to the Dirac point. The reason for the revolution of the CEC shapes from Fig. 3.12(a) to (b) is that, considering the CECs above the Dirac point, from the higher to lower energy contour, the six hole pockets along $\bar{\Gamma}-\bar{\mathrm{M}}$ approach the $\bar{\Gamma}$ point, connect to each other, and eventually converge on the Dirac point. Thus the electron pocket around $\bar{\Gamma}$ is smaller in Fig. 3.12(b) than that in Fig. 3.12(a), and the outer hexagon in Fig. 3.12(b) is actually the connected part from the six hole pocket cusps in Fig. 3.12(a). To explicitly illustrate the scattering channels, the zoom-in CECs as well as the spin texture only around $\bar{\Gamma}$ are shown in Fig. 3.12(c-d). From Fig. 3.12(c) we can find that the scattering intensity of $\mathbf{q_A}$ (black arrows at higher position) should be weaker than that of $\mathbf{q_B}$ (black arrows at lower position) because of the misorientation angle of spin directions. Specifically, $\mathbf{q_A}$ represents the scattering between the outer hole pockets in the $\bar{\Gamma}-\bar{M}$ direction and $\mathbf{q_B}$ represents that between the central electron pocket and outer hole pockets. Since $\mathbf{q_A}$ has a spin direction misalignment of 60 °, giving a spin probability factor of ¾, while the latter one has 0 °, giving a probability of 1, the two scattering vectors should be both observable along $\bar{\Gamma}-\bar{M}$. However, still along $\bar{\Gamma}-\bar{M}$, the scattering corresponding to $\mathbf{q_D}$ (red arrows in Fig. 3.12(c)) is totally forbidden due to the opposite spins of two relevant states. Besides, $\mathbf{q_C}$ (green arrows in Fig. 3.12(c)) represents the scattering between the "next-nearest-neighbor" hole pockets, which is obviously along $\bar{\Gamma}-\bar{K}$ and has a spin direction difference of 120 °, giving a probability of ¼. This should correspond to scattering patterns of weaker intensities along $\bar{\Gamma}-\bar{K}$.

Indeed, there are two sets of strong intensities (Fig. 3.11(l-v)) along $\bar{\Gamma}-\bar{M}$ and weak ones along $\bar{\Gamma}-\bar{K}$ (Fig. 3.11(l-t)) in the FT-STS mapping. Particularly, the mappings taken at 20 mV and -60 mV are selected for comparison as shown in Fig. 3.12(e-f), respectively. In Fig. 3.12(c), It is obvious that $\mathbf{q_A} < \mathbf{q_B}$, and hence $\mathbf{q_A}$ corresponds to the inner set of patterns that has smaller values compared with the outer set in Fig. 3.12(e). Besides, the weak $\mathbf{q_C}$ can also be observed in Fig. 3.12(e). Moreover, when the CEC approaches the Dirac point as shown in Fig. 3.12(d), $\mathbf{q_B}$ (black arrows in

Fig. 3.12(d)) is still distinguishable because of the definite value under any allowed energy, whereas $\mathbf{q_A}$ (red arrows in Fig. 3.12(d)) is not because of the changeable values since the initial and final momenta can be selected continuously. So in Fig. 3.12(f) only the intensity marked as $\mathbf{q_B}$ can be observed. In addition, that is also why in Fig. 3.9(c) $\mathbf{q_A}$ appears at a higher energy compared with $\mathbf{q_B}$.

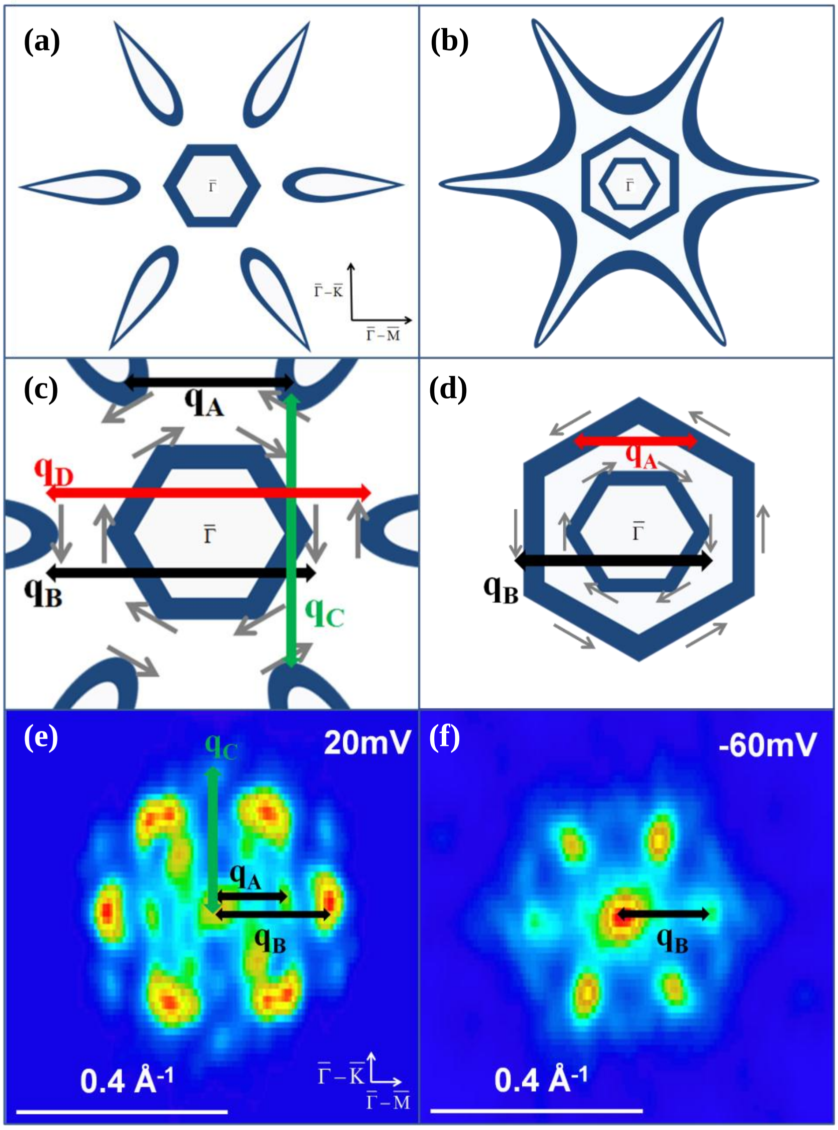

**Fig. 3.12 (a-b)** Schematics of CECs at **(a)** a higher energy and **(b)** a lower one. **(c-d)** Zoom-in CECs as well as the spin texture only around $\bar{\Gamma}$ for (a-b). The small grey arrows represent the spin directions. **(c)** $\mathbf{q_A}$ and $\mathbf{q_B}$ (both black arrows) are allowed scattering vectors along $\bar{\Gamma}-\bar{M}$, while $\mathbf{q_C}$ (green arrows) with a much less probability along $\bar{\Gamma}-\bar{K}$ and $\mathbf{q_D}$ (red arrows) is totally forbidden. **(d)** $\mathbf{q_A}$ and $\mathbf{q_B}$ are still allowed along $\bar{\Gamma}-\bar{M}$, where values of $\mathbf{q_A}$ are continuous while those of $\mathbf{q_B}$ are definite. **(e-f)** FT-STS mappings at **(e)** 20 mV and **(f)** -60 mV are shown for comparison with (c-d), respectively. The observable scattering vectors are marked.

Besides, plotting the dispersion obtained from Fig. 3.13(a) gives us two slopes, 1.29 eVÅ [Fig. 3.13(b)] and 1.22 eVÅ [Fig. 3.13(c)], which are again comparable with the data previously obtained from 1D step-edge scattering in Fig. 3.9(c). These phenomena unambiguously illustrate that scatterings of TSSs have much larger probabilities of taking place between states with similar spin directions.

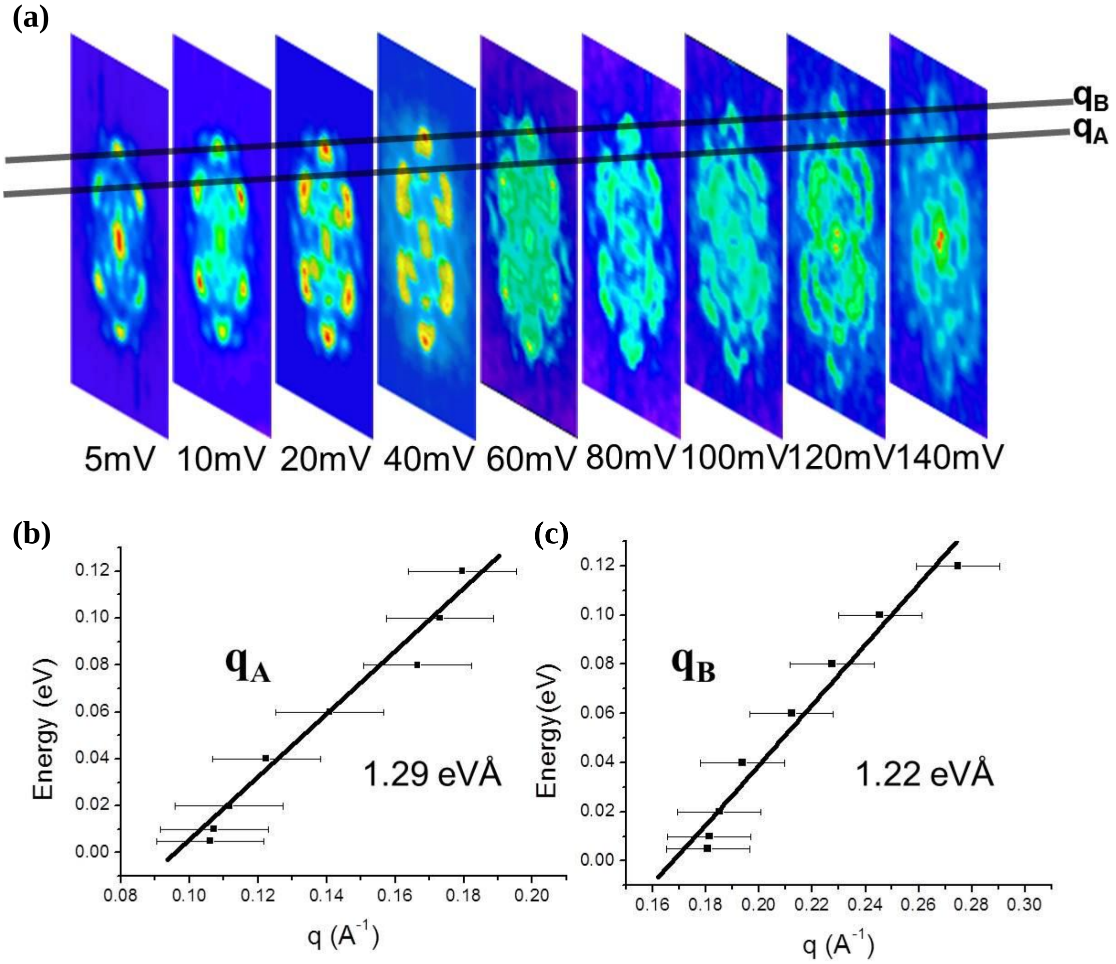

**Fig. 3.13 (a)** The FT-STS maps in Fig. 3.11 at the bias from 5mV and 140mV are selected to generate the linear dispersion relationship. Each map shows two sets of scattering vectors corresponding to $\mathbf{q_A}$ and $\mathbf{q_B}$, respectively. The slopes of $\mathbf{q_A}$ **(b)** and $\mathbf{q_B}$ **(c)** extracted from (a). Here the error bar corresponds to 0.05π Å$^{-1}$, which is determined by (2π/40) nm$^{-1}$.

Moreover, the explanation to these QPI patterns can also be fulfilled by the combination of both experimental and theoretical methods. Hence, for comparison, the first-principles calculations are used in this project. Fig. 3.14(a) shows the surface bands of 30BL Sb(111) with emphasis on the high symmetry points $\overline{\Gamma}$, $\overline{\mathrm{K}}$ and $\overline{\mathrm{M}}$. Then derived from the Fermi energy contour which is similar to the schematic in Fig. 3.12(a), the DFT simulations of the QPI according to the spin-angle dependence of scattering probability as in Eq. (3.2) are given in Fig. 3.14(c) and (e). The energy levels are selected to be 5 meV and 80 meV, based on the consideration of verifying the accuracy of calculations in energies both near and away from $E_F$.

Compare the experimental data in Fig. 3.14(b) and (d) with the simulation data in Fig. 3.14(c) and (e), and we can find several interesting aspects that are in common. Firstly, along $\overline{\Gamma}-\overline{\mathrm{M}}$ six dominating scattering vectors, $\mathbf{q_B}$ (marked as black arrows), can be seen as indicated by the brighter colors in both cases. Secondly, at higher energy in Fig. 3.14(d-e), the scattering vectors have a more dispersing intensity mainly centered but not solely confined along $\overline{\Gamma}-\overline{\mathrm{M}}$, which are different from those at 5 meV. Thirdly, still at higher energy in Fig. 3.14(d-e), weak scattering vectors, $\mathbf{q_C}$ (marked as green arrows), begin to appear at the outer part along $\overline{\Gamma}-\overline{\mathrm{K}}$. These three common features demonstrate the essential agreement between the two approaches when they are used to interpret the underlying interference principles.

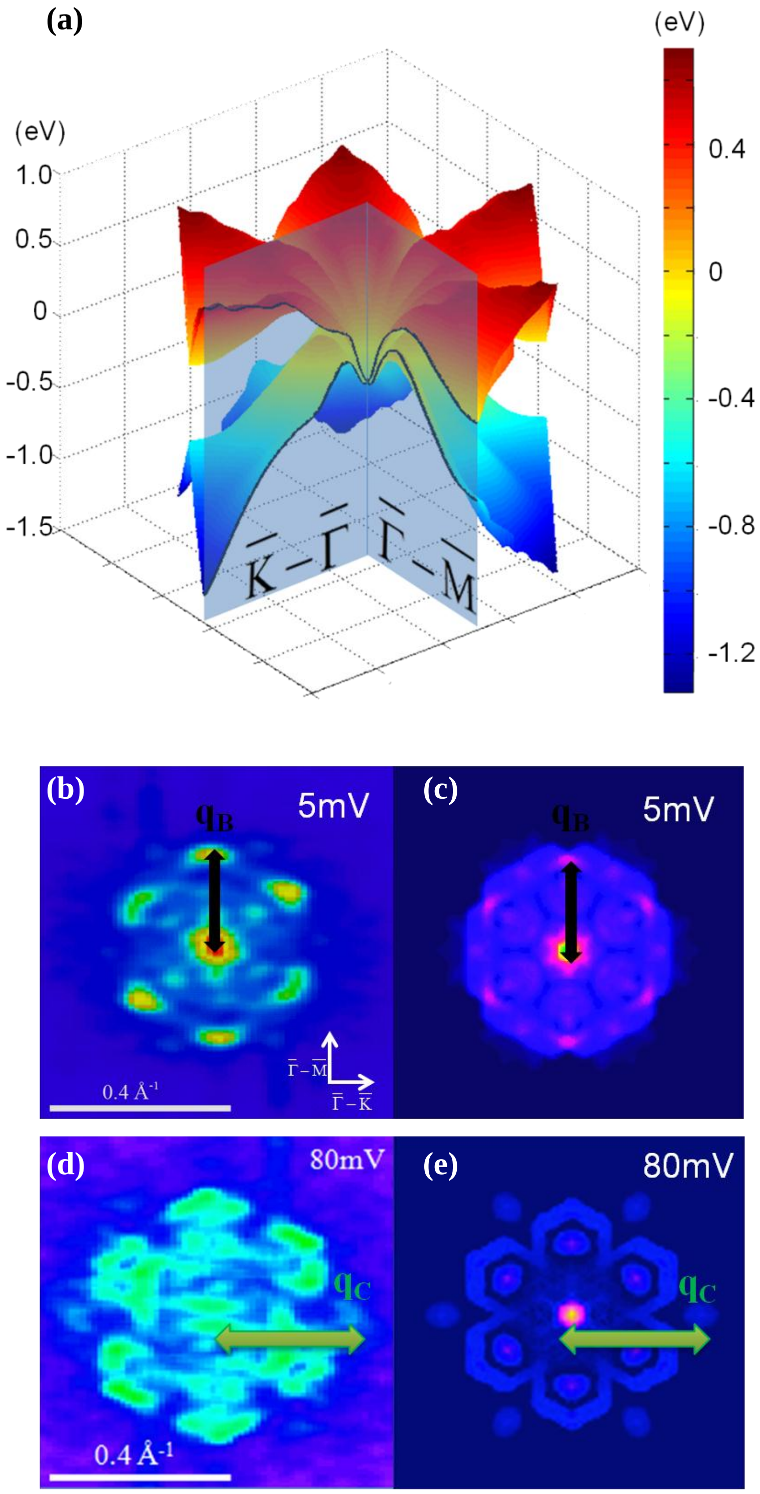

**Fig. 3.14** **(a)** Calculated surface bands of 30BL Sb(111). **(b)** The FT-STS mapping taken at 5mV and **(c)** the corresponding calculated QPI patterns. **(d)** The FT-STS mapping taken at 80mV and **(e)** the corresponding calculated QPI patterns. $\mathbf{q_B}$ and $\mathbf{q_C}$ are marked for comparison.

According to the characterization of QPI patterns by both experimental 1D/2D scattering and first-principles calculations, the invisibility of time-reversed paths of backscattering trajectories on Sb(111) due to the topological Berry's phase is explicitly elucidated. Hence, SSs on Sb(111) are confirmed as the TSSs, which may offer a simple yet appropriate system for realization of quantum effects that people have been imagining.

### 3.3.3 Magnetic adsorbates on Sb (111) films

The TR symmetry in TIs can be broken by magnetic scattering centers on the surface (surface doping) and in the bulk (bulk doping), or by an external magnetic field. Indeed, by proper bulk doping of Fe or Mn, the conducting massless Dirac fermions can be changed to insulating massive Dirac fermions, meaning a gap can be opened, in existing 3D TI materials such as $Bi_2Se_3$[29] and $Bi_2Te_3$[30-32]. Additionally, by external magnetic field, Landau quantization[25,33,34] can also be achieved which reflects the Dirac fermion nature of the SS electrons in 3D TIs.

However, regarding the effect of the magnetic moment of an impurity to the local scattering properties, the surface doping is a complicated problem compared with other two methods. Because due to the doping effect of impurities on top, TSSs are easily affected by new states that become occupied, which would make it difficult to analyze the exact influence of the deposited magnetic materials. Besides, the localized change of scattering would be beyond the detection ability of some surface-sensitive techniques such as ARPES. Additionally, even if the localized change could be observed using STM/STS, it is hard to determine if the resultant scattering channels come from new SSs-BSs or SSs-SSs scattering. Nevertheless, it is still of vital importance for us to probe the effect of surface doping, because it is more relevant for the practical field where TIs need to be in contact with ferromagnets or superconductors for device applications. Therefore, here the advantage of STM for investigating localized electronic properties is used. From Eq. (3.2), we know for TSSs, QPI patterns corresponding to $\theta_{s_{k'}} - \theta_{s_k} = \pi$ are totally forbidden due to the spin conservation law. However, new patterns might be activated if TR symmetry is locally broken. Our aim is to find if there is any change in QPI patterns due to deposited magnetic materials.

When an atom or a molecule is trapped by an attractive interaction on a solid surface, it becomes an adsorbate with adsorption energy $E_{ads}$. Normally, when the adsorbate is mainly attracted by van der Waals force, $E_{ads}$ is less than 100 meV, which results in the typical physisorption and has little change in electronic configurations of both the adsorbate and substrate. However, with such magnetic adsorbate, the adsorbate-induced modulation of TSSs' LDOS may still be significantly altered, considering the underlying broken TR symmetry. Hence, in this part, MnPc molecules are deposited on the previously confirmed TSSs of Sb(111) films to investigate the probability of newly generated scattering channels.

In Fig. 3.15(a) the low coverage of manganese phthalocyanine (MnPc) molecules on the surface of 30BL Sb(111) is shown. The full occupancy of step edges illustrates that initially they act as effective trapping sites for the molecules, indicating a high mobility of MnPc on Sb(111). MnPc on terraces can be used for testing the magnetic response of TSSs. Fig. 3.15(b) shows MnPc in a higher resolution, and the cross-like bright features are well-separated individual MnPc molecules. One reason for choosing MnPc [see the schematic in the inset of Fig. 3.15(b)] is that it is a well known molecular magnet, which carries a spin 3/2 in gas phase[35] and exhibits a nonzero magnetic moment when absorbed on metal surfaces[36]. Another reason is that depositing transition metal atoms such as Mn and Fe directly may form alloy with the substrate Sb, obscuring the role of magnetic impurities as the surface scattering centers. The characteristic STS spectrum of the Sb(111) surface (which is taken more than 20 nm away from any nearby MnPc) and that of MnPc molecules are shown in Fig. 3.15(c). The main peaks at negative bias remain almost unchanged, whereas the peaks at positive bias are modified greatly by the MnPc molecule. The peak on MnPc is at 0.18 V while that on Sb is 0.10 V. The dramatic peak shift is also confirmed by the spatial-and energy-resolved *dI/dV* spectrum [Fig. 3.15(d)] taken along the white dot line in (b). Since the molecule locates at the centre of the measured line, the spectrum is almost symmetric about the central line.

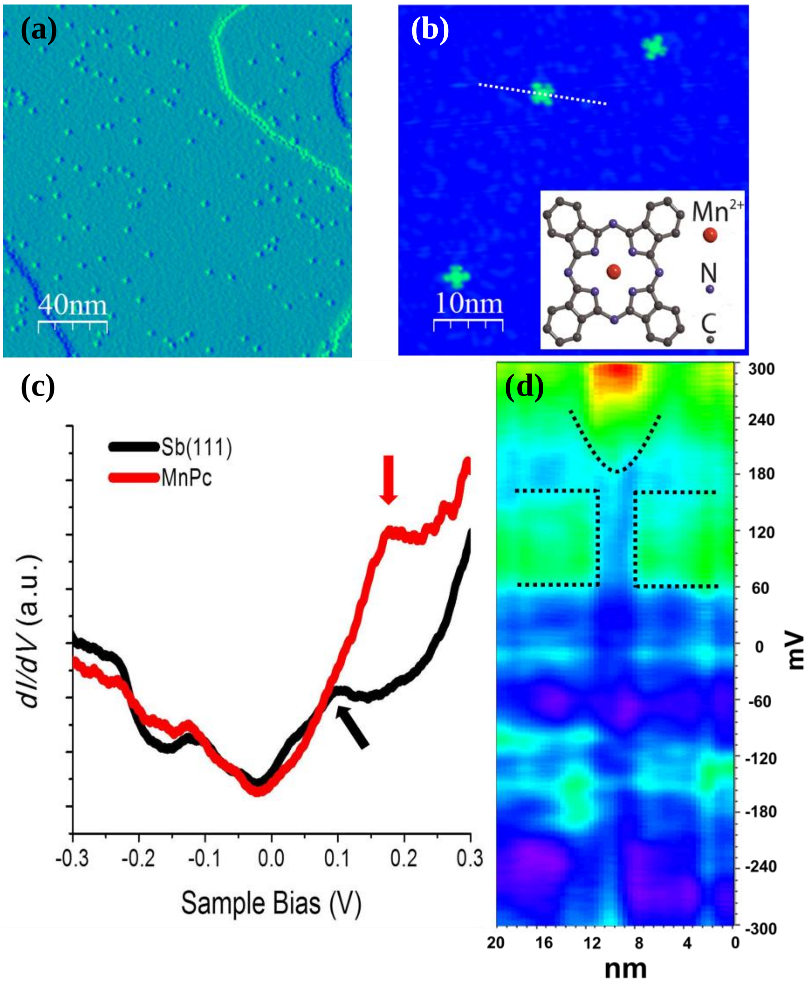

**Fig. 3.15 (a)** The low coverage of MnPc molecules on the surface of 30BL Sb(111). MnPc locates at edge steps as well as the terraces. **(b)** A high resolution image reveals the cross-like MnPc molecules. The inset image shows schematically the structure of a MnPc molecule. **(c)** The characteristic STS spectrums of both Sb(111) surface and MnPc molecules. The main change for the LDOS is that on MnPc a strong peak (red arrow) shows up at 0.18 V instead of the one at 0.10 V (black arrow) on Sb. **(d)** Spatial and energy-resolved *dI/dV* spectrum along the white dashed line in (b) also shows the peak shift of 0.08 V in the central area, which is the position of the MnPc molecule. The black dot line in (d) marks the two areas with stronger LDOS corresponding to the two labelled peaks in (c).

To enhance the possible magnetic-impurity-induced scattering events, the density of MnPc is increased as shown in Fig. 3.16(a). The peak shift can also be observed in the *dI/dV* mapping in Fig. 3.16(b) and (c), which both correspond to the same topography [Fig. 3.16(a)]. It is obvious that at 200 mV (Fig. 3.16(b)), the molecules are bright spots whereas at -80 mV (Fig. 3.16(c)) they are dark. Combined with the STS spectrum in Fig. 3.15(c), it can be determined that the MnPc molecules have much stronger LDOS at 200 mV than at -80 mV. It is also striking that the molecules do not generate any significant standing waves around them, probably due to the weak interactions between adsorbates and the substrate. The scattering patterns shown here can still be assigned to the effect of atomic defects of the Sb surface.

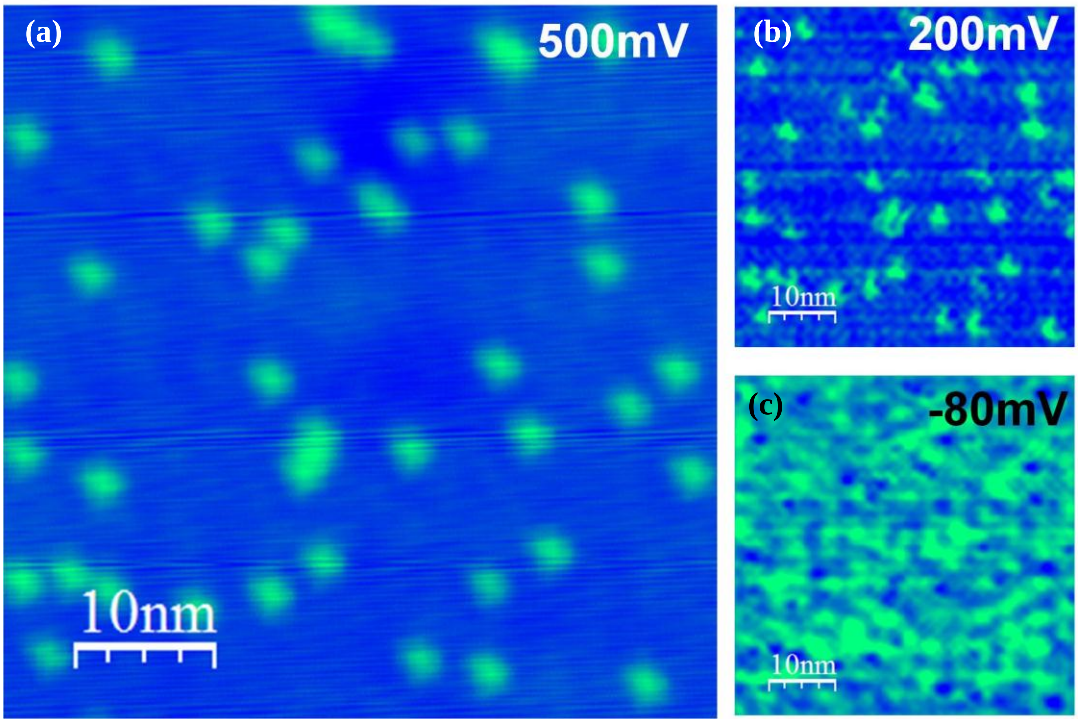

**Fig. 3.16 (a)** The STM topography of the Sb(111) surface. **(b)** *dI/dV* mapping taken on the area in (a) at the bias of 200 mV (b) and -80 mV **(c)**. The molecules have quite different LDOS at the two energy levels.

This phenomenon is confirmed in the FT-STS mapping shown in Fig. 3.17(a-f). Although there are some perturbation and corrugation induced by the large size of the molecules, some key features can still be seen. For example, at -20 meV [Fig. 3.17(a-b)], compared with Fig. 3.11(l), the two sets of strong scatterings along $\overline{\Gamma}-\overline{\mathrm{M}}$ as well as the weak ones along $\overline{\Gamma}-\overline{\mathrm{K}}$ are identical with those on the substrates without MnPc. Besides, when the bias reaches -60 mV [Fig. 3.17(c-d)] and -80 mV [Fig. 3.17(e-f)], the two sets transform into one set, which is again, similar to the situation on pure Sb(111) surface in Fig. 3.11(j) and (i), respectively. It is believed that the locally broken TR symmetry by magnetic impurities should break the spin conservation for scattering events taking place nearby, and thus give birth to scattering patterns which are solely determined by the band structure without the influence caused by the associated spin texture. However, in our MnPc/Sb system, the scatterings remain unchanged even in a high coverage magnetic molecular density, giving a strong indication that MnPc molecules cannot break the local TR symmetry as expected.

It is worth noting that since MnPc is a weakly-coupled magnetic impurity due to the configuration of the molecule, the magnetic moment of this impurity might be too weak to create significant LDOS modulations around it. In this sense, strongly-coupled magnetic impurities such as Fe are required to further test the magnetic-impurity-induced effects.

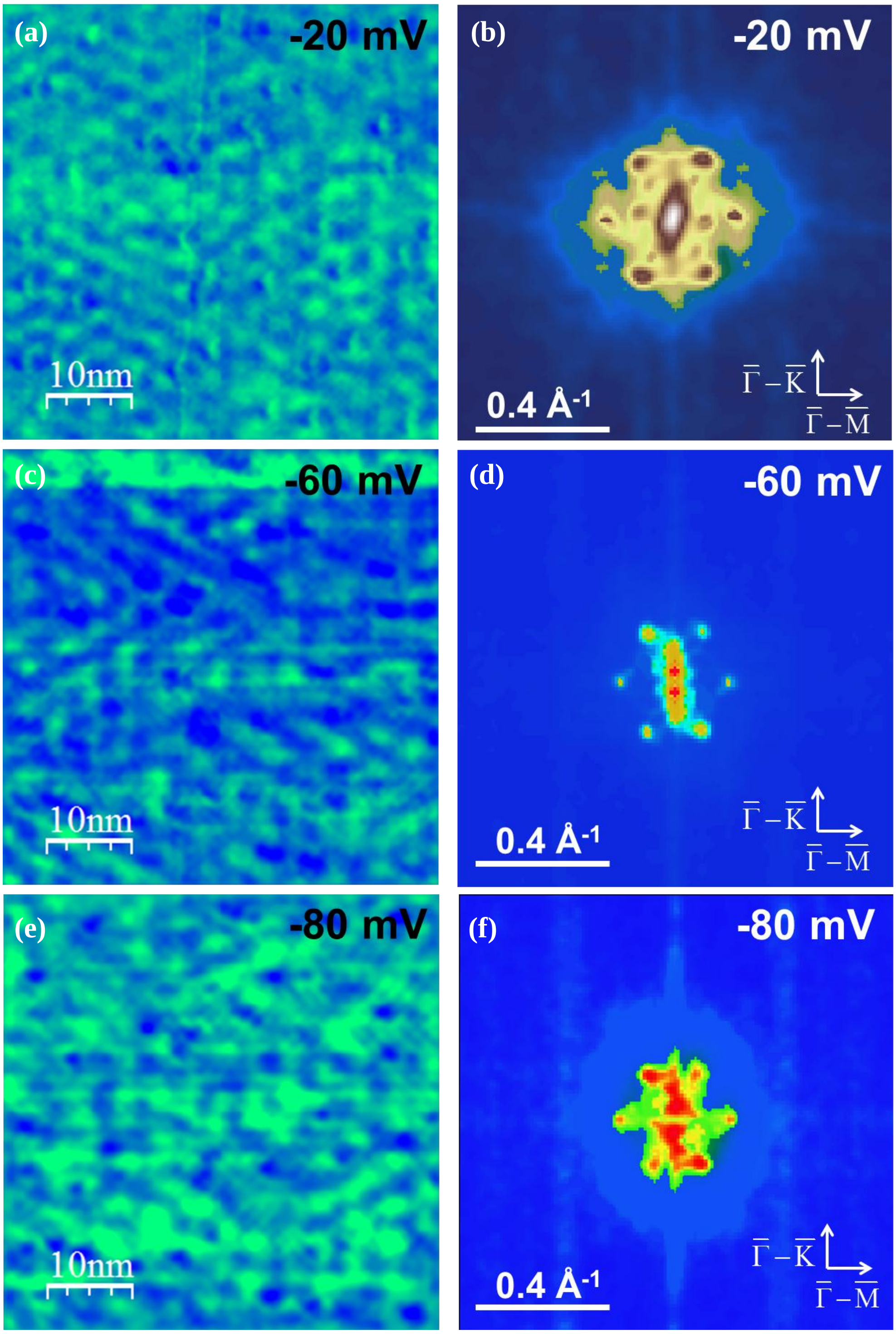

**Fig. 3.17** The *dI/dV* mapping at **(a)** -20 mV, **(c)** -60 mV and **(e)** -80 mV. The corresponding FT-STS spectrums are shown in **(b)**, **(d)** and **(f)**. The figure in **(b)** shows two sets of scattering intensities along $\bar{\Gamma}-\bar{M}$ and weak intensities along $\bar{\Gamma}-\bar{K}$. At **(d)** -60 mV and **(f)** -80 mV only one set along $\bar{\Gamma}-\bar{M}$ can be observed.

Besides, the absence of new scattering channels, e.g. stronger scattering intensity along $\bar{\Gamma}-\bar{K}$, can be explained by the recent theoretical work[16], which demonstrates that normal STM/STS is incapable of detecting magnetic-impurity-induced backscattering. Moreover, the simulation work based on Green’s function[17] indeed reveals the backscattering processes in magnetization patterns. Therefore, the magnetic-impurity-induced effects on TSSs may be observable using spin-polarized STM[37] and further work is highly required.

## 3.4 Conclusions

In this chapter *in-situ* STM/STS studies on the surface of Sb(111) thick films, which approaches the bulk surface, are illustrated. Taking advantage of 1D step edges and 2D terrace defects, the standing waves of the SSs can be observed. Using the FT-STS method, it is proved that although bulk Sb is semimetal and has a distorted Dirac cone at $\bar{\Gamma}$, it possesses TSSs on the (111) surface. Besides, the origins of observed scattering wavevectors in the FT-STS are well explained by the combination of both experimental data and first-principles calculations. Additionally, the introduction of magnetic impurities on the TSSs is performed by depositing MnPc on Sb(111). We find that the scattering patterns remain unchanged even in a high coverage molecular density, possibly due to the incapability of the normal STM/STS method.

# References

1 Stegemann, B., Ritter, C., Kaiser, B. & Rademann, K. Characterization of the (0001) cleavage surface of antimony single crystals using scanning probe microscopy: Atomic structure, vacancies, cleavage steps, and twinned interlayers. *Phys. Rev. B* **69**, 155432 (2004).

2 Isshiki, T., Nishio, K., Saijo, H. & Shiojiri, M. Growth and crystallographic, surface and defect structures of antimony particles deposited in a high-resolution transmission electron microscope. *Thin Solid Films* **237**, 155-159 (1994).

3 Bardotti, L., Jensen, P., Hoareau, A., Treilleux, M. & Cabaud, B. Experimental Observation of Fast Diffusion of Large Antimony Clusters on Graphite Surfaces. *Phys. Rev. Lett.* **74**, 4694-4697 (1995).

4 Heyde, M., Cappella, B., Sturm, H., Ritter, C. & Rademann, K. Dislocation of antimony clusters on graphite by means of dynamic plowing nanolithography. *Surf. Sci.* **476**, 54-62 (2001).

5 Kaiser, B., Stegemann, B., Kaukel, H. & Rademann, K. Instabilities and pattern formation during the self-organized growth of nanoparticles on graphite. *Surf. Sci.* **496**, L18-L22 (2002).

6 Wang, X. S., Kushvaha, S. S., Yan, Z. & Xiao, W. Self-assembly of antimony nanowires on graphite. *Appl. Phys. Lett.* **88**, 233105-233103 (2006).

7 Sugawara, K. *et al.* Fermi Surface and Anisotropic Spin-Orbit Coupling of Sb(111) Studied by Angle-Resolved Photoemission Spectroscopy. *Phys. Rev. Lett.* **96**, 046411 (2006).

8 Hsieh, D. *et al.* Observation of unconventional quantum spin textures in topological insulators. *Science* **323**, 919-922 (2009).

9 Hsieh, D. & et al. Direct observation of spin-polarized surface states in the parent compound of a topological insulator using spin- and angle-resolved photoemission spectroscopy in a Mott-polarimetry mode. *New J. Phys.* **12**, 125001 (2010).

10 Gomes, K. K. *et al.* Quantum imaging of topologically unpaired spin-polarized Dirac fermions. *arXiv:0909.0921v2* (2009).

11 Seo, J. *et al.* Transmission of topological surface states through surface barriers. *Nature* **466**, 343-346 (2010).

12 Hasan, M. Z. & Kane, C. L. Colloquium: Topological insulators. *Rev. Mod. Phys.* **82**, 3045 (2010).

13 Moore, J. Topological insulators: The next generation. *Nat. Phys.* **5**, 378-380

(2009).

14 Kresse, G. & Furthmüller, J. Efficient iterative schemes for ab initio total-energy calculations using a plane-wave basis set. *Phys. Rev. B* **54**, 11169-11186 (1996).

15 Perdew, J. P., Burke, K. & Ernzerhof, M. Generalized Gradient Approximation Made Simple. *Phys. Rev. Lett.* **77**, 3865-3868 (1996).

16 Liu, Q., Qi, X.-L. & Zhang, S.-C. Stationary phase approximation approach to the quasiparticle interference on the surface of a strong topological insulator. *Phys. Rev. B* **85**, 125314 (2012).

17 Stróżecka, A., Eiguren, A. & Pascual, J. I. Quasiparticle Interference around a Magnetic Impurity on a Surface with Strong Spin-Orbit Coupling. *Phys. Rev. Lett.* **107**, 186805 (2011).

18 Friedel, J. The distribution of electrons round impurities in monovalent metals. *Philos. Mag.* **43**, 153 (1952).

19 Crommie, M. F., Lutz, C. P. & Eigler, D. M. Imaging standing waves in a two-dimensional electron gas. *Nature* **363**, 524-527 (1993).

20 Petersen, L. *et al.* Direct imaging of the two-dimensional Fermi contour: Fourier-transform STM. *Phys. Rev. B* **57**, R6858-R6861 (1998).

21 Crommie, M. F., Lutz, C. P. & Eigler, D. M. Confinement of Electrons to Quantum Corrals on a Metal Surface. *Science* **262**, 218-220 (1993).

22 Hasegawa, Y. & Avouris, P. Direct observation of standing wave formation at surface steps using scanning tunneling spectroscopy. *Phys. Rev. Lett.* **71**, 1071-1074 (1993).

23 Burgi, L., Jeandupeux, O., Brune, H. & Kern, K. Probing hot-electron dynamics at surfaces with a cold scanning tunneling microscope. *Phys. Rev. Lett.* **82**, 4516-4519 (1999).

24 Burgi, L., Jeandupeux, O., Hirstein, A., Brune, H. & Kern, K. Confinement of surface state electrons in Fabry-Perot resonators. *Phys. Rev. Lett.* **81**, 5370-5373 (1998).

25 Jiang, Y. *et al.* Landau Quantization and the Thickness Limit of Topological Insulator Thin Films of $Sb_2Te_3$. *Phys. Rev. Lett.* **108**, 016401 (2012).

26 Liu, M. *et al.* Electron interaction-driven insulating ground state in $Bi_2Se_3$ topological insulators in the two-dimensional limit. *Phys. Rev. B* **83**, 165440 (2011).

27 Wang, J. *et al.* Evidence for electron-electron interaction in topological insulator thin films. *Phys. Rev. B* **83**, 245438 (2011).

28 Roushan, P. *et al.* Topological surface states protected from backscattering by chiral spin texture. *Nature* **460**, 1106 (2009).

29 Chen, Y. L. *et al.* Massive Dirac Fermion on the Surface of a Magnetically Doped Topological Insulator. *Science* **329**, 659-662 (2010).

30 Hsieh, D. *et al.* Observation of Time-Reversal-Protected Single-Dirac-Cone Topological-Insulator States in $Bi_2Te_3$ and $Sb_2Te_3$. *Phys. Rev. Lett.* **103**, 146401 (2009).

31 Okada, Y. *et al.* Direct Observation of Broken Time-Reversal Symmetry on the Surface of a Magnetically Doped Topological Insulator. *Phys. Rev. Lett.* **106**, 206805 (2011).

32 Hor, Y. S. *et al.* Development of ferromagnetism in the doped topological insulator $Bi_{2-x}Mn_xTe_3$. *Phys. Rev. B* **81**, 195203 (2010).

33 Cheng, P. *et al.* Landau Quantization of Topological Surface States in $Bi_2Se_3$. *Phys. Rev. Lett.* **105**, 076801 (2010).

34 Hanaguri, T., Igarashi, K., Kawamura, M., Takagi, H. & Sasagawa, T. Momentum-resolved Landau-level spectroscopy of Dirac surface state in Bi2 Se3. *Phys. Rev. B* **82**, 081305.

35 Barraclough, C. G., Martin, R. L., Mitra, S. & Sherwood, R. C. Paramagnetic Anisotropy, Electronic Structure, and Ferromagnetism in Spin S = (3/2) Manganese(II) Phthalocyanine. *J. Chem. Phys.* **53**, 1638-1642 (1970).

36 Franke, K. J., Schulze, G. & Pascual, J. I. Competition of Superconducting Phenomena and Kondo Screening at the Nanoscale. *Science* **332**, 940-944 (2011).

37 Wiesendanger, R. Spin mapping at the nanoscale and atomic scale. *Rev. Mod. Phys.* **81**, 1495 (2009).

# Chapter 4

# STM/STS investigations of Sb (111) thin films

## 4.1 Introduction

### 4.1.1 Towards 2D limit for TSSs

In the field of practical applications, topologically nontrivial thin films are more suitable building blocks than bulk materials since the real device architectures require these thin films in good contact with large-moment ferromagnets and superconductors to form junction or valve structures. In this regard, approaching 2D limit for 3D TIs has been extensively explored[1-12]. Theoretical calculations predict that the Dirac cones will turn into Dirac hyperbolas and a gap due to the coupling will open up at $\bar{\Gamma}$ point in the ultrathin limit induced by inter-surface coupling[1,7], even in an oscillatory way[9,13,14]. Indeed, by ARPES measurements, the thickness-dependent bandgap can be observed in both $Bi_2Se_3$[4,10] and $Bi_2Te_3$[3] thin films. However, ARPES can only provide us with an overall view of this gap opening process in the band structure but cannot give detailed information on the inter-surface coupling effect for TSSs, which apparently involves the spin texture besides the band structure. In this sense, STM/STS should be employed in this particular subject because it is capable of revealing the local topological properties more precisely, and can analyze the spin information associated with the scattering events by a combination of STS with DFT-based simulation approaches[15,16].

From the work described in Chap. 3, it is clear that the SSs on Sb(111) are indeed TSSs which are protected by TR symmetry. Actually the Sb(111) thin film is an ideal model to investigate the detailed physical properties when approaching 2D limit, especially the inter-surface interaction. Because on one hand, the distorted Dirac cone it possesses can create various scattering channels for us to reveal the underlying scattering principles. On the other hand, as described in Chap. 1, taking advantage of the QCE, the negative indirect bandgap in bulk Sb can be tuned and transformed into a positive bandgap, offering the possibility of making Sb a real TI. From

$$\begin{aligned} E_g^{eff} &= \min(E_e) - \max(E_h) \\ &= (E_C + \frac{\pi^2\hbar^2}{2m_0 m_e^* a^2}) - (E_V - \frac{\pi^2\hbar^2}{2m_0 m_h^* a^2}) \\ &= (E_C - E_V) + \frac{\pi^2\hbar^2}{2m_0 a^2}\left(\frac{1}{m_e^*} + \frac{1}{m_h^*}\right) \\ &= E_g^{bulk} + \frac{\pi^2\hbar^2}{2m_0 a^2}\left(\frac{1}{m_e^*} + \frac{1}{m_h^*}\right) \end{aligned} \tag{4.1}$$

where $E_g^{bulk}$ = -174 mV, $m_e^*$ = 0.073 and $m_h^*$ = 0.120 according to the previous report[17], we know the critical thickness "*a*" for Sb(111) to possess a positive gap is around 6.7 nm, which is approximately 18BL. This rough estimation gives us a reference to fabricate thin films with appropriate thickness.

Similar to those in $Bi_2Se_3$ and $Bi_2Te_3$, TSSs on upper and lower surfaces in the Sb(111) thin film will couple together eventually when the film is thin enough. Previous calculation studies[18] demonstrate that the spin-polarized SSs will degenerate to spin-unpolarized quantum well states (QWSs) in 20BL Sb(111). Here, SSs of much thinner films are exploited, in order to unveil the detailed vanishing process of spin polarization from TSSs to QWSs.

In terms of Sb(111) growth, there remains some obstacles to obtain ultrathin films. The surface energy of Sb is 0.54-0.66 J $m^{-2}$, which is fairly low compared with that of other metals or semiconductors. On one hand, due to the chemical inactivity, a 3D islanding growth mode is expected on inert surfaces such as Si(111)-√3×√3:Bi-β. On the other hand, substrates with higher surface energy might lead to a layer-by-layer growth mode due to strong interface binding, but this also induces a larger structure inversion asymmetry (SIA)[4,7], which can lift the degeneracy of two Dirac cones belonging to two surfaces. The resulting new features may mix up with those generated by inter-surface coupling and obscure the main problem we focus on. Therefore, we need to develop a proper deposition scheme to achieve relatively free-standing thin films to exclude the influence caused by SIA.

### 4.1.2 Outline

In this chapter, the results of our *in-situ* STM/STS investigations of Sb thin films in UHV systems are presented. In the first part, the growth method for the atomic flat Sb(111) thin films using the cracked Sb source are shown. Then the second part will focus on the FT-STS investigations of 9BL Sb(111) deposited on Si(111)-√3×√3:Bi-β. Compared with the results on 30BL Sb, the QPI patterns here have very different distributions of intensities in the momentum space, unambiguously indicating that the intra- and inter-surface interference dominate in the thick and thin film cases, respectively. Instead of fully degenerating to unpolarized QWSs, at 9BL the TSSs show strong wavevector-dependence in inter-surface coupling and only survive near $\bar{\Gamma}$ point without opening a gap, revealing the vanishing process of spin polarization from TSSs to QWSs. To find the thickness-dependent effect, the following part will cover the FT-STS studies on 6-15BL Sb(111). In the end, the STS studies of thin films from 6BL to 11BL are shown. The energy shift of characteristic peaks can be seen in the series of spectra. Combined with first-principles calculations, the origins of these features can be elucidated, demonstrating the band evolution process of Sb(111) thin films.

## 4.2 Experimental Method

The experiments were carried out in a Unisoku UHV system equipped with a LT-STM which can perform measurements at $LN_2$ or LHe temperature. The base pressure is $7\times10^{-11}$ Torr. Si(111)-$\sqrt{3}\times\sqrt{3}$:Bi-β serves as the growth substrate, and the fabrication method has been described in Chap.2. High purity (99.999%) Bi and Sb were deposited at RT or $LN_2$ temperature. Before the deposition, both sources were degassed at appropriate temperatures for a few hours in order to remove contamination. The flux was calibrated using STM. STM images were carefully calibrated and the scanner drift was corrected. The dI/dV spectrum was acquired using a lock-in amplifier with the bias voltage modulated at a frequency of 700 Hz and the peak-to-peak amplitude of 5 mV.

## 4.3 Results and Discussion

### 4.3.1 Cracking source for Sb(111) thin film growth

Due to the steric hindrance effect[19] and lower free energy, Sb tends to be evaporated from the source as tetramer molecules ($Sb_4$)[20] and not monomer atoms ($Sb_1$). So upon arrival, $Sb_4$ molecules migrate and coalesce into three-dimensional clusters, which are normally thick, uneven and irregular[21,22]. In comparison, $Sb_1$ atoms, due to their lower surface mobility, are likely to form relatively uniform 2D islands. Since this project focuses on 2D structures to study the inter-surface coupling effect, $Sb_1$ atomic deposition is preferential. Naturally thermal dissociation can be used to produce atomic species. Hence a new growth method was developed based on high-temperature cracking, which can lead to a layer-by-layer growth mode.

Based on the previous literature using a time-of-flight mass spectrometer[19], the tetramer, dimer and monomer fractions as a function of cracking zone temperature is shown in Fig. 4.1(a), where we can find that $Sb_4$ molecules are the major product at a cracking temperature below 600 ℃. In the range of 750–1500 ℃, $Sb_1$ and $Sb_2$ species are the only products that they could detect, and higher temperature yields more $Sb_1$, which indicate that a nearly 100% output of $Sb_1$ can be obtained at a cracking temperature above 1100 ℃. Luckily these temperatures can be achieved in many MBE systems. The design of the cracking setup is schematically shown in Fig. 4.1(b).

The thermionic emission takes place from the tungsten (W) filament when the temperature is high enough. Besides, the positive voltage applied to the tantalum (Ta) foil enhances the rate of impingement of electrons emitted from the filament, leading to a higher temperature to about 1000˚C. Hence, the flux of $Sb_4$ molecules hitting the Ta foil is cracked into a flux of mostly $Sb_1$ atoms together with some $Sb_2$ molecules. Then $Sb_1$ atoms as the majority are reflected toward the substrate. Indeed, from the mass spectra taken by *in-situ* quadrupole gas analyzer, the two stable isotopes, $^{121}Sb$ and $^{123}Sb$ can be seen, while using the source without cracking they cannot be observed.

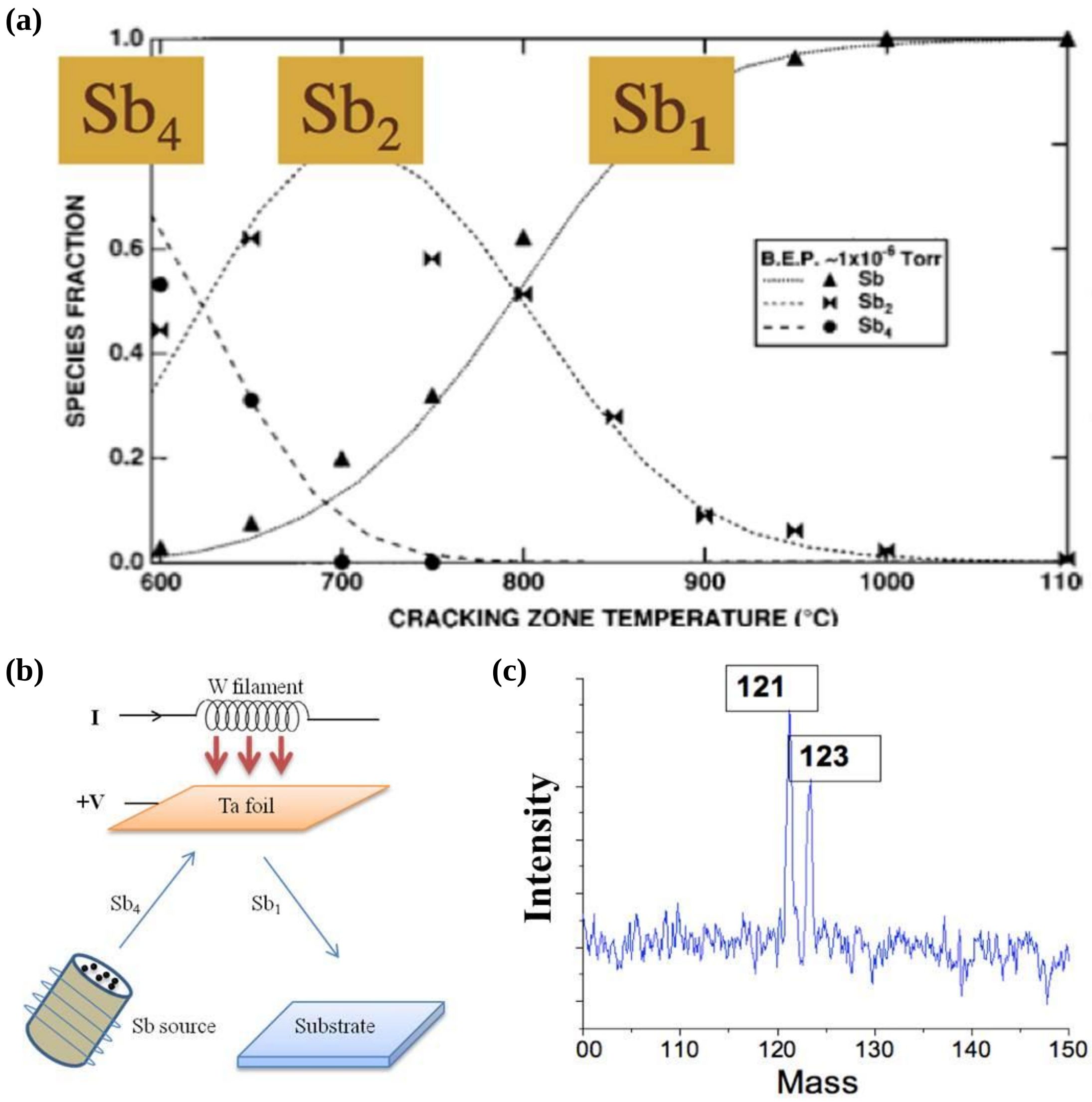

**Fig. 4.1 (a)** The relative fraction of each Sb species as a function of cracking temperature (adapted from Ref. [19], with permission from the American Institute of Physics). **(b)** A schematic diagram of the cracking set-up. The temperature of the Ta foil can be 1000˚C after 200V is applied on it due to the impingement of electron beams emitted by the W filament. After the reflection, $Sb_4$ molecules are mostly cracked into $Sb_1$ atoms. **(c)** Mass spectrum of cracked Sb species. The two stable isotopes, $^{121}$Sb and $^{123}$Sb can be seen, indicating the yield of mainly $Sb_1$ atoms after cracking is realized in this setup.

The dramatic change can be seen from the resultant Sb nanostructures shown in Fig. 4.2 below. These two images were both Sb deposited on the same substrate (Si(111)-√3×√3:Bi-β), at the same temperature (~ -150 ℃), under the same flux (0.5 BL/min) for 20 min followed by annealing at 300 ℃ for 10 min. However, the morphological difference is very obvious. The nanostructures in Fig. 4.2(a) were from the uncracked Sb source while those in Fig. 4.2(b) were from the cracked one. In the uncracked case, Sb(110) nanorods and Sb(111) islands coexist on the substrate, and the nanorods tend to grow in parallel and form bundles. Particularly, it is often observed that they grow in two perpendicular directions, as shown in the lower left part of Fig. 4.2(a), indicating the nanorods start in a simple cubic phase which forms for compressed Sb due to a large Laplace pressure[23]. The coexistence and even overlap of both (111) and (110) nanostructures complicate the uniformity of both morphology and LDOS information. Besides, the areas of Sb(111) films become rather limited in this case, which makes it difficult to perform FT-STS measurements. In contrast, large areas of uniform Sb(111) films can form in the cracked case, making the surface suitable for accurate FT-STS studies. Additionally, thin (111) islands with thickness less than 10BL are rare using the uncracked source even at lower deposition because of the $Sb_4$-induced 3D island growth mode, which is inappropriate for our inter-surface coupling studies. In this sense, the fabricated Sb (111) films using the cracked source have great advantages in both the area and the thickness than those using uncracked source.

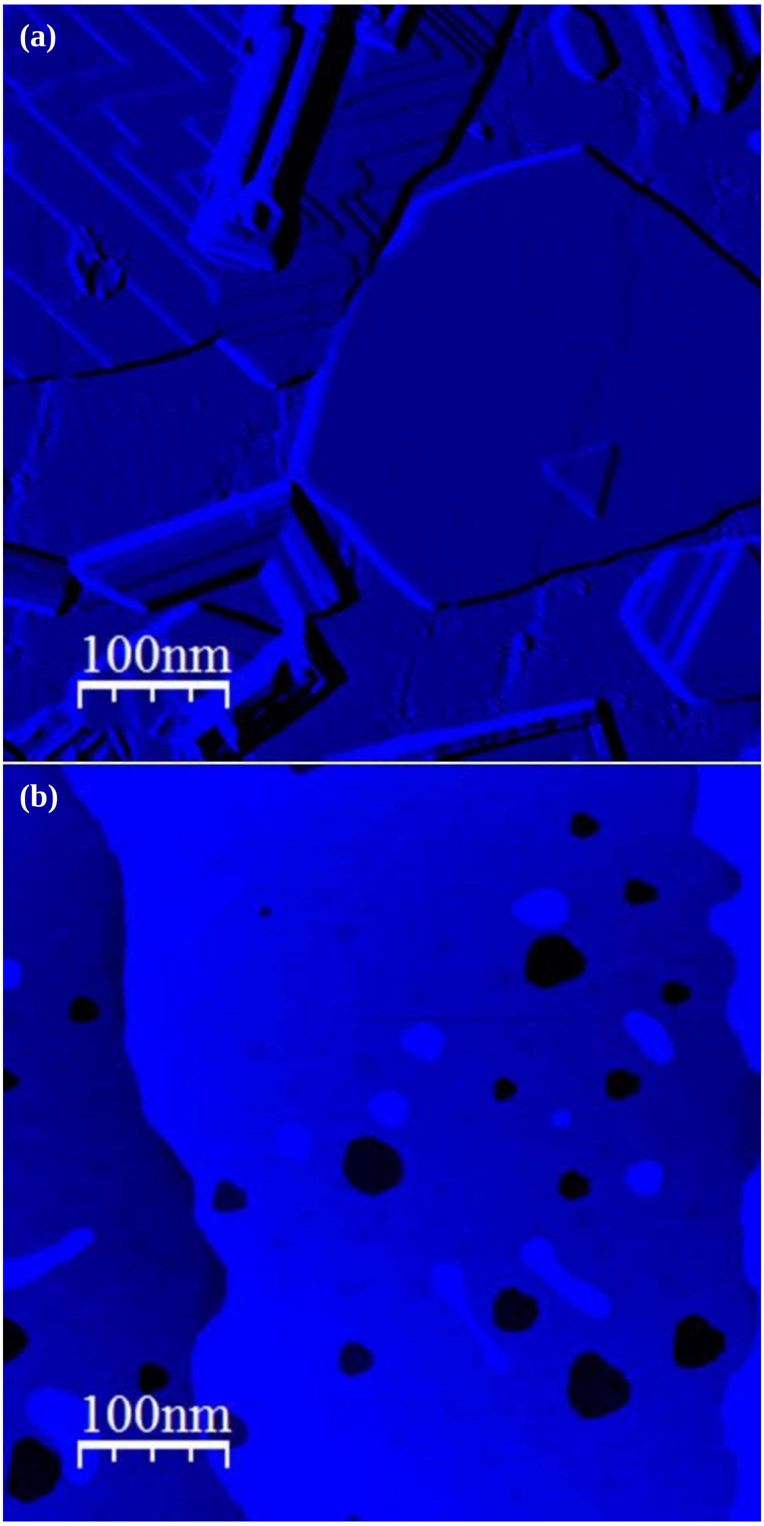

**Fig. 4.2** Sb(111) on Si(111)-√3×√3:Bi-β using **(a)** an uncracked Sb source and **(b)** a cracked source. The morphology shows dramatic changes between these two methods. In the first case, higher (111) islands and (110) nanorods dominate because of the $Sb_4$ molecules, while in the second case, flat and uniform (111) thin films dominate.

The complete growth process using the cracking source will be introduced next. 30-min deposition with a flux of 0.5 BL/min is used here as an example. The substrate Si(111)-√3×√3:Bi-β was maintained at about -150 ℃. At the beginning, $Sb_1$ atoms tend to form (110) nanorods, as shown in Fig. 4.3(a). Here the deposited atoms have little thermal energy (~ 10 meV) to overcome the diffusion barrier and form a large compact shape structure. In fact, they nucleate broadly on the substrate, leading to numerous (110) straight and branched nanorods with thickness between 3 nm and 15 nm. Besides, due to the weak interface bonding there are no obvious areas of flat terraces. Then after annealed at 300 ℃ for 10 minutes, the same sample has totally different morphology. Most of the Sb(110) nanorods disappeared and large areas of uniform Sb(111) films appear, which can be determined by both the inset atomic resolution image in Fig. 4.3(b) and the triangular shape of the islands and defects. The phase transition from Sb(110) to Sb(111) is triggered by appropriate annealing here.

image on the surface.

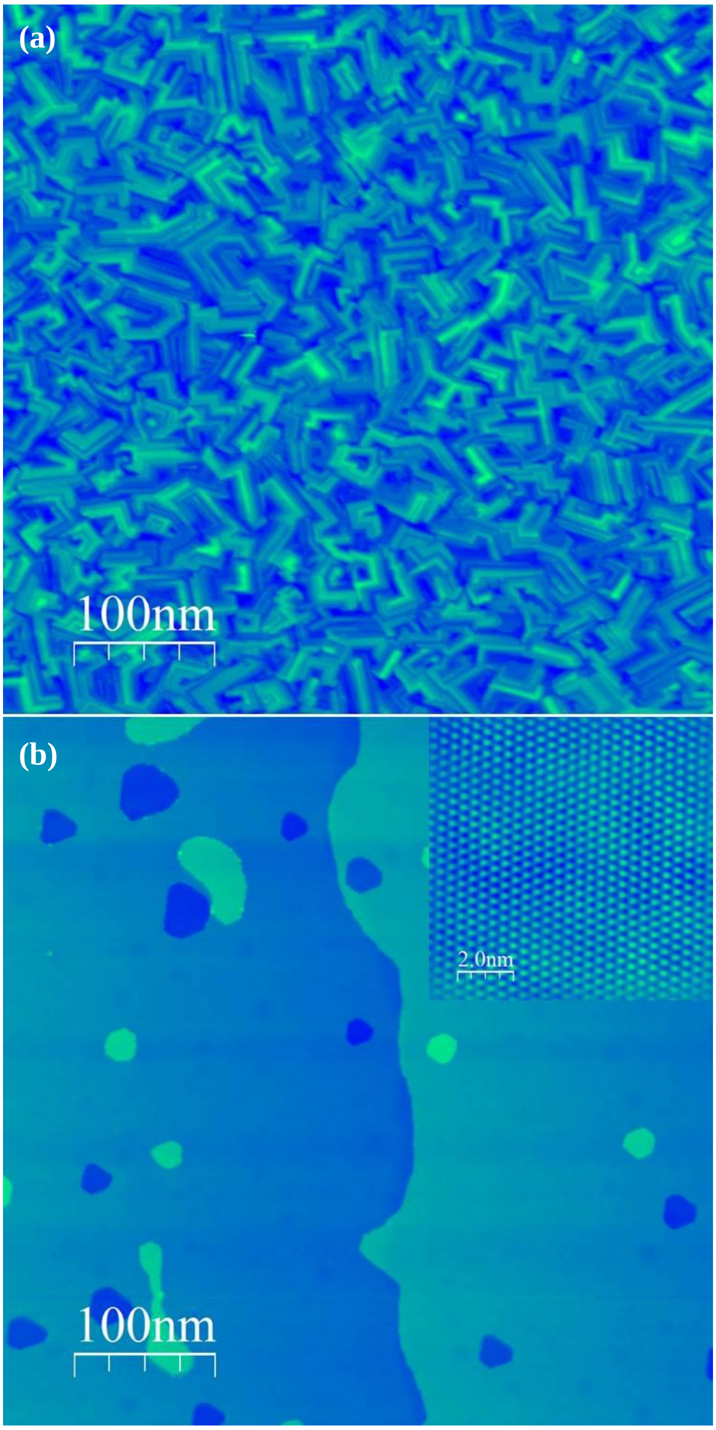

**Fig. 4.3 (a)** Straight and branched Sb(110) nanorods obtained at -150 ℃. **(b)** Sb(111) thin films after annealing the sample in (a) at 300 ℃. The inset is the atomic resolution image on the surface.

It needs pointing out that on various substrates[24-26], the phase transition from (110) to (111) is very common for Bi, which is also a group V semimetal. However, for uncracked Sb, the coexistence of two phases is easier to appear. Considering the deposition flux for Bi is mainly $Bi_1$ atoms and $Bi_2$ molecules, using cracked Sb the phase transition shows much similarity to the Bi case, unambiguously indicating the composition changes of the source. From the description above, we know that the cracked Sb source, which can generate $Sb_1$ atoms, is suitable for formation of uniform Sb(111) thin films because $Sb_1$ atoms have the lower surface mobility to obtain 2D structures. In the next section, FT-STS studies on thin films prepared by this method will be introduced.

### 4.3.2 FT-STS studies on 9BL Sb(111) thin films

In this project 9BL (~3.88nm) films as the example were chosen to study the inter-surface coupling effect. Actually, from the first-principles calculations, at this thickness, the coupling of SSs at $\bar{\Gamma}$ is not strong enough to open a gap yet, as shown in Fig. 4.4(a), indicating the robustness of TSSs. The corresponding CEC at $E_F$ is shown in Fig. 4.4(b). Since the band structure around $\bar{\Gamma}$ does not change much compared with that of the bulk, the CEC here in the central part seems quite similar with the one in Fig. 3.12(a), where the Fermi surface is composed of a central electron pocket around the $\bar{\Gamma}$ point, surrounded by 6 hole pockets along $\bar{\Gamma}-\bar{M}$. It is also worth noting that in Fig.

4.4(b) there are also six electron pockets far away from $\bar{\Gamma}$ (~0.7 Å$^{-1}$). Because the scattering events involving these bands correspond to much larger $\boldsymbol{q}$ values, which can hardly be observed in the FT-STS mapping, the influence of these outer pockets is negligible when we analyze the QPI patterns.

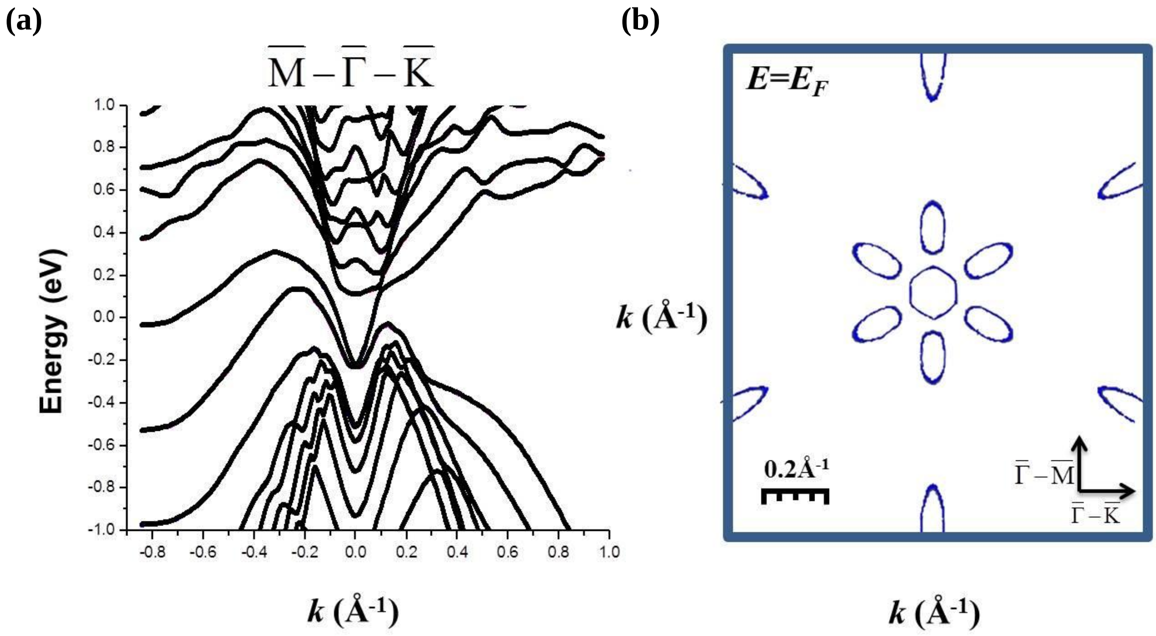

**Fig. 4.4 (a)** The calculated band structure of 9BL Sb(111) films. **(b)** CEC at $E_F$ based on the band structure in (a).

Shown in Fig. 4.5 is the FT-STS mapping on 9BL Sb(111) at different energies. All these images (with bias applied on the sample) are obtained at the same area (50 nm × 50 nm). Compared with the 30BL case at the same energy in Fig. 3.11, we can see dramatic changes in the scattering intensity distribution. Firstly, different from dominating intensity along the $\bar{\Gamma}-\bar{M}$ directions in the thick case, here comparable intensity along $\bar{\Gamma}-\bar{\mathrm{K}}$ can also be seen. Secondly, instead of discrete scattering vectors **q** at a specific energy in 30BL Sb, continuous intensity with clear cutoff vectors along $\bar{\Gamma}-\bar{\mathrm{M}}$ and $\bar{\Gamma}-\bar{\mathrm{K}}$ are observable on 9BL Sb, indicating new scattering channels have emerged in this case. These extraordinary features cannot be solely determined by the band structure, since around $\bar{\Gamma}$ it does not change much from 30BL down to 9BL. So the spin related factors must be taken into account.

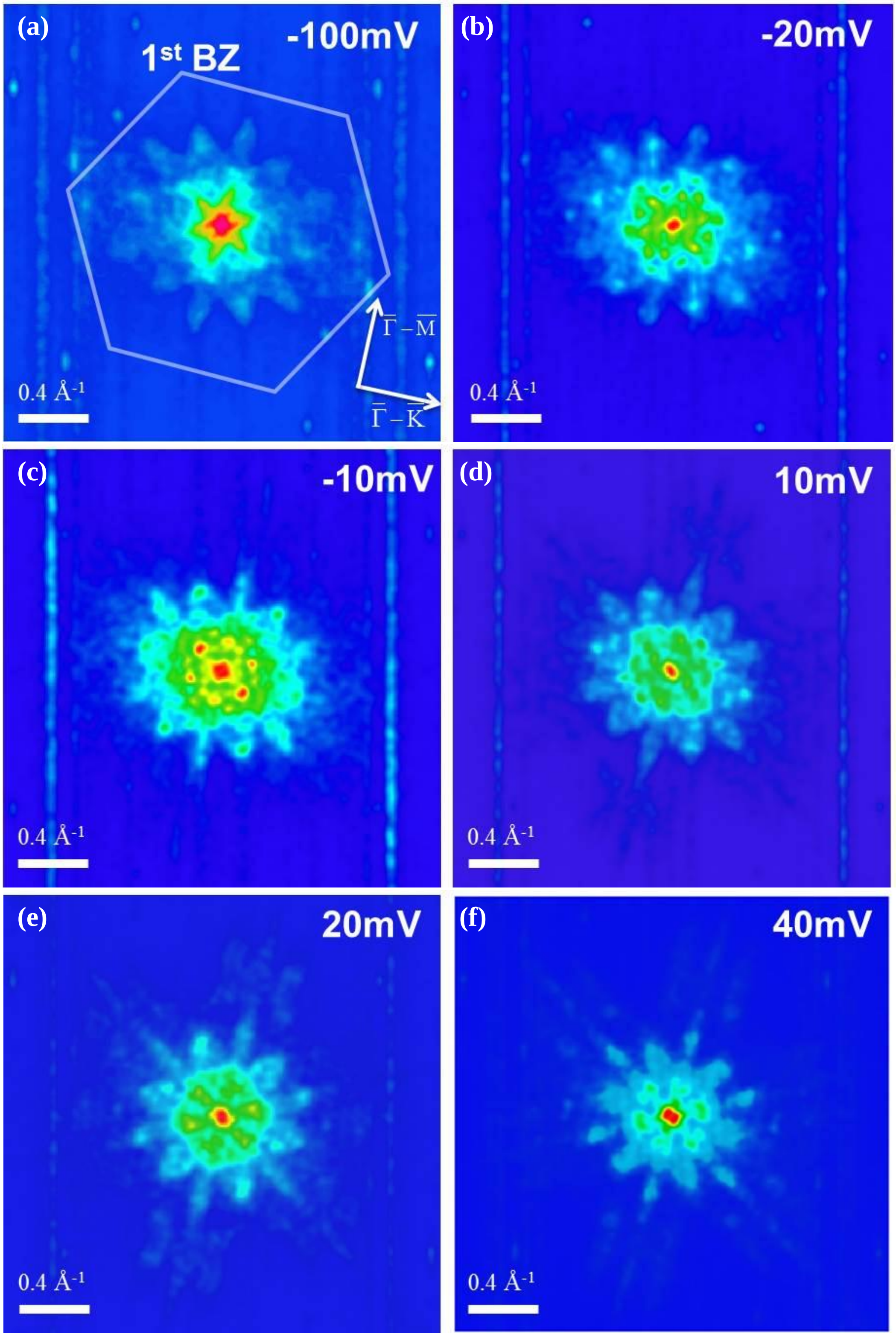

**Fig. 4.5** Bias-dependent FT-STS measurements on 9BL Sb (111) near $E_F$. All patterns consist of continuous scattering vectors along both $\overline{\Gamma}-\overline{M}$ and $\overline{\Gamma}-\overline{K}$. The direction is marked in (a). The FBZ is marked as the white hexagon.

Now we discuss the origins of these **q** vectors in the mapping. The FT-STS measurement at 20 mV is taken as an example as shown in Fig. 4.6(a). Specifically, the two cutoff vectors marked as $\mathbf{q}_\mathbf{C}$ and $\mathbf{q}_\mathbf{D}$ (both shown as black dashed lines) are 0.63 Å$^{-1}$ and 0.54 Å$^{-1}$, which are along $\overline{\Gamma}-\overline{\mathrm{M}}$ and $\overline{\Gamma}-\overline{\mathrm{K}}$, respectively. For comparison, the calculated CEC is needed. From Fig. 4.5 we know the largest observable scattering vectors are less than 0.6 Å$^{-1}$, so the central part of CEC around $\overline{\Gamma}$ associated with the spin texture is selected for simplicity as shown in Fig. 4.6(b), while the outer electron pockets in Fig. 4.4(b) are dismissed. Based on the scale near $E_F$ in the calculated CEC, the possible scattering channels can be determined in Fig. 4.6(b). It is worth noting that spin directions (grey arrows in Fig. 4.6(b)) of the upper surface are labeled artificially in order to address that the scattering, especially $\mathbf{q}_\mathbf{C}$, seems to violate the spin conservation if we only consider the spin texture of the upper surface. In fact the real spin distribution on the CEC is complicated considering the inter-surface coupling effect.

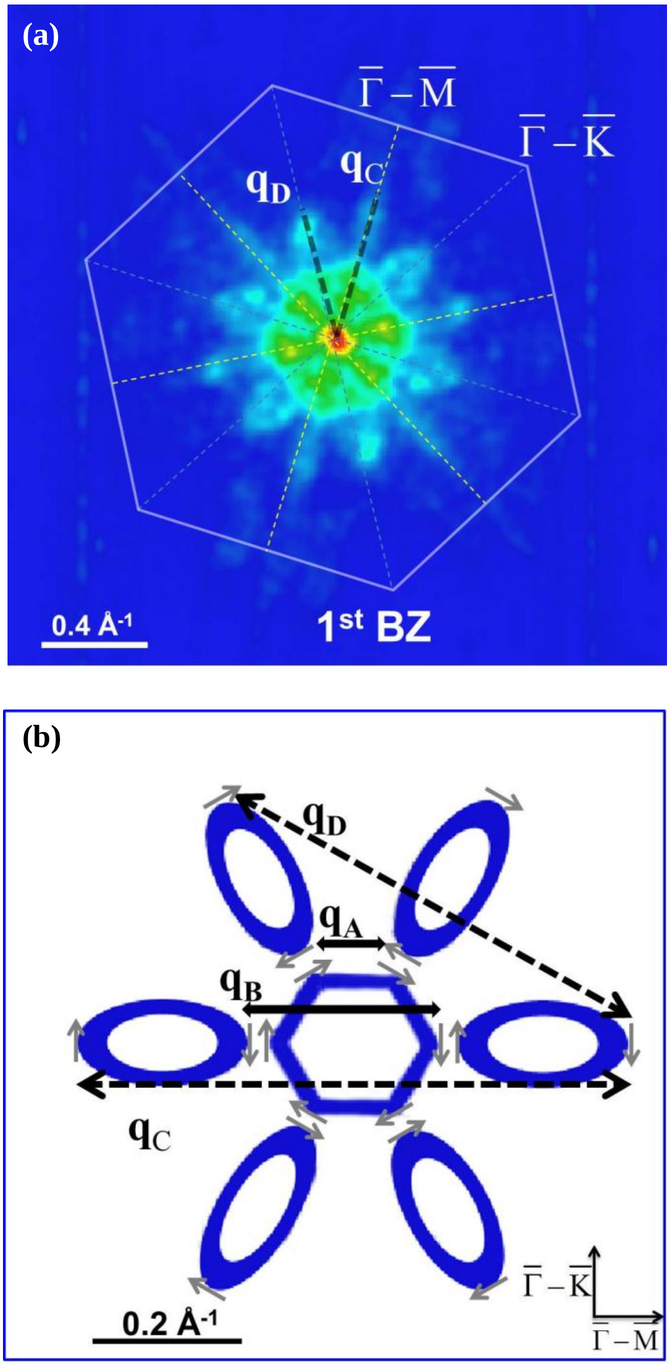

**Fig. 4.6 (a)** A representative FT-STS mapping at 20mV within FBZ. Two cutoff vectors marked as $\mathbf{q_C}$ and $\mathbf{q_D}$ are both shown as black dashed lines. **(b)** $\mathbf{q_C}$ and $\mathbf{q_D}$ in the calculated CEC at Fermi energy. The grey arrows illustrate the spin directions on the upper surface. Obeying spin conservation, $\mathbf{q_A}$ and $\mathbf{q_B}$ (solid black lines) still exist and correspond to the central green zone with high intensities in (a).

One striking aspect is that the unique length ratio $2/\sqrt{3}$ between $\mathbf{q_C}$ and $\mathbf{q_D}$ cutoff vectors under any bias in the observed range. As mentioned above, in Fig. 4.6(a) $\mathbf{q_C}$ equals to 0.63Å$^{-1}$ while $\mathbf{q_D}$ = 0.54Å$^{-1}$. Actually it can be derived from Fig. 4.6(b), where we can find out that the former ($\mathbf{q_C}$) should be associated with scatterings between the outermost edges of the "opposite" hole pockets along $\bar{\Gamma}-\bar{\mathrm{M}}$, and the latter ($\mathbf{q_D}$) can be assigned to those between the "next-nearest-neighbor" hole pockets along $\bar{\Gamma}-\bar{\mathrm{K}}$. Therefore, the specific ratio is ultimately determined by the geometry of the Sb band structure as shown in Fig. 4.6(b). Besides, it is also striking because these scatterings, $\mathbf{q_C}$ and $\mathbf{q_D}$, are forbidden or very weak in 30BL Sb. However, here in the 9BL case they do exist as if breaking the spin conservation. In fact, different from the thick case in which the two surfaces are well separated from each other, here the thin film approaches the 2D limit, and thus one SS is no long confined to one surface. So now, it is possible for an electron in state ***k*** on one surface to scatter into a state ***k'*** with the same spin on the opposite surface. SSs from the two opposite surfaces are doubly degenerate, and the strong inter-surface coupling diminishes the spin polarization of SSs. This opens up new scattering channels along $\bar{\Gamma}-\bar{\mathrm{K}}$ without violating the spin conservation. Therefore, quite different from the 30BL Sb where the patterns mainly originate from the so called "intra-surface scattering", here the unusual patterns with comparable intensities both along $\bar{\Gamma}-\bar{\mathrm{M}}$ and $\bar{\Gamma}-\bar{\mathrm{K}}$ originate from the "inter-surface scattering".

Moreover, it is extraordinary that the discrete vectors extracted from FT-STS of 30BL films are transformed into continuous ones here, meaning that any scattering is allowed as long as it occurs within the range confined by the cutoff vectors $\mathbf{q_C}$ and $\mathbf{q_D}$ in Fig. 4.6(a). This is based on the same reason of higher scattering probabilities due to lifting of the spin constraint. Scattering channels are no longer bound to occur merely between the states at the edges of the hole pockets with definite spin directions but also between any two states on the pockets, thus inducing continuous QPI patterns instead of discrete ones.

It is also noticeable that the inner patterns (shown as the central green zone in Fig. 4.6(a)) have stronger intensities than $\mathbf{q_C}$ and $\mathbf{q_D}$, and they correspond to $\mathbf{q_A}$ and $\mathbf{q_B}$ (solid black lines in Fig. 4.6(b)). Interestingly, comparing the QPI patterns taken on 30BL Sb in Fig. 3.11(p) with the core part here, one can find that they overlap very well, demonstrating that intra-surface scatterings still contribute a lot. This two-part pattern unambiguously visualizes the coexistence of intra- and inter-surface scattering events.

The QPI patterns of the thin Sb(111) film can be explained in another perspective. For a Sb(111) thick film, there is one Dirac cone of TSSs on each surface, forming a Kramers pair. With inversion symmetry, a pair of SSs of a particular $\boldsymbol{k}$ are degenerate in energy but with opposite spin. In a thin Sb(111) film, this pair of SSs can mix together, yielding a state that is degenerate in spin. However, the degree of mixing is still unknown, raising a question whether this pair of SSs is fully or partially degenerate in spin. It is significant because if fully degenerate the SSs would lose their topological properties and simply degrade to be QWSs due to the QCE. However, the two-part pattern strongly indicates that on the 9BL Sb(111) surface both TSSs and QWSs coexist, demonstrating a partial spin degeneracy.

Therefore, efforts are needed for generating the spin separation of SSs in **k** space to interpret the dynamic process of evolution from TSSs to QWSs. Following the procedure of calculating the spin separation of SSs described by Bian *et al.*[18], we select one specific surface band (marked as blue lines in Fig. 4.7(a)) along $\bar{\Gamma}-\bar{\mathrm{M}}$, and compute the spin separation as a function of the momentum on that band [Fig. 4.7(b)], where normalized values, ±1, represent the fully spin-polarized TSSs. Interestingly, a strong ***k***-dependent transition from fully spin-polarized TSSs to fully unpolarized QWSs can be clearly found out, showing that the spin degeneracy increases as ***k*** moves away from $\bar{\Gamma}$ and towards $\bar{\mathrm{M}}$. Total spin degeneracy occurs at $\mathbf{k}$ =0.34 Å$^{-1}$, which is closer to $\bar{\Gamma}$ point compared with the situation of 20 BL Sb(111)[18]. Because the thinner the film, the stronger the inter-surface coupling effect, more SSs are expected to show small spin separation and even spin degeneracy. Thus the signature of this trend is the spin degeneracy point approaching towards the $\bar{\Gamma}$ point. This thickness-dependent trend will be verified next in Section 4.3.3.

In addition, the band structure along $\bar{\Gamma}-\bar{\mathrm{M}}$ is plotted in Fig. 4.7(a-b), and the three points marked as A, B and C correspond to the band positions cut by the Fermi level. Specially, point B is the initial or final momentum involved in the scattering vector $\mathbf{q_B}$ in Fig. 4.6(b), near which topological properties are still solid. Based on Fig. 4.7(b), it corresponds to ±0.9 in the spin separation, demonstrating that the 10% spin degeneracy is not enough to trigger the transition from TSSs to QWSs.

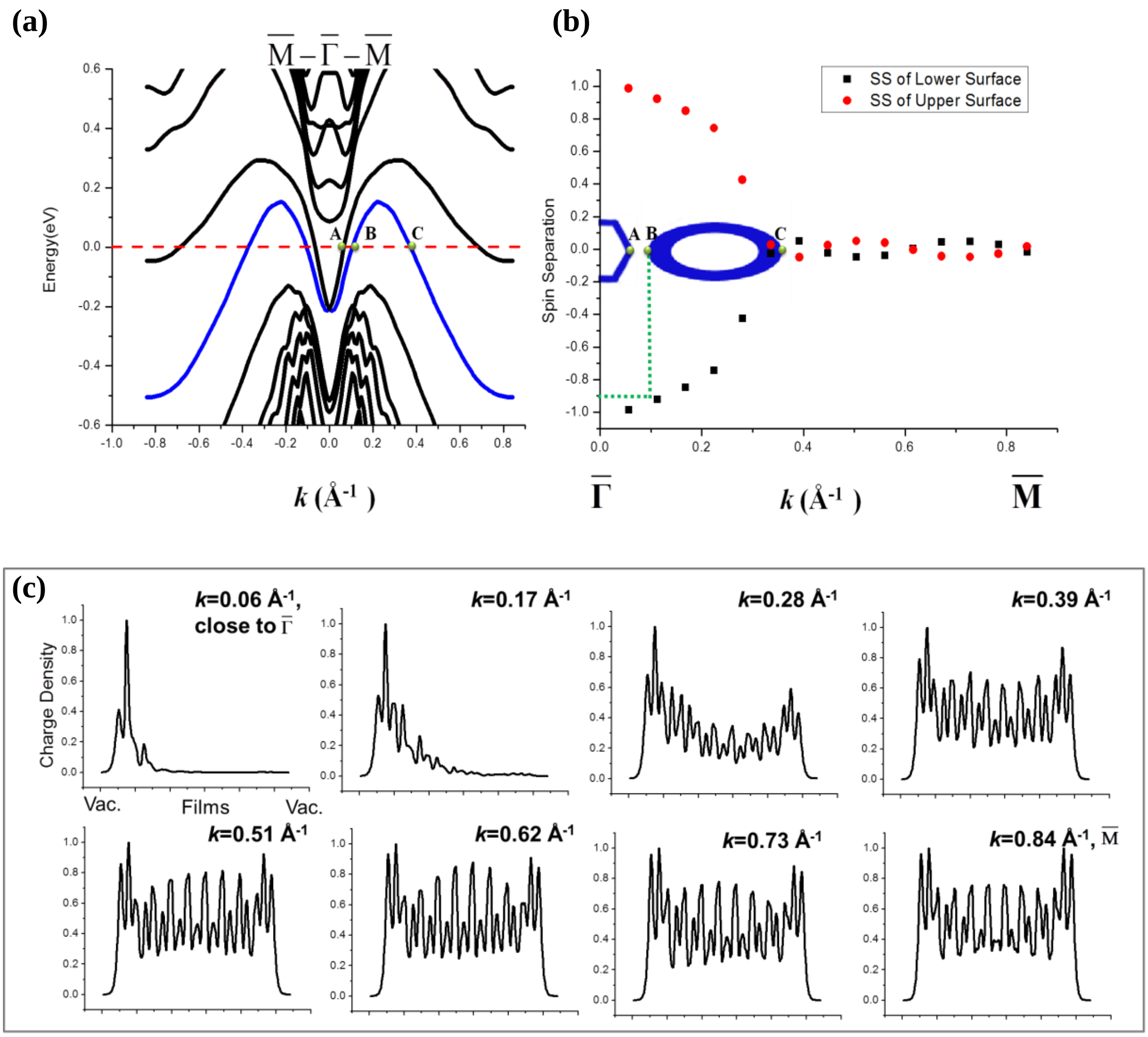

**Fig. 4.7 (a)** Calculated band structure of 9BL Sb(111) along $\overline{\Gamma}-\overline{\mathrm{M}}$. The blue lines represent the surface band chosen for computing the spin separation. **(b)** Spin separation as a function of the wavevector, indicating the strong ***k***-dependent coupling of upper and lower states. A, B and C points are labeled for comparison between the band structure and CEC along $\overline{\Gamma}-\overline{\mathrm{M}}$. **(c)** The real-space distribution of SS from near $\overline{\Gamma}$ to $\overline{\mathrm{M}}$ obtained from DFT computation, showing that a well-defined localization of SS around $\overline{\Gamma}$ but large penetration depth for states from 0.34Å$^{-1}$ to $\overline{\mathrm{M}}$, which is strong evidence to treat that part of states as QWSs.

This can also be explained with the distribution of SSs in real space as shown in Fig. 4.7(c). 8 equal-spacing points along the blue SS band ranging from near $\bar{\Gamma}$ to $\bar{\mathrm{M}}$ in Fig. 4.7(a) are chosen to calculate the spatial location of SSs in the 9BL film. It is obvious that around $\bar{\Gamma}$ the SSs are well localized near the surface, indicating that the coupling is difficult to realize in that part due to the spatial separation. In contrast, when approaching $\bar{\mathrm{M}}$ the distribution of SSs becomes more and more spread over the whole thickness, meaning the inter-surface coupling is stronger due to the spatial overlap.

Additionally, based on the CEC and the spin texture near the Fermi energy, we can simulate the scattering pattern as shown in Fig. 4.8(b), which is in good agreement with our experimental demonstration in Fig. 4.8(a). Firstly, the characteristic feature of comparable intensities both along $\bar{\Gamma}-\bar{\mathrm{M}}$ and $\bar{\Gamma}-\bar{\mathrm{K}}$ can be seen. The red and green arrows are used to label the "head" and "tail" positions, which corresponds to $\mathbf{q}_\mathbf{B}$ [Fig. 4.6(b)] due to intra-surface coupling and $\mathbf{q}_\mathbf{C}$ [Fig. 4.6(b)] due to inter-surface coupling, respectively. Secondly, it can be seen that the core part of the simulated pattern has brighter colors corresponding to the "head", demonstrating six stronger intensities along $\bar{\Gamma}-\bar{\mathrm{M}}$, which is consistent with our observation that the intra-surface coupling is still important.

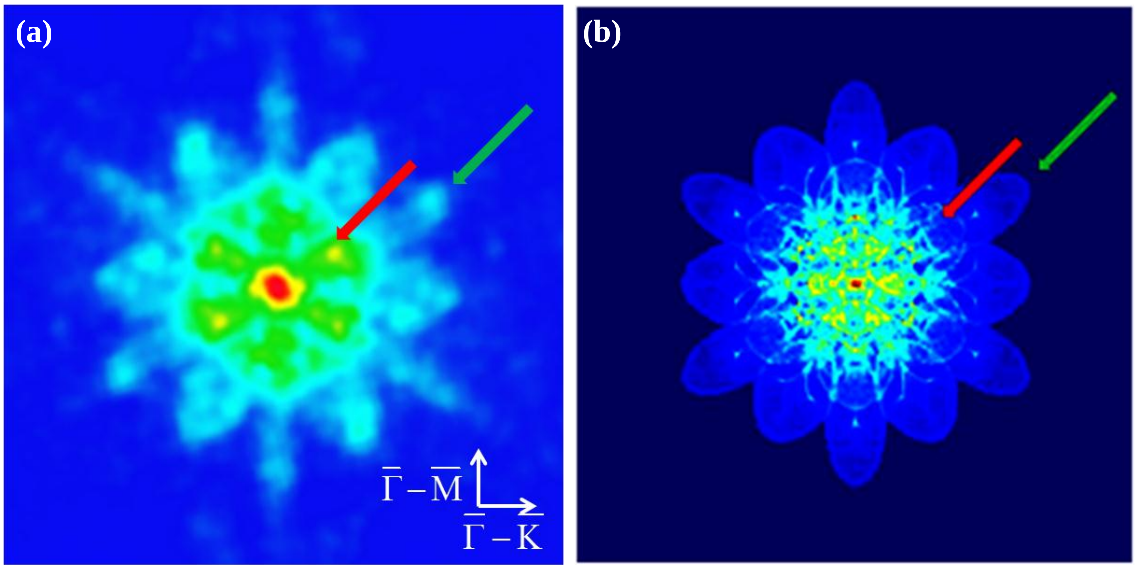

**Fig. 4.8 (a)** FT-STS mapping at 20mV and **(b)** the corresponding simulated pattern based on first-principles calculations. The red and green arrows mark the position due to TSSs and QWSs, respectively.

The inter-surface coupling of TSSs in $Bi_2Se_3$ thin films have been studied both theoretically and experimentally[4,7], where the most remarkable effect is the opening of a bandgap at $\bar{\Gamma}$. Compared to Sb(111), TSSs on $Bi_2Se_3$(111) form a fairly ideal Dirac cone with a rather weak warping in the bulk bandgap region[27,28]. They can be considered as true SSs. In contrast, Sb(111) has a highly warped Dirac cone. The SSs not far from the $\bar{\Gamma}$ point have long penetration depth into the interior, and they almost behave as surface resonance states. At 9BL thickness, the inter-surface coupling of these states makes them located more near the film centre than at the surfaces. As a result, the spin splitting due to the Rashba effect[29] is greatly diminished.

One of our first thoughts to study Sb(111) ultrathin films is that the negative bandgap in bulk can be tuned to a positive one due to QCE, and hence Sb becomes a real TI if TSSs are still there. However, after the observation and explanation of FT-STS patterns in 9BL Sb films, we know that in Sb thin films, part of SSs degenerate to QWSs and lose their topological properties. In this sense, Sb ultrathin films cannot be defined as a TI. But still, Sb is a unique system to get insight into the transition from TSSs to QWSs when the thickness decreases towards 2D limit. Although not an ideal TI, it indeed allows us to investigate the extraordinary scatterings via the same spin direction, while in other TIs (e.g. $Bi_2Se_3$) possessing a fairly ideal Dirac cone it is impossible to get similar features exclusively between SSs. The “distorted” Dirac cones of Sb thin films offer us an interesting quasi-2D system to help interpret the detailed progress of coherent coupling and hybridization of TSSs. Nevertheless of particular interest is the tunability of spin-related scattering channels by means of changing thickness, which can be effectively manipulated to influence the transport properties and to obtain desired electronic and spintronic properties of the interesting films from the application point of view.

### 4.3.3 Thickness-dependent FT-STS studies on Sb(111) thin films

From the discussions of scatterings in 9BL Sb(111) above, we know the ***k***-dependent diminishing process for the spin polarization from $\overline{\Gamma}$ to $\overline{\mathrm{M}}$ gradually. Besides, combined with data on 30BL in Chap. 3, it can be envisaged that this diminishing process is also thickness-dependent, i.e. SSs of thinner films would give rise to larger QWSs contributions due to stronger inter-surface coupling effect. Therefore, on several film thicknesses, this phenomenon will be examined by evaluating the ratio between QPI intensities due to QWSs and TSSs.

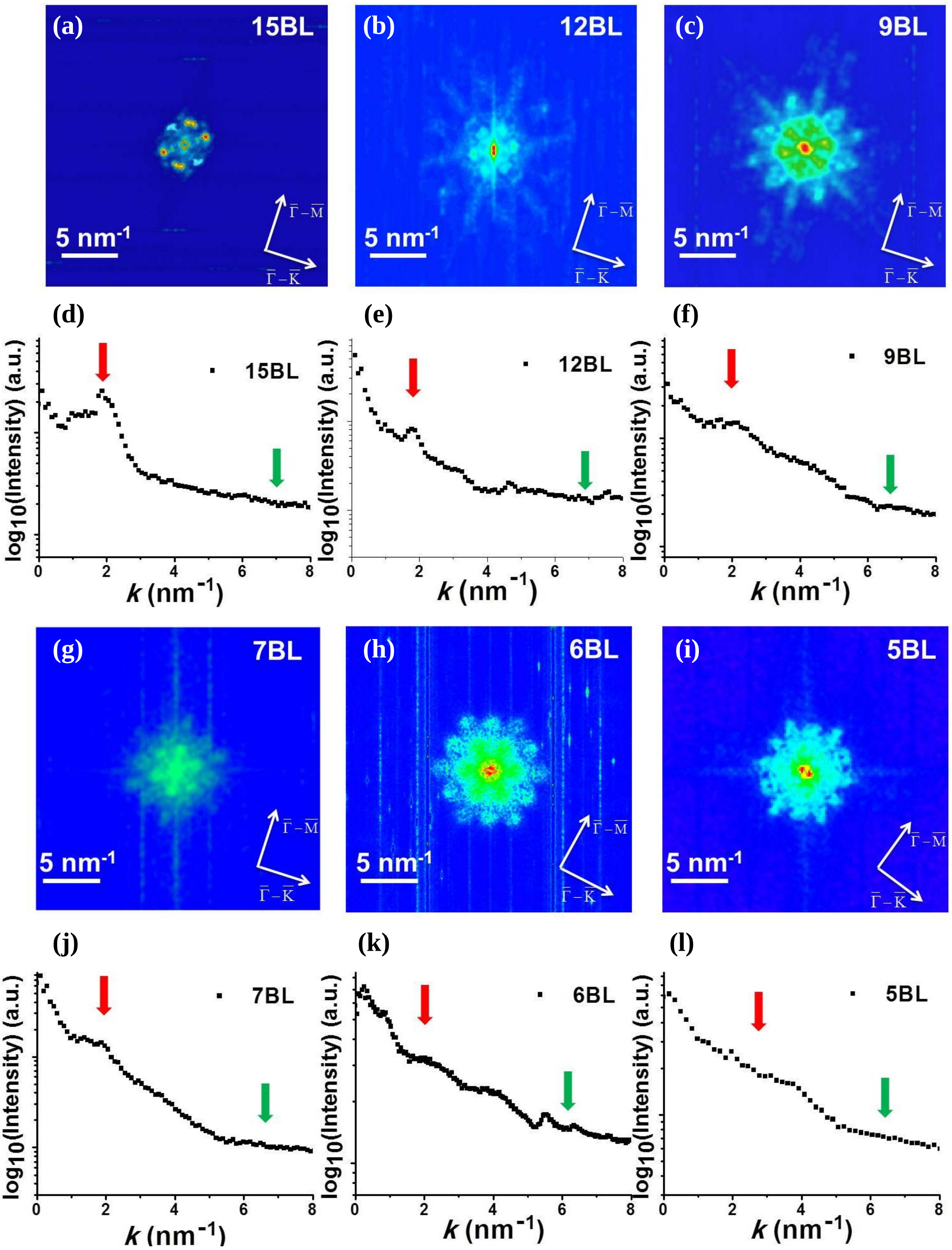

**Fig. 4.9 (a-c)** and **(g-i)** show the FT-STS patterns taken on 15, 12, 9, 7, 6, 5BL Sb(111), respectively. **(d-f)** and **(j-l)** show the corresponding average intensities (logarithmic scale) along $\bar{\Gamma}-\bar{\mathrm{M}}$. The red and green arrows mark the position of inner “heads” due to intra-surface coupling and outer “tails” due to inter-surface coupling.

The thickness-dependent FT-STS patterns under the same bias (+20 mV) as well as the distribution of corresponding average intensities along $\bar{\Gamma}-\bar{M}$ are shown in Fig. 4.9. Based on (a-c) and (g-i), it can be easily figured out that from 15BL down to 5BL, the intensities of “heads” are reduced as the film becomes thinner, demonstrating a weaker intra-surface coupling effect. In contrast, the “tails” are absent on 15BL, but they become more observable as the film becomes thinner, indicating a stronger inter-surface coupling effect. This phenomenon is qualitatively consistent with the previous conclusion based on the spatial extent of SSs wavefunctions.

We now analyze the corresponding intensity data in (d-f) and (j-l) for the “heads” and “tails” in FT-STS patterns. We define their intensities as $I_H$ and $I_T$, respectively, and obtain the ratio $I_T/I_H$ as a function of the number of Sb BLs in Table. 4.1.

**Table 4.1** The ratio $I_T/I_H$ vs. the film thickness. The ratio increases monotonically as the film becomes thinner.

| **No. of BL** | **15** | **12** | **9** | **7** | **6** | **5** |
|---|---|---|---|---|---|---|
| **$I_T/I_H$ (%)** | 7 | 14 | 16 | 18 | 44 | 47 |

Plot the the ratio as a function of film thickness in Fig. 4.10 and we can see the relationship more clearly. Since “heads” come from intra-surface coupling while “tails” come from inter-surface coupling, this ratio $I_T/I_H$ is an effective parameter to quantitatively measure the strength comparison between two competing coupling channels. More fundamentally speaking, the coupling effects are ultimately determined by the real-space distributions of wavefunctions in the involved states confined by the band structure and the associated spin texture. In this sense, this monotonic trend unambiguously confirms our explanation on the evolutionary process of diminishing spin polarization, not only from $\overline{\Gamma}$ to $\overline{M}$, but also from thick to thin films.

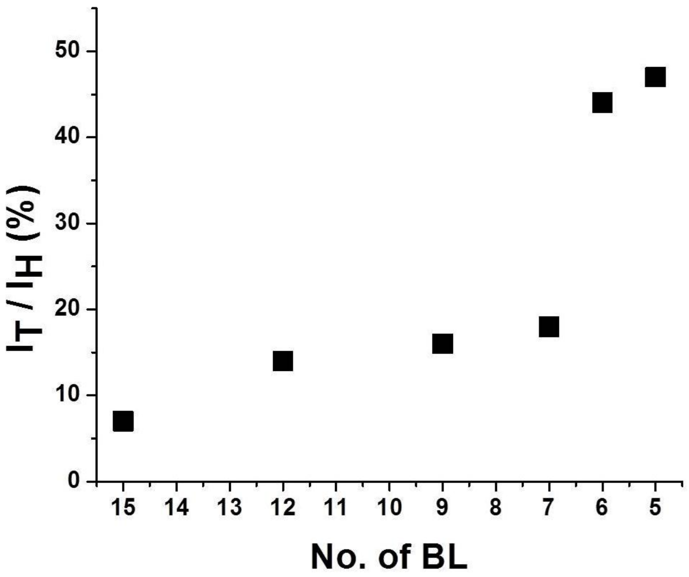

**Fig. 4.10** The ratio $I_T/I_H$ as a function of the film thckness derived from Table 4.1.

Besides the monotonic correlation, it is noticable that there exists a significant “jump” for the ratio from 7BL to 6BL, indicating the thickness around this range undergoes a dramatic transition[30,31] for the ovelap of wavefunctions of two opposite SSs. This specific issue needs further investigations with first-principles calculations.

### 4.3.4 STS studies on 6-11BL Sb(111) thin films

Till now we know the physical properties of SSs are determined by not only the band structure, but also the spin texture associated with it. In the previous section, efforts were made to reveal the underlying spin information by means of FT-STS. However, this has disadvantages on illustrating details of the band structure, because FT-STS measurements focus on the spatial distribution of scatterings and lacks the particulars of LDOS. Specifically, we also need to know the details of the band, such as the shape, position of characteristic points like the Dirac point. Actually, as shown before, STS data can give us the energy distribution of LDOS more precisely. Therefore, next we will perform STS measurements on ultrathin Sb(111) films ranging from 6BL to 11BL, to investigate the subtle evolution of band structures in these films.

Fig. 4.11 is published by Gomes et al.[32]. They gave the STS profile, which shows features that correspond to those in the ARPES within the same energy window, both from bulk Sb samples. This good agreement between these two methods indicates that we can also reveal the corresponding correlation between STS spectra and the band structure obtained from first-principles calculations. Here for comparison on different films, we define three characteristic points: the energy of the Dirac point ($E_D$), the inflection point along $\overline{\Gamma}-\overline{K}$ direction ($I_K$) and that along $\overline{\Gamma}-\overline{M}$ direction ($I_M$), which can help us determine changes of band structures as the thickness changes.

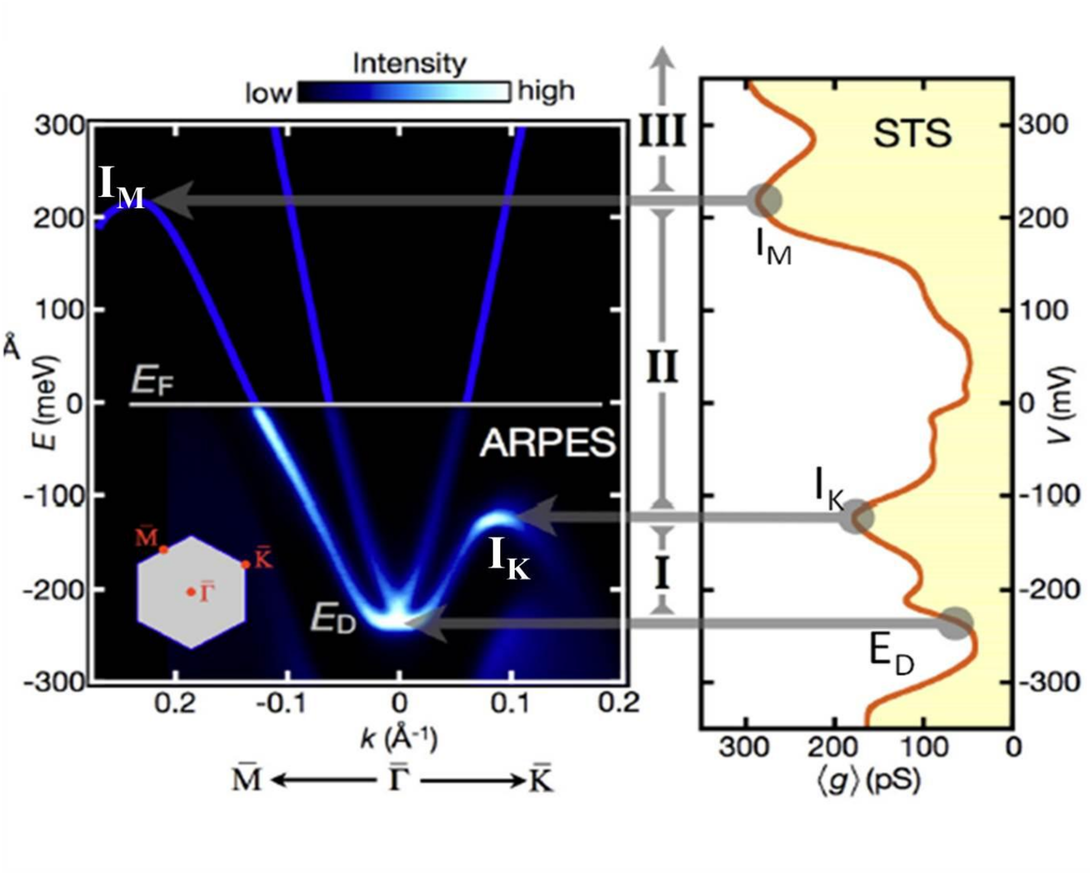

**Fig. 4.11** ARPES and STS results show features within the same energy window on bulk Sb[32]. (Images are reprinted from Ref. [32].)

It is worth noting that since $E_F$ is not aligned in different films, the absolute values of $E_D$, $I_K$ and $I_M$ are not effective references to reveal the evolution process. Hence we shall use the energy differences instead, ($I_K$ - $E_D$) and ($I_M$ - $E_D$), to examine changes in thickness-dependent band structures. Fig. 4.12 shows the calculated band structure in (a) and the STS spectra in (b), where $E_D$, $I_K$ and $I_M$ are marked as reference.

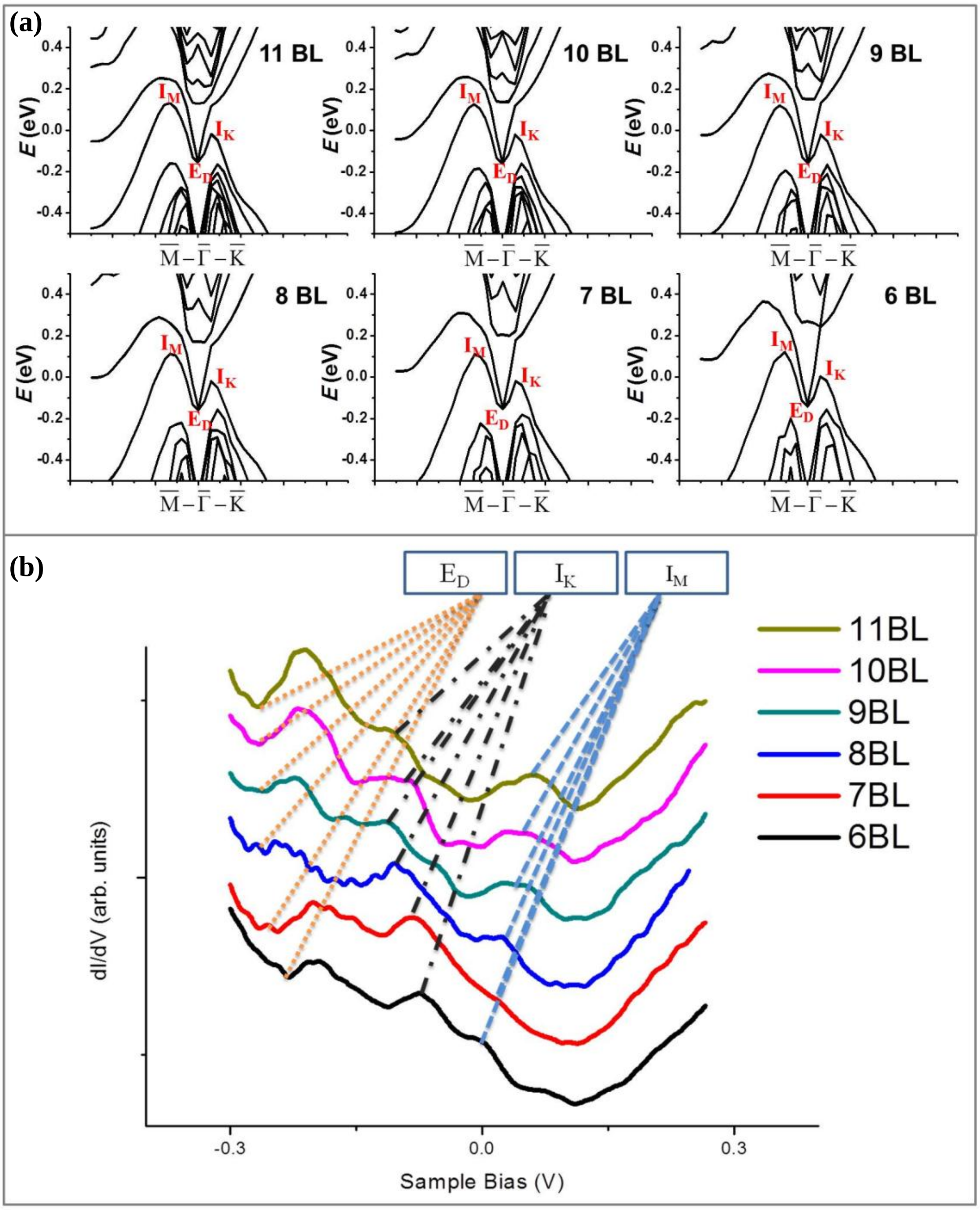

**Fig. 4.12 (a)** Calculated band structure of Sb(111) thin films from 11 BL to 6 BL. **(b)** STS measurements performed on Sb(111) films of different thickness with marked $E_D$, $I_K$ and $I_M$ points.

Now the corresponding energies of $E_D$, $I_K$ and $I_M$ are extracted. Referring to Table 4.2 below, the correlation between the thickness and the energy differences can be plotted in Fig. 4.13. Here the error bar scale is the thermal energy at $LN_2$ temperature (77 K), which is about 6.7 meV. Our STS data show that the peak positions shift with the thickness of Sb(111) thin films. More specifically, the energy difference between $E_D$ and $I_M$ shows an obvious decreasing trend with the decrease in film thickness. This can be explained by the QCE, in which the energy gap is opened further when the dimensions of the nanostructure are reduced. This causes surface bands connected to the bulk valence band (BVB) along $\overline{\Gamma}-\overline{\mathrm{M}}$ to move downwards, which lowers the corresponding energy level of $I_M$. Interestingly, for the energy difference between $E_D$ and $I_K$, no such trend can be observed, and the increase in film thickness has no discernible effect on the energy difference.

Besides, based on the energy difference obtained by experiments (solid lines) and calculations (dot lines), we find the consistent results for this evolutionary process.

**Table 4.2** The trends in energy differences with the number of BLs.

| **No. of BL** | **$E_D$ (mV)** | **$I_K$ (mV)** | $I_K$ - $E_D$ (mV) | **$I_M$(mV)** | $I_M$ - $E_D$ (mV) |
|---|---|---|---|---|---|
| **6** | -229 | -76 | **153** | 3 | **232** |
| **7** | -235 | -84 | **151** | 37 | **272** |
| **8** | -259 | -104 | **155** | 22 | **281** |
| **9** | -261 | -113 | **148** | 28 | **289** |
| **10** | -267 | -115 | **152** | 40 | **307** |
| **11** | -268 | -109 | **159** | 59 | **327** |

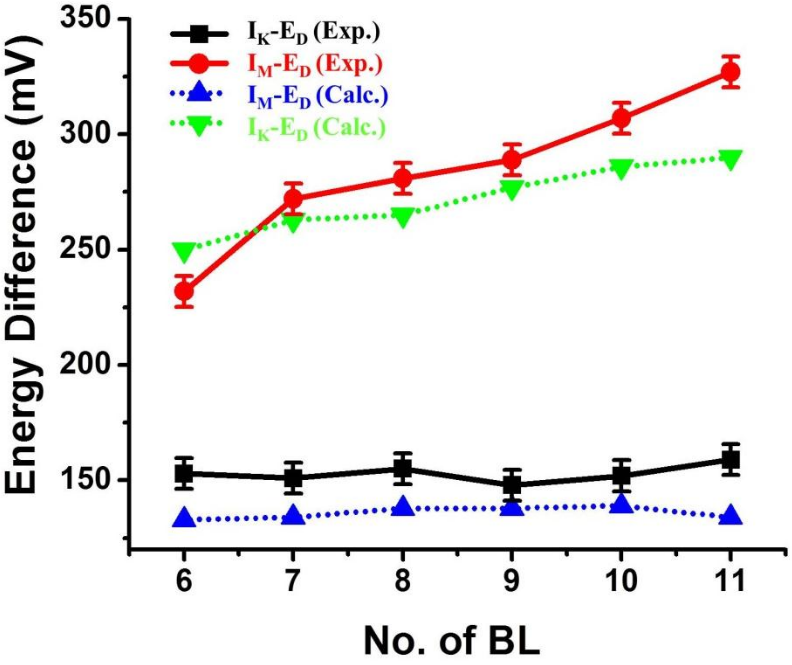

**Fig. 4.13** Energy differences as a function of the film thckness derived from Table 4.2.

Additionally, it is worth noting that from the experimental data of ($I_M$ - $E_D$) between 6BL and 7BL, a “jump” can be observed, which is similar to the dramatic change of intensity ratio $I_T/I_H$ between 6BL and 7BL in Section 4.3.3. As a matter of fact, these two results are consistent, because at 6BL, a small value of ($I_M$ - $E_D$) leads to a “quicker” U-turn for the surface band when it leaves $\bar{\Gamma}$ and advances towards the BVB, which indicates the gap is opened further due to the QCE. Fundamentally speaking, the larger gap originates from the stronger overlap of wavefunctions, including the hybridization between those of SSs from two surfaces, which is identical with the enhanced inter-surface coupling effect. From Section 4.3.3 we know the enhanced inter-surface coupling exactly results in a larger $I_T$ and subsequently induces a huge increase in the intensity ratio $I_T/I_H$ at 6BL. Besides, giving the fact that ($I_M$ - $E_D$) increases slowly as the thickness is beyond 7BL, this sudden jump demonstrates again that the 6BL Sb thin film undergoes a significant transition.

Moreover, since the computed values of ($I_M$ - $E_D$) in Fig. 4.13 do not have such phenomenon, which are based on first-principles calculations for free-standing Sb films, the sudden jump may be attributed to the substrate effect. In another word, although Si(111)-√3×√3:Bi-β is quite inert, the SIA[4,7] induced by the substrate is not negligible especially when the Sb film approaches to the 2D limit and becomes as thin as 6BL. An accurate interpretation for the substrate effects requires further investigations by both experiments and calculations.

All in all, in this section, taking the detailed STS spectra on 6-11BL as an example, we clearly observe the subtle evolution of the underlying band structures. Hence, by comparing STS measurements to computational data, we understand the detailed band structure of thin films; while by comparing FT-STS to computational data, we know the spin texture associated with it. Through combination of the two methods in a STM system, a more comprehensive and complete physical picture of the electronic states in Sb(111) thin films can be revealed accordingly.

## 4.4 Conclusions

In this chapter *in-situ* STM/STS studies on the surface of Sb(111) thin films are illustrated. Firstly, a new deposition method for thin film fabrication is developed, making the precise measurements on Sb(111) films possible. Then taking advantage of the FT-STS method, we prove on 9BL Sb thin films, part of SSs degenerate to QWSs and lose their topological properties. The evolutionary transition from TSSs to QWSs is revealed. Furthermore, the thickness-dependent FT-STS patterns are shown, and we explored the key scattering processes on several representative thicknesses, identifying their origins by experimental and computational data. The result demonstrates the competing process between the intra-surface and inter-surface coupling effects. At last, we perform STS measurements from 6BL to 11BL and show the results consistent with first-principles calculations, which reveal the precise changes of band structures in thin films of 6-11BL.

## References

1 Park, K., Heremans, J. J., Scarola, V. W. & Minic, D. Robustness of Topologically Protected Surface States in Layering of $Bi_2Te_3$ Thin Films. *Phys. Rev. Lett.* **105**, 186801 (2010).

2 Kong, D. *et al.* Few-Layer Nanoplates of $Bi_2Se_3$ and $Bi_2Te_3$ with Highly Tunable Chemical Potential. *Nano Lett.* **10**, 2245 (2010).

3 Li, Y. Y. *et al.* Intrinsic Topological Insulator $Bi_2Te_3$ Thin Films on Si and Their Thickness Limit. *Adv. Mater.* **22**, 4002-4007 (2010).

4 Zhang, Y. *et al.* Crossover of the three-dimensional topological insulator $Bi_2Se_3$ to the two-dimensional limit. *Nat. Phys.* **6**, 584-588 (2010).

5 Cho, S., Butch, N. P., Paglione, J. & Fuhrer, M. S. Insulating Behavior in Ultrathin Bismuth Selenide Field Effect Transistors. *Nano Lett.* **11**, 1925-1927 (2011).

6 Wang, G. A. *et al.* Atomically smooth ultrathin films of topological insulator $Sb_2Te_3$. *Nano Res.* **3**, 874-880 (2010).

7 Shan, W. Y., Lu, H. Z. & Shen, S.-Q. Effective continuous model for surface states and thin films of three-dimensional topological insulators. *New J. Phys.* **12**, 043048 (2010).

8 Liu, M. *et al.* Electron interaction-driven insulating ground state in $Bi_2Se_3$ topological insulators in the two-dimensional limit. *Phys. Rev. B* **83**, 165440 (2011).

9 Lu, H. Z., Shan, W. Y., Yao, W., Niu, Q. & Shen, S. Q. Massive Dirac fermions and spin physics in an ultrathin film of topological insulator. *Phys. Rev. B* **81**, 115407 (2010).

10 Sakamoto, Y., Hirahara, T., Miyazaki, H., Kimura, S.-i. & Hasegawa, S. Spectroscopic evidence of a topological quantum phase transition in ultrathin $Bi_2Se_3$ films. *Phys. Rev. B* **81**, 165432 (2010).

11 Zyuzin, A. A., Hook, M. D. & Burkov, A. A. Parallel magnetic field driven quantum phase transition in a thin topological insulator film. *Phys. Rev. B* **83**, 245428 (2011).

12 Jiang, Y. *et al.* Landau Quantization and the Thickness Limit of Topological Insulator Thin Films of $Sb_2Te_3$. *Phys. Rev. Lett.* **108**, 016401 (2012).

13 Linder, J., Yokoyama, T. & Sudbo, A. Anomalous finite size effects on surface states in the topological insulator $Bi_2Se_3$. *Phys. Rev. B* **80**, 205401 (2009).

14 Liu, C. X. *et al.* Oscillatory crossover from two-dimensional to

three-dimensional topological insulators. *Phys. Rev. B* **81**, 041307 (2010).

15 Roushan, P. *et al.* Topological surface states protected from backscattering by chiral spin texture. *Nature* **460**, 1106 (2009).

16 Alpichshev, Z. *et al.* STM Imaging of Electronic Waves on the Surface of $Bi_2Te_3$: Topologically Protected Surface States and Hexagonal Warping Effects. *Phys. Rev. Lett.* **104**, 016401 (2010).

17 Liu, Y. & Allen, R. E. Electronic structure of the semimetals Bi and Sb. *Phys. Rev. B* **52**, 1566-1577 (1995).

18 Bian, G., Miller, T. & Chiang, T. C. Passage from Spin-Polarized Surface States to Unpolarized Quantum Well States in Topologically Nontrivial Sb Films. *Phys. Rev. Lett.* **107**, 036802 (2011).

19 Brewer, P. D., Chow, D. H. & Miles, R. H. Atomic antimony for molecular beam epitaxy of high quality III-V semiconductor alloys. *J. Vac. Sci. Technol. B* **14**, 2335-2338 (1996).

20 Kumar, V. Electronic and atomic stuctures of $Sb_4$ and $Sb^8$ clusters. *Phys. Rev. B* **48**, 8470-8473 (1993).

21 Yan, Z., Kushvaha, S. S., Xiao, W. & Wang, X. S. Different-dimensional structures of antimony formed selectively on graphite. *Applied Physics A: Materials Science & Processing* **88**, 299-307 (2007).

22 Bardotti, L., Jensen, P., Hoareau, A., Treilleux, M. & Cabaud, B. Experimental Observation of Fast Diffusion of Large Antimony Clusters on Graphite Surfaces. *Phys. Rev. Lett.* **74**, 4694-4697 (1995).

23 Wang, X. S., Kushvaha, S. S., Yan, Z. & Xiao, W. Self-assembly of antimony nanowires on graphite. *Appl. Phys. Lett.* **88**, 233105-233103 (2006).

24 Nagao, T. *et al.* Nanofilm allotrope and phase transformation of ultrathin Bi film on Si(111)-7 x 7. *Phys. Rev. Lett.* **93**, 105501 (2004).

25 Yaginuma, S. *et al.* Origin of flat morphology and high crystallinity of ultrathin bismuth films. *Surf. Sci.* **601**, 3593-3600 (2007).

26 Scott, S. A., Kral, M. V. & Brown, S. A. A crystallographic orientation transition and early stage growth characteristics of thin Bi films on HOPG. *Surf. Sci.* **587**, 175-184 (2005).

27 Zhang, H. *et al.* Topological insulators in $Bi_2Se_3$, $Bi_2Te_3$ and $Sb_2Te_3$ with a single Dirac cone on the surface. *Nat. Phys.* **5**, 438-442 (2009).

28 Liu, C.-X. *et al.* Model Hamiltonian for topological insulators. *Phys. Rev. B* **82**, 045122 (2010).

29 Bychkov, Y. A. & Rashba, E. I. Properties of a 2D electron gas with lifted spectral degeneracy. *JETP Letters* **39**, 78-81 (1984).

30 Zhang, P.-F., Duan, W. & Wu, J. Electronic and topological transitions in Sb (111) thin films. *arXiv:1203.3379v2* (2012).

31 Bian, G., Wang, X., Liu, Y., Miller, T. & Chiang, T. C. Interfacial Protection of Topological Surface States in Ultrathin Sb Films. *Phys. Rev. Lett.* **108**, 176401 (2012).

32 Gomes, K. K. *et al.* Quantum imaging of topologically unpaired spin-polarized Dirac fermions. *arXiv:0909.0921v2* (2009).

# Chapter 5

# Enhanced substrate effect: STM investigations of CdSe(0001) polar surfaces

## 5.1 Introduction

In Chap.3, we focused on the upper surface of the studied material, Sb, and analyzed the topological properties of SSs. In Chap.4, besides the upper surface, we investigated the lower surface as well, and explored the inter-surface coupling effect. In this chapter, we dig deeper to study the substrate beneath the studied material, which may influence the physical properties of the upper structure.

### 5.1.1 Substrate effect for 3D TIs

From the viewpoint of applications, it is crucial to reduce the residual bulk carriers in 3D TIs in real devices. Normally there are two ways to realize the reduction. One is achieved by doping, and the other is by using ultrathin TI films to obtain larger surface-to-volume ratio and enhance the contribution of surfaces. In the first approach, hole donors such as Sn and Ca are introduced in 3D TIs to form $Bi_{2-\delta}Sn_{\delta}Te_3$[1] and $Bi_{2-\delta}Ca_{\delta}Se_3$[2]. By changing the doping level systematically, scientists can lower the Fermi energy to lie near the Dirac point. Unfortunately, even if confirmed as bulk insulators by ARPES, TI materials still exhibit finite bulk carriers in transport measurements[3], suggesting an offset between bulk and surface Fermi levels[3,4]. In the second approach, based on the discussion in Chap. 4, in ultrathin films the SIA induced by the substrate might play an important role in determining the physical properties of the material. For Sb(111), we find when it is as thin as 6BL, the substrate effect may be significant. The reason for this extrinsic effect can be found in the effective continuous model behind it. For example, in $Bi_2Se_3$ ultrathin films, in-plane dispersions of SSs can be written as[5,6] :

$$E_{\pm}(k) = E_0 - Dk^2 \pm \sqrt{(v_F \hbar k)^2 + (\frac{\Delta}{2} - Bk^2)^2} \tag{5.1}$$

Here $\Delta$ is the gap size. $B$ and $D$ are parameters used in the model Hamiltonian[7]. Considering the SIA term due to the substrate, an additional electrical potential term "$V$" can be introduced in the model, and thus new dispersions are re-written as[6]:

$$E_{\pm}(k) = E_0 - Dk^2 \pm \sqrt{(\left|\tilde{V}\right| + \sigma v_F \hbar k)^2 + (\frac{\Delta}{2} - Bk^2)^2} \tag{5.2}$$

$\sigma = \pm 1$ represents two opposite spins. Therefore, the Dirac cone from the upper surface is moved upwards while the one from the lower surface is moved downwards, meaning that the degeneracy of two Dirac cones from two SSs is removed by this potential difference due to the substrate. Specifically, for wurtzite (WZ) CdSe, the abundant surface charge on the polar surface (0001) may induce a larger electrical field, subsequently leading to new dispersions of the upper structure much more different from original ones. In this sense, CdSe(0001) may serve as a proper substrate to deposit

Sb or $Bi_2Se_3$ on it, because as an external factor, the enhanced substrate effect induced by the polar surface is worth investigating, which can be manipulated effectively to tune the electronic properties of TIs in order to fabricate the desired devices.

Moreover, using ultrathin $Bi_2Se_3$ films, theoretical studies[8] show that it is possible to obtain 2D quantum spin Hall (2D QSH) states[9-12]. However, the lattice relaxation is non-negligible when the ultrathin film is in vacuum environment, and the QSH state could be changed to ordinary insulator state if the distance between quintuple layers (QLs) are relaxed to be larger. So the proper substrate with larger in-plane lattice constant is highly required to stretch the $Bi_2Se_3$ within the film plane. Since the in-plane lattice constant of $Bi_2Se_3$ is 4.14 Å while that of WZ CdSe is 4.30 Å, it is an ideal substrate for obtain ultrathin $Bi_2Se_3$ without significant relaxation.

### 5.1.2 Lattice Structure of WZ CdSe

As an important II-VI semiconducting compound, bulk CdSe has two kinds of crystal structures in normal conditions: zinc blende (ZB) cubic structure and wurtzite (WZ) hexagonal structure. The former has an ABCABC stacking sequence along the [111] direction while the latter has an ABABAB stacking sequence along the [0001] direction. In nanostructures such as nanocrystals, CdSe is normally in the form of WZ[13]. Particularly, Cd-terminated CdSe is defined as (0001) while Se-terminated CdSe is $(000\bar{1})$. Since the structure of our samples is Cd-terminated WZ, which will be confirmed later, only the schematic structure of WZ (0001) is shown in Fig. 5.1(a), where the lattice constant is marked as well.

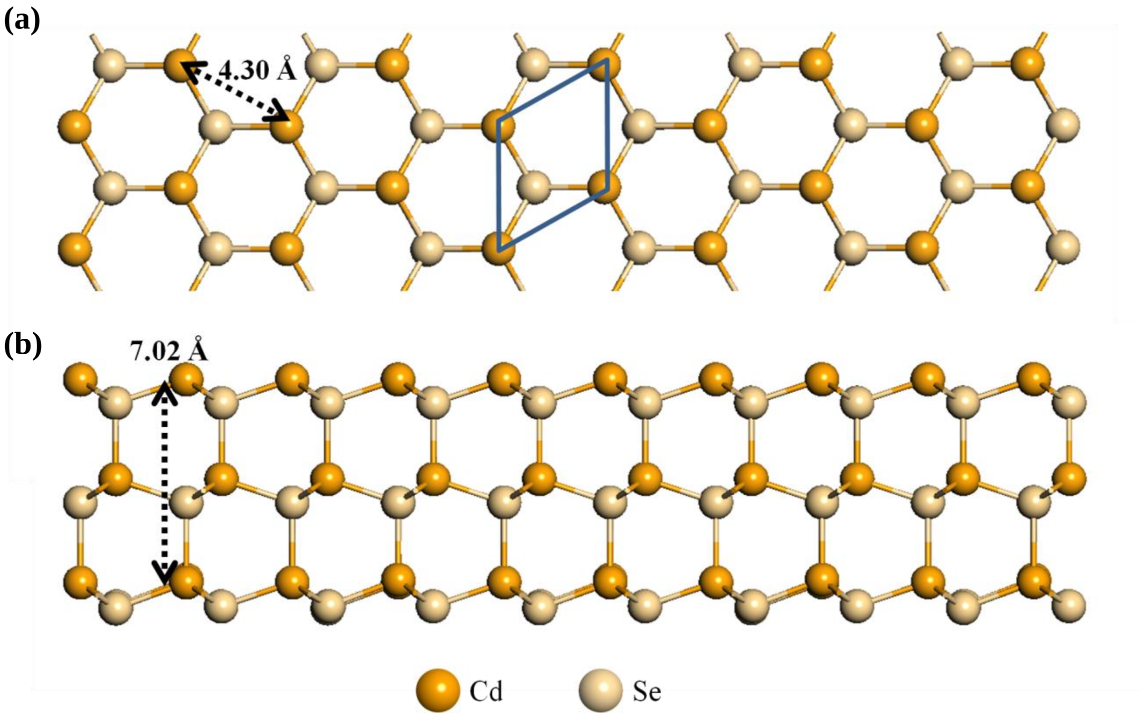

**Fig. 5.1** Structural model of the unreconstructed WZ CdSe crystals **(a)** (0001) **(b)** $(10\bar{1}0)$. $(10\bar{1}0)$ is also the side view of (0001). A unit cell is marked as the blue dimond in (a).

### 5.1.3 Outline

The results of our *in-situ* STM investigations of CdSe films in UHV systems are given in this chapter. In the first part, the growth method for the atomic flat CdSe(0001) films deposited on Si(111)-√3×√3:Bi-β are shown based on a two-step growth procedure. Then the second part will focus on the kinetic growth process of CdSe(0001), and the explanation of the Moiré pattern will be given. At last, a detailed analysis of the surface reconstruction is performed, indicating the Cd-vacancy 2×2 reconstruction is the energetically favorite configuration for this polar surface.

## 5.2 Experimental Method

The experiments were performed in an Omicron multi-chamber UHV system with a RT-STM as well as a Unisoku multi-chamber UHV system with a LT-STM. The base pressure for both systems is $7\times10^{-11}$ Torr. Si(111)-$\sqrt{3}\times\sqrt{3}$:Bi-β serves as the growth substrates. High purity (99.999%) Bi and CdSe were deposited at RT or 200-300 ℃. Before the deposition, both sources were degassed at appropriate temperatures for a few hours in order to remove contamination. The flux was calibrated using AES and STM. STM images were carefully calibrated and the scanner drift was corrected.

## 5.3 Results and Discussion

### 5.3.1 Growth method of CdSe(0001) films

CdSe is an important II-VI semiconducting compound for optoelectronics, and CdSe quantum dots[14-18] have drawn much attention as typical nanostructures to study the QCE. However, up to now, only a few studies can be found in literature studying the growth of single-crystalline CdSe films, especially the (0001) surface. The reason is that different from $(11\bar{2}0)$ or $(10\bar{1}0)$ as shown in Fig. 5.1(b), (0001) is a polar surface due to the atomic architecture. Hence, the atomic arrangements must satisfy the ionic stability, which requires either faceting or surface reconstruction[19] as the most effective approaches. Next we’ll show that by precisely controlling the deposition conditions, both approaches can be realized in the process of formation of CdSe nanostructures. Because of the inertness of Si(111)-√3×√3:Bi-β, the sticking coefficient of Cd and Se on the substrate is lower than that on crystalline CdSe. Therefore, at a fixed beam flux, the substrate temperature must be low for nucleation at the initial stage. After sufficient nucleation, however, the substrate temperature should be increased to improve the film quality. This method is also used in the MBE growth of other compounds[20].

A test was made to explicitly unveil the influence of the initial substrate temperature. Under the same flux of 0.5 ML/min for 10 min deposition onto the same sample, in the one-step method the substrate was kept at 250 ℃ before and during the deposition, while in the two-step method it was kept at RT before the deposition and gradually raised to 250 ℃ in 3 min during the deposition. The formed CdSe nanostructures using the one-step and two-step methods are shown in Fig. 5.2(a) and (b), respectively, with corresponding LEED patterns in Fig. 5.2(c) and (d). The first interesting aspect is that the two-step method obviously provides a better quality of CdSe films. In the one-step method, from Fig. 5.2(a), the coexistence of CdSe 3D clusters (bright and uneven areas) and islands (dark and flat areas) can be found. After measurements, it can be confirmed that the inner and outer sets of hexagonal spots in Fig. 5.2(c) correspond to the lattice of CdSe and Si, respectively. The stronger intensity of the inner set indicates that CdSe nanostructures cover the substrate entirely. Additionally, a very weak 2×2 reconstruction can be seen as well.

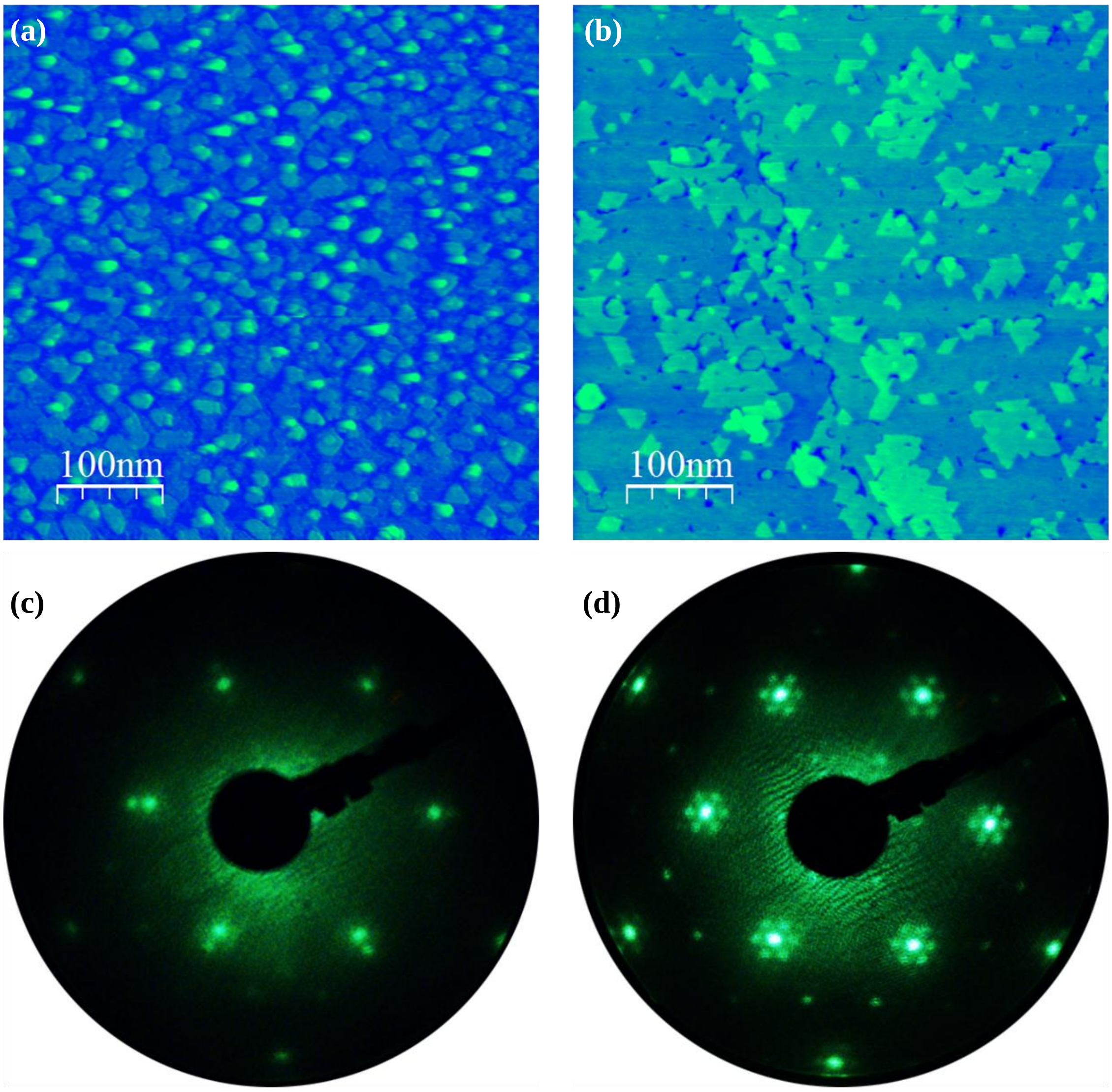

**Fig. 5.2** STM images of CdSe nanostructures on Si(111)-√3×√3:Bi-β using **(a)** one-step and **(b)** two-step method. The corresponding LEED patterns are shown in **(c)** and **(d)**. Clusters and islands can be seen in (a), while flat and uniform films can be seen in (b). Both patterns were taken using an e-beam energy of 56 eV.

In contrast, using the two-step method, we can obtain flat and uniform films. Besides, from the LEED pattern in Fig. 5.2(d), two dramatic changes can be found compared with that in Fig. 5.2(c). One is that six satellite spots show up around the 1×1 spots, which should correspond to a large period (~3.4 nm) in the real space. Later we will confirm it is due to the Moiré pattern between the in-plane lattice of Si and CdSe. The other is that a 2×2 reconstruction appears explicitly in the pattern, while in Fig. 5.2(c) it is very weak. These two kinds of nanostructures also indicate the two ways to satisfy the ionic stability criterion. If large and uniform films form, a net charge has to exist on the polar surface to lower the electrostatic energy, and hence induces a strong surface reconstruction as shown in Fig. 5.2(d). Conversely, in the nanostructures in Fig. 5.2 (a), the ionic requirements are compensated through the formation of small facets, islands and clusters, leading to a much weaker surface reconstruction as shown in Fig. 5.2(c). Interestingly, based on the structural model in Fig. 5.1(b), the unit cell contains two half layers along [0001]. Hence, one half layer is 3.51 Å in height, while the atomic step of Si(111) is 3.14 Å. Due to the quite limited height difference of only 0.37 Å, the half-layered CdSe 2D islands can overcome the substrate step smoothly and form a continuous film as shown in the middle part of Fig. 5.2(b).

In addition, the question whether it is a Se- or Cd-terminated surface can also be solved. The LEED studies[21] and DFT calculations[22] both indicate that $(000\bar{1}) >$ $(0001) > (10\bar{1}0)$ in terms of electrostatic energy. Besides, it was also revealed[22,23] that there is no significant reconstruction on $(000\bar{1})$ while there is 2 × 2 on (0001). Therefore, we can conclude that our sample is (0001), i.e. a Cd-terminated surface.

From the discussion above, we know the two-step growth should be chosen for high-quality CdSe(0001) films. Actually the quality is also determined by both the substrate temperature and the flux. Since LEED patterns are capable of revealing the general quality of CdSe films, based on LEED for total CdSe amounts around 5 ML, Fig. 5.3 gives a statistical result of the deposition outcomes. The red cross represents only Si 1×1 pattern, which indicates only non-crystalline CdSe clusters form. The blue triangle represents the two-set patterns as shown in Fig. 5.2(c), while the green circle represents those in Fig. 5.2(d), corresponding to good CdSe films. To conclude, it can be found that using a flux of 0.5~0.7 ML/min and a two-step substrate temperature raising from RT to 200~300 ℃, the flat and uniform CdSe(0001) films can be obtained.

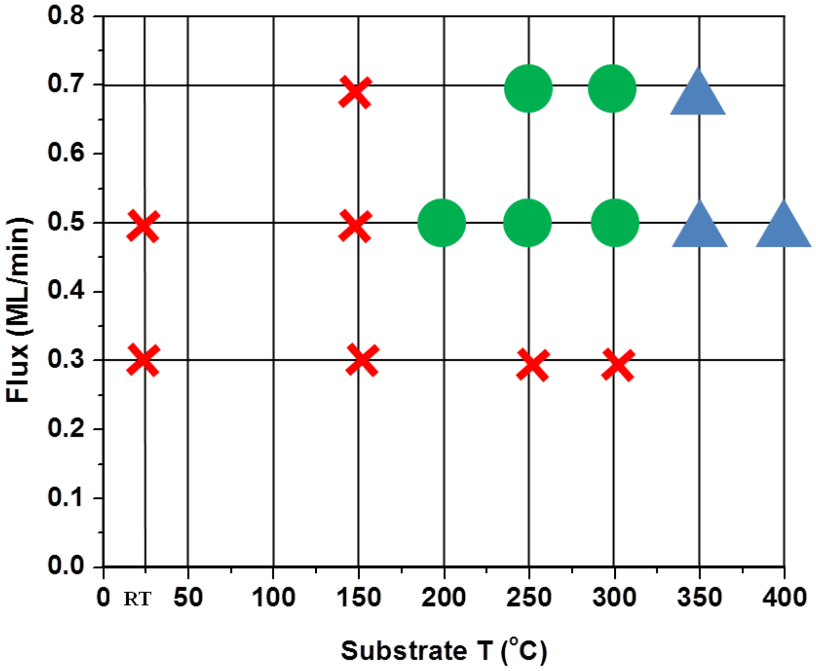

**Fig. 5.3** Statistical LEED patterns as a function of the flux and substrate temperature. The red cross represents only Si 1×1 structure. The blue triangle represents two-set patterns, and the green circles represent that with CdSe 2×2 and the Moiré pattern.

### 5.3.2 Kinetic growth process of CdSe(0001) films

Based on the growth strategy mentioned above, a detailed deposition process will be given below, with a flux of 0.5 ML/min and two-step substrate temperature from RT to 250 ℃. Specifically, as a compound material, CdSe has the stoichiometric issue between the two elements. Therefore, the analysis of the composition is necessary. Based on AES measurements focused on Si, Se and Cd, Table 5.1 gives the peak height ratio of $I_{Si}/I_{Se}$ and $I_{Cd}/I_{Se}$ as a function of the deposition time. Then the result is plotted in Fig. 5.4. Due to the surface sensitivity of AES mesurements, the decreasing ratio of $I_{Si}/I_{Se}$ indicates the Se molecules accumulate on the substrate as the depisition amount increases. Interestingly, the ratio of $I_{Cd}/I_{Se}$ is not constant, and has an increasing trend as the deposition increases. Compared with a bulk CdSe sample which yields the ratio 25.11% of $I_{Cd}/I_{Se}$, it can be concluded that after 10 min (~5 ML) deposition, our CdSe nanostructures are very close to be stoichiometric. It is also worth noting that at a lower coverage initially, there is even no signal of Cd, demonstrating that Se dominates the nucleation at first, and might form a wetting layer for the subsequent CdSe nanostructures.

**Table 5.1** Peak ratio of $I_{Si}/I_{Se}$ and $I_{Si}/I_{Se}$ vs. CdSe deposition time.

| **Deposition time (min)** | **1** | **2** | **4** | **6** | **8** | **10** |
|---|---|---|---|---|---|---|
| **$I_{Si}/I_{Se}$ (%)** | **274.73** | **155.04** | **53.82** | **49.60** | **45.64** | **15.24** |
| **$I_{Cd}/I_{Se}$ (%)** | **0.00** | **0.00** | **11.54** | **12.29** | **19.84** | **20.00** |

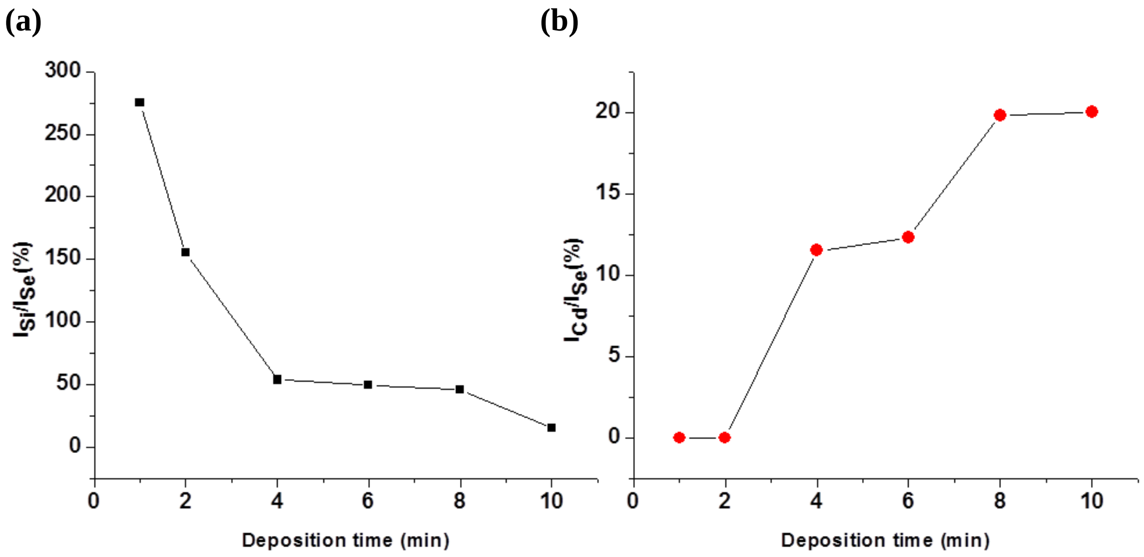

**Fig. 5.4** Peak ratio of **(a)** $I_{Si}/I_{Se}$ and **(b)** $I_{Si}/I_{Se}$ as a function of the deposition time derived from Table 5.1.

The initial stage of nucleation can be revealed in detail by the STM image in Fig. 5.5(a) and the corresponding LEED pattern in Fig. 5.5(c), both taken after 1 min deposition. The amorphous structure formed by Se covers the substrate uniformly, acting as the wetting layer for further growth of CdSe. Indeed, very small triangular islands of height 3.5 Å appear, which correspond to a half-layered CdSe(0001). However, the coverage of these crystalline 2D islands is limited, and thus only six spots of Si lattice can be seen in the LEED pattern in Fig. 5.5(c). Besides, although very weak, the √3×√3 reconstruction of Bi is still present, indicating that there is no significant reaction between Se and Bi atoms when the substrate temperature is still low. Then upon a 1-min additional deposition, islands of two kinds of height, 7.0 Å (1 ML) and 1.40 nm (2 ML), form on the wetting layer, which are shown as the brighter and darker regions in Fig. 5.5(b). Additionally, different from Fig. 5.5(c), here in Fig. 5.5(d) very weak spots can be seen inside the Si spots. After measurements, they can be assigned to the in-plane lattice of CdSe(0001), which originates from the single crystalline islands as shown in Fig. 5.5(b).

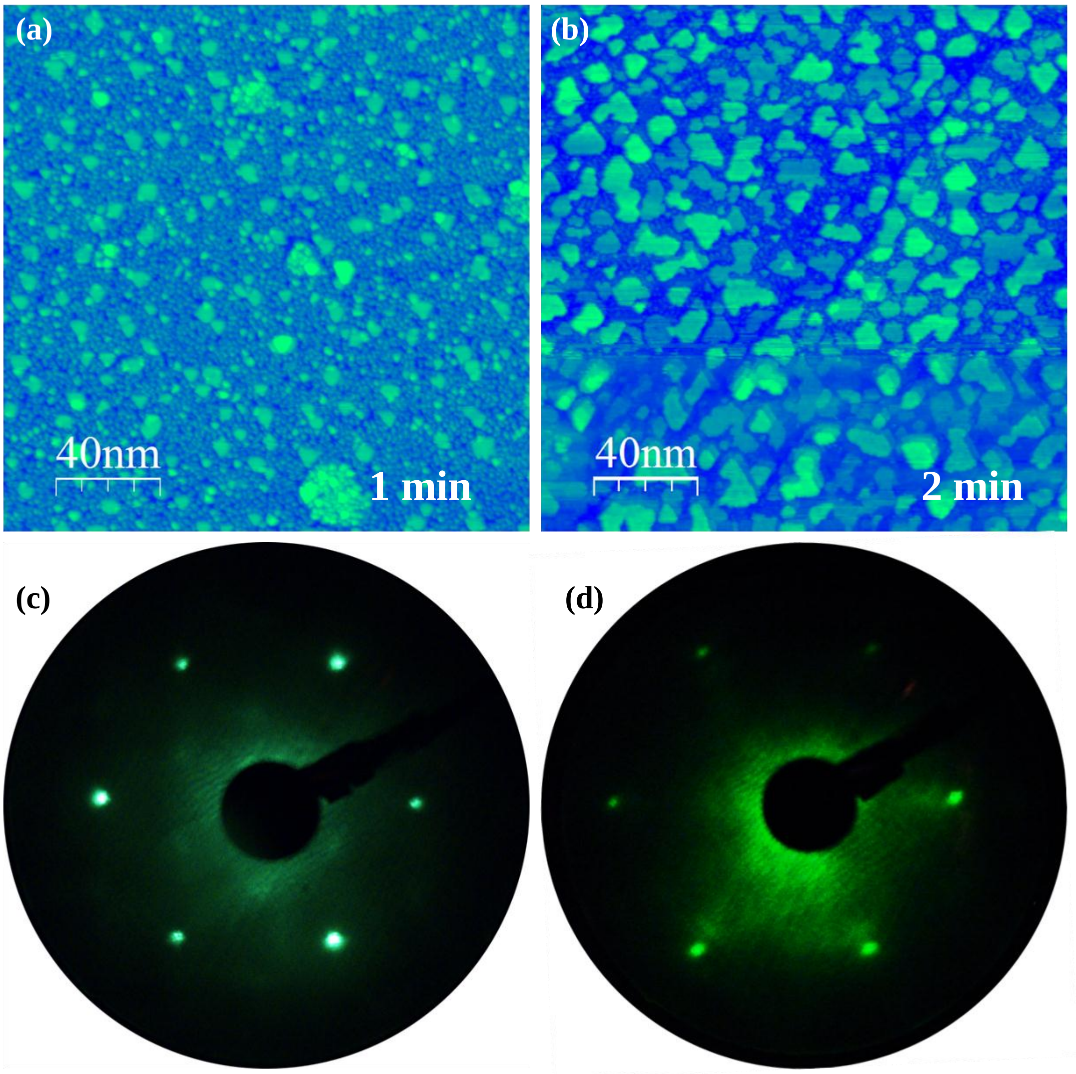

**Fig. 5.5** STM images of the initial stage of CdSe deposition on Si(111)-√3×√3:Bi-β. **(a)** 1-min deposition and **(c)** the corresponding LEED pattern. **(b)** 2-min deposition and **(d)** the corresponding LEED pattern. Both patterns were taken using an e-beam energy of 47 eV.

More deposition needs to be performed subsequently to unveil the process of film formation. So the gradually increasing deposition is shown in Fig. 5.6(a-d). From these STM images, it can be clearly found that upon 4-min (~2 ML) deposition [Fig. 5.6(a)], the first layer of CdSe becomes continuous, above which many triangular islands form. Then the film grows thicker step by step [Fig. 5.6(b-d)] with fewer defects such as holes, which have a depth of 7.0 Å corresponding to the normal thickness of 1 ML CdSe(0001). Since the film quality is improving progressively, the 2×2 reconstruction and even the Moiré pattern become clearer in LEED as shown in Fig. 5.2(d). Till now, a very likely scenario for the CdSe(0001) film formation is that at first when the substrate temperature is still low, due to the relatively large electronegativity, Se tends to remain on the Bi terminated surface rather than Cd, forming a wetting layer for further nucleation of CdSe. Then small CdSe islands appear, and increase in both area and number. As the substrate temperature becomes higher, they connect to each other and expand to form continuous films. Finally the subsequent growth is epitaxial, so the film quality is improved gradually, following the layer-by-layer growth mode.

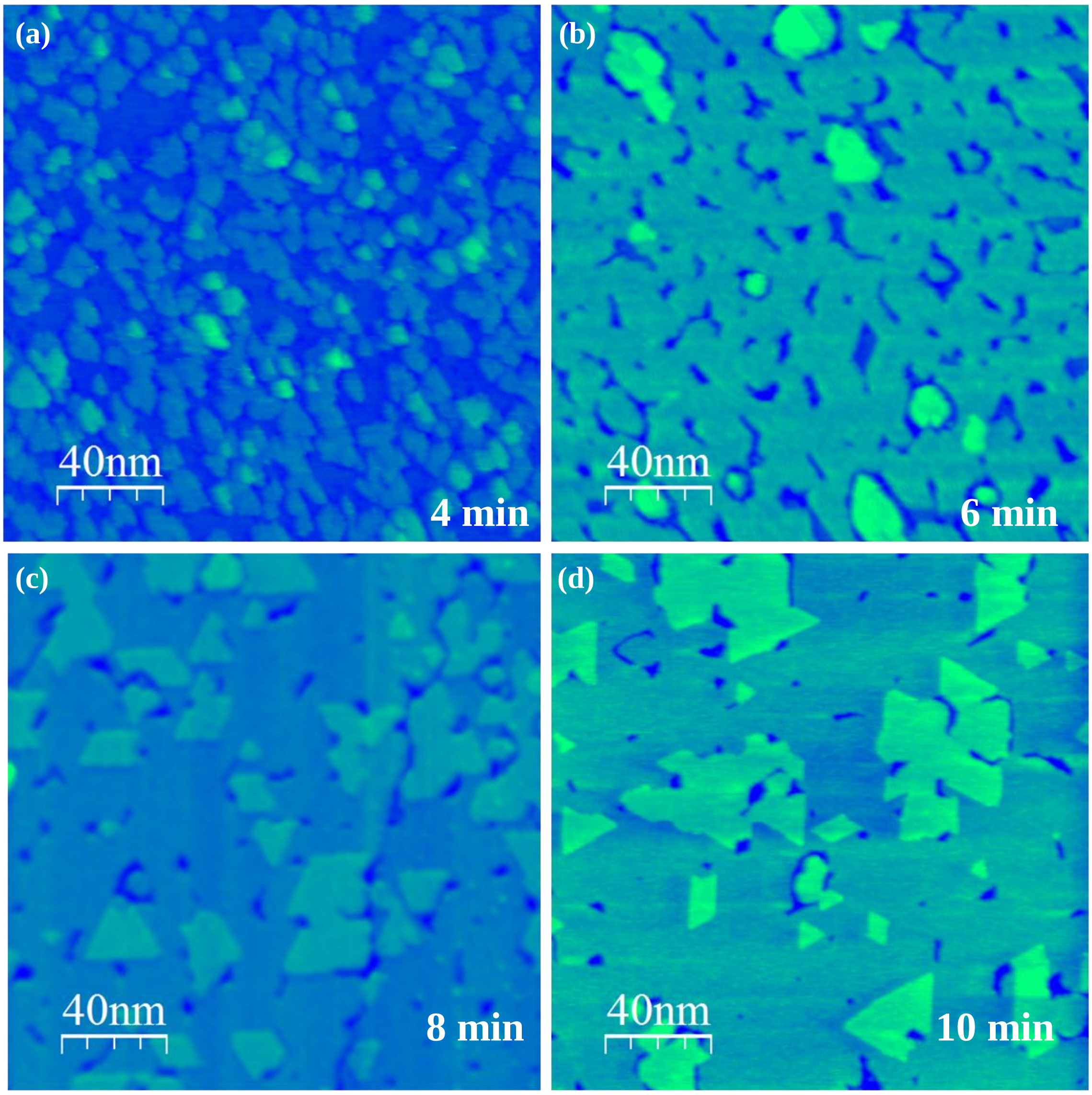

**Fig. 5.6** STM images of gradually increasing CdSe deposition on Si(111)-√3×√3:Bi-β for **(a)** 4 min, **(b)** 6 min, **(c)** 8 min and **(d)** 10 min.

Moreover, since the in-plane lattice constants are different for Si(111) and CdSe(0001), the unstrained lattices should build a Moiré pattern. Indeed, on 5 ML CdSe(0001), choose a flat area marked as the white square in Fig. 5.7(a), and we can obtain an STM image containing both the atomic structure and the Moiré pattern as shown in Fig. 5.7(b). It can also be confirmed by FFT [Fig. 5.7(c)] of the real space image, explicitly illustrating two hexagonal patterns, where the outer one is from the atomic arrangement while the inner one is due to the Moiré pattern. The real space period of the Moiré pattern is 3.43 nm here, which is comparable with the data obtained in the LEED pattern in Fig. 5.2(d). Besides, through a simple calculation the periodicity of the Moiré pattern can be obtained. The superposition of DOS from atoms of both the substrate and the upper structure can provide a stronger current signal for STM to detect, and the overlap takes place at a periodicity of "*d*". From the LEED pattern it can be determined that there is no misorientation angle between the two lattices, so $d \approx (n+1)a_{Si} \approx na_{Cd}$, and $n$ means numbers of atoms while $a$ is the lattice constant. Obviously, we get $9a_{Si} \approx 8a_{Cd,}$ yielding the periodicity $d \approx$ 3.46 nm, which is consistent with the measured value. Because the calculation assumes lattice constants are not relaxed, the agreement with experimental data also indicates that there is no significant strain in the studied system. Besides, the schematic of the formation of the Moiré pattern is shown in Fig. 5.7(d), where Cd atoms (marked as red balls) are on top. Obviously, the geometric overlap between two in-plane hexagonal lattices appears in red zones, giving a stronger tunneling current in that area.

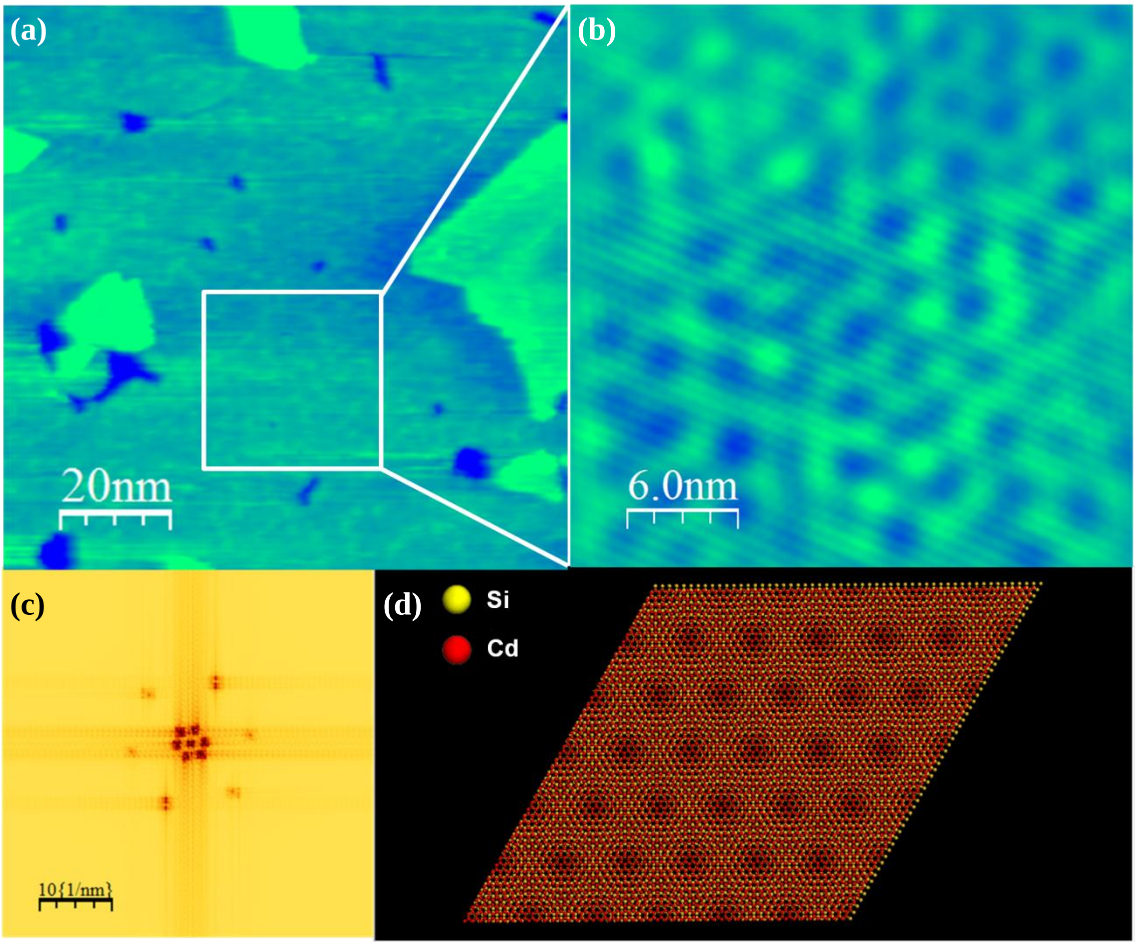

**Fig. 5.7 (a)** A 100 nm × 100 nm STM image of the surface on 5 ML CdSe(0001). **(b)** STM image of the flat area in the white square in (a) shows both the atomic resolution and the Moiré pattern. **(c)** FFT of the real space image in (b). Two sets of hexagonal patterns can be seen. **(d)** Schematic of the Moiré pattern in real space. Cd atoms on top are marked as red balls while Si atoms below are yellow ones.

### 5.3.3 Surface reconstruction of CdSe(0001) films

The 2×2 reconstruction of CdSe(0001) has been well studied by both DFT calculations[22,24,25] and LEED experiments[21,23,26,27]. Nevertheless, unlike neutral surfaces

$(10\bar{1}0)$ and $(11\bar{2}0)$ [28-30], no STM image of (0001) or the reconstruction on that have been reported so far. Since our sample is of good quality, the atomic resolution images on 10ML CdSe(0001) can be obtained as shown in Fig. 5.8(a-b). Interestingly, from the filled state image in Fig. 5.8(a), the 2×2 reconstruction marked as the yellow diamonds, as well as the 1×1 inside the unit cell can both be clearly observed, while from the empty state image in Fig. 5.8(b), only 2×2 reconstruction is observable, probably due to the merging of LDOS from atoms nearby at this energy.

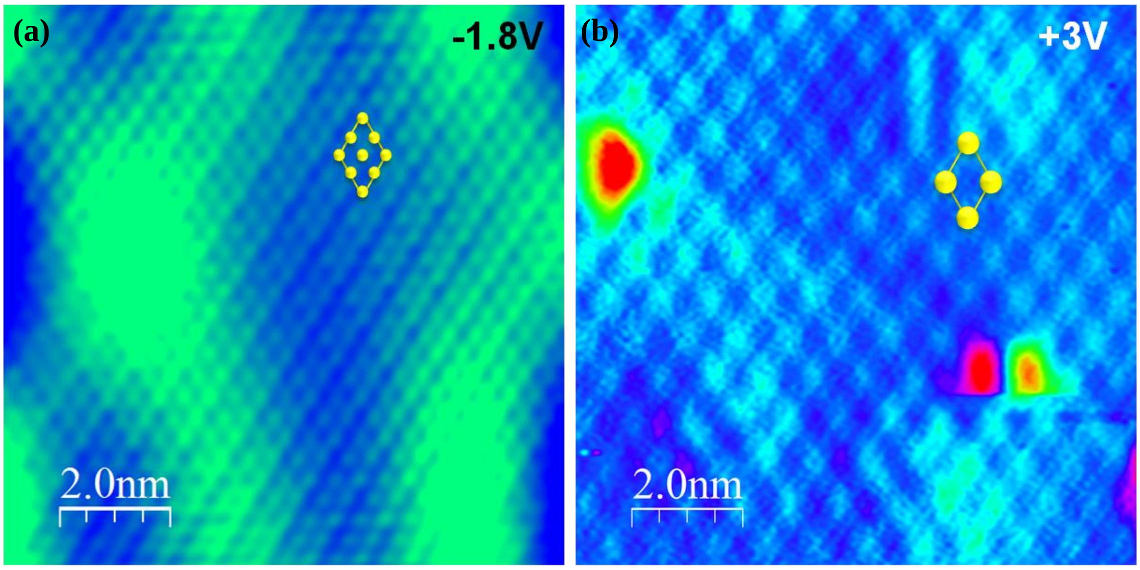

**Fig. 5.8** 10 nm × 10 nm atomic resolution images on 10 ML CdSe(0001) surface. Imaging conditions: (a) $V_{bias}$= -1.8V, I=50pA. (b) $V_{bias}$= 3.0V, I=50pA. Yellow diamonds represent 2×2 unit cells. Yellow balls are used to mark the strong DOS.

The reason for this specific reconstruction can be explained by the electron counting rule as described in previous reports[25,31-33]. In order to simplify the problem, one 1×1 unit cell of (0001) as shown in Fig. 5.1(a) can be considered to possess one dangling bond due to Cd, since one Cd atom needs to form four bonds with neighboring Se atoms using two electrons. Hence one unit cell has ½ surface electron. In this sense, a 2×2 cell should have 4×½= 2 electrons, which is an even number and are more suitable to interpret the reconstruction. Based on the electron counting rule, one vacancy of Cd needs to be introduced in a 2×2 cell, and the three newly-formed Se dangling bonds due to the vacancy can be exactly compensated by the three remaining Cd atoms, making the surface energetically stable.

Then Mr. Luo Ziyu and Mr. Zhou Miao performed the first-principles electronic structure calculations based on DFT using the VASP package[34] with a plane wave basis and a 5 × 5 ***k***-point sampling of the Brillouin zone. In all calculations, GGA in PBE format[35] was included. A supercell that includes 2 × 2 unit cells of CdSe(0001) with periodical boundary conditions and a vacuum region of 10 Å along the [0001] direction were employed. The optimized geometry of Cd-vacancy 2×2 reconstructed (0001) surface is shown in Fig. 5.9(a-b). The 2×2 unit cell is marked as the blue diamond in Fig. 5.9(a), and the Cd vacancy in the center is labeled by the dash line circle.

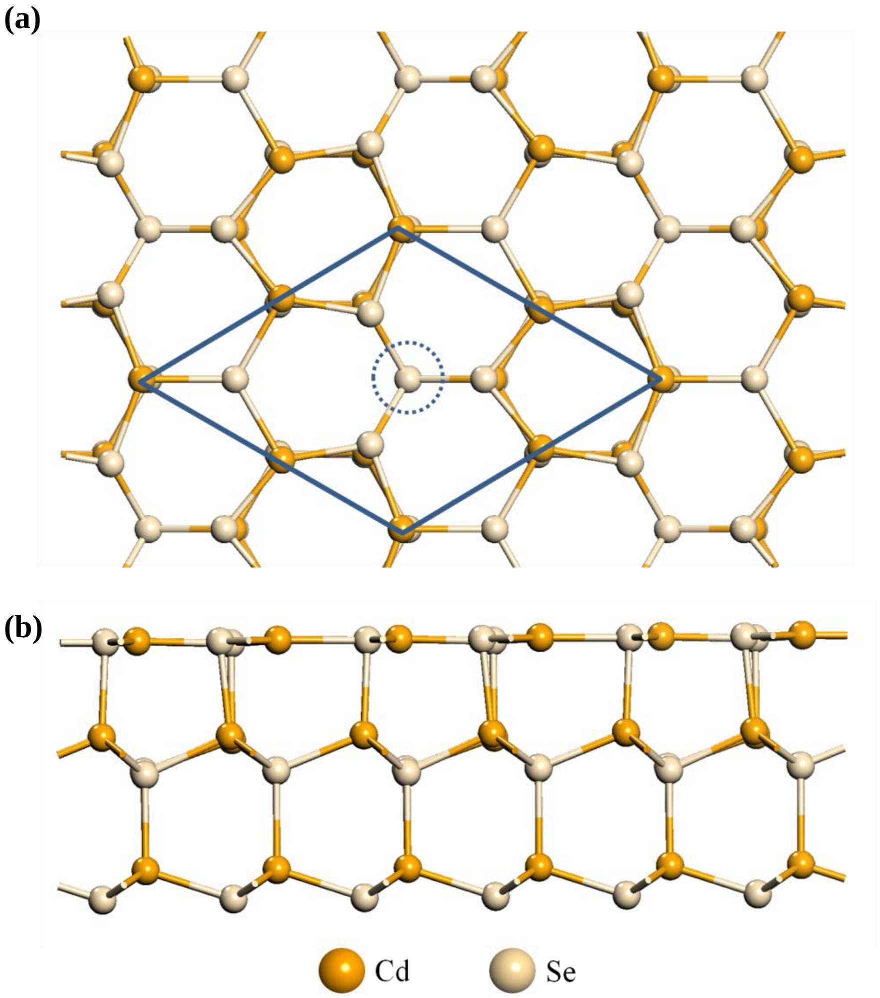

**Fig. 5.9** Optimized geometry of Cd-vacancy 2×2 reconstruction on (0001). **(a)** The top view of (0001) reconstructed surface and **(b)** the side view from $(10\bar{1}0)$. The Cd vacancy in the center is labeled by the dash line circle in (a).

Moreover, based on the relaxed structure above, the simulated STM image can be obtained as shown in Fig. 5.10(a), which can reflect the real space distribution of DOS generated by the atoms on the surface. The blue areas in Fig. 5.10(a) represent the locations of stronger DOS, which agree well with the experimental image (5 nm × 5 nm) shown in Fig. 5.10(b). For comparison, yellow 2×2 unit cells are drawn in both images.

Particularly, along the $[10\bar{1}0]$ direction as marked by the arrows, remarkable similarity can be found. For instance, in the 2×2 unit cell, red arrows in Fig. 5.10(a-b) point to the area of weak DOS, while black arrows mark the area of stronger DOS, which can be distinguished by the color brightness in both images.

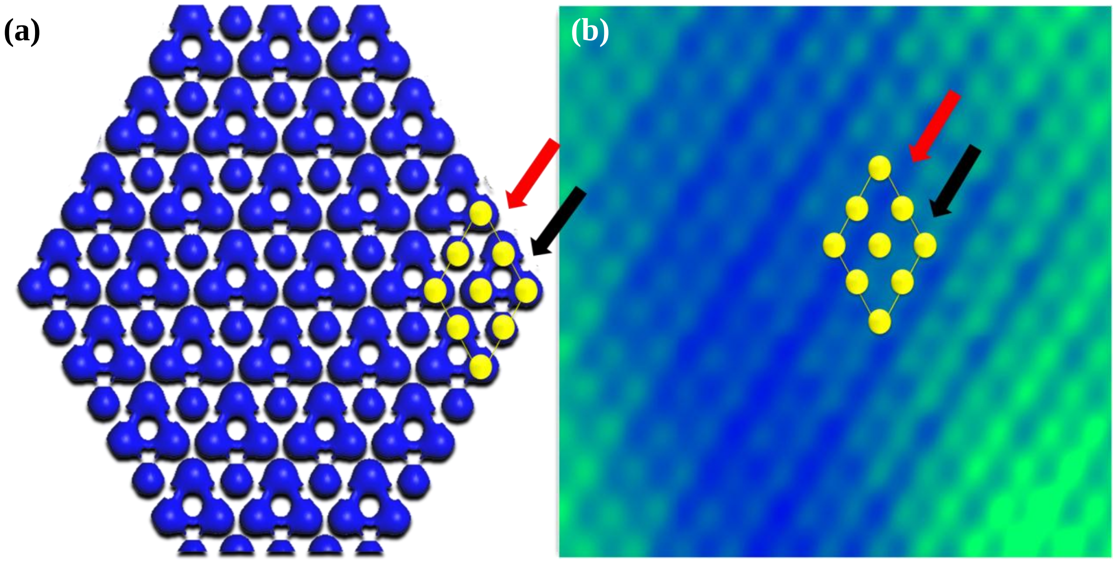

**Fig. 5.10 (a)** Simulated STM image based on the optimized geometry of Cd-vacancy 2×2 reconstruction. **(b)** Experimental STM image (5 nm × 5 nm). 2×2 unit cells are marked by yellow diamonds.

To conclude, this section illustrates detailed analysis of the Cd-vacancy 2×2 reconstruction on the CdSe polar surface (0001). Using STM, the real space surface structure is revealed for the first time. Besides, by employing DFT calculations, the stable configuration can be found, and good agreement between simulated and real STM images is established.

## 5.4 Conclusions

The kinetic growth process of II-VI semiconductor CdSe on Si(111)-√3×√3:Bi-β surface is studied using AES, LEED and STM. Atomically smooth and single crystalline WZ CdSe(0001) films can be obtained by physical vapor deposition in ultra high vacuum conditions. A growth model can be developed which illustrates that Se atoms acting as the wetting layer, dominate the initial stage, and subsequently CdSe grows in the layer-by-layer mode along [0001] direction. Besides, detailed measurements on the reconstruction of (0001) surfaces are performed, revealing the well-known 2×2 reconstruction by STM for the first time, which is in good agreement with our theoretical calculations. The high-quality film has great potential in optoelectronic devices, and might serve as an interesting substrate for TIs such as Sb and $Bi_2Se_3$ due to its largely polar surface.

# References

1 Chen, Y. L. *et al.* Experimental Realization of a Three-Dimensional Topological Insulator, $Bi_2Te_3$. *Science* **325**, 178-181 (2009).

2 Hsieh, D. *et al.* A tunable topological insulator in the spin helical Dirac transport regime. *Nature* **460**, 1101-1105 (2009).

3 Analytis, J. G. *et al.* Bulk Fermi surface coexistence with Dirac surface state in $Bi_2Se_3$ : A comparison of photoemission and Shubnikov-de Haas measurements. *Phys. Rev. B* **81**, 205407 (2010).

4 Qi, X.-L. & Zhang, S.-C. Topological insulators and superconductors. *Rev. Mod. Phys.* **83**, 1057-1110 (2011).

5 Lu, H. Z., Shan, W. Y., Yao, W., Niu, Q. & Shen, S. Q. Massive Dirac fermions and spin physics in an ultrathin film of topological insulator. *Phys. Rev. B* **81**, 115407 (2010).

6 Shan, W. Y., Lu, H. Z. & Shen, S.-Q. Effective continuous model for surface states and thin films of three-dimensional topological insulators. *New J. Phys.* **12**, 043048 (2010).

7 Zhang, H. *et al.* Topological insulators in $Bi_2Se_3$, $Bi_2Te_3$ and $Sb_2Te_3$ with a single Dirac cone on the surface. *Nat. Phys.* **5**, 438-442 (2009).

8 Liu, C. X. *et al.* Oscillatory crossover from two-dimensional to three-dimensional topological insulators. *Phys. Rev. B* **81**, 041307 (2010).

9 Kane, C. L. & Mele, E. J. $Z_2$ topological order and the quantum spin Hall effect. *Phys. Rev. Lett.* **95**, 146802 (2005).

10 Kane, C. L. & Mele, E. J. Quantum Spin Hall Effect in Graphene. *Phys. Rev. Lett.* **95**, 226801 (2005).

11 Bernevig, B. A. & Zhang, S. C. Quantum spin Hall effect. *Phys. Rev. Lett.* **96**, 106802 (2006).

12 Bernevig, B. A., Hughes, T. L. & Zhang, S. C. Quantum spin Hall effect and topological phase transition in HgTe quantum wells. *Science* **314**, 1757-1761 (2006).

13 Katari, J. E. B., Colvin, V. L. & Alivisatos, A. P. X-ray Photoelectron-Spectroscopy of CdSe Nanocrystals with Applications to Studies of the Nanocrystal Surface. *J. Phys. Chem.* **98**, 4109-4117 (1994).

14 Marx, E., Ginger, D. S., Walzer, K., Stokbro, K. & Greenham, N. C. Self-assembled monolayers of CdSe nanocrystals on doped GaAs substrates.

*Nano Lett.* **2**, 911-914 (2002).

15 Walzer, K., Marx, E., Greenham, N. C. & Stokbro, K. Scanning tunneling spectroscopy of CdSe nanocrystals covalently bound to GaAs. *Surf. Sci.* **532**, 795-800 (2003).

16 Bernard, R. *et al.* Ultrahigh vacuum deposition of CdSe nanocrystals on surfaces by pulse injection. *J. Phys.: Condens. Matter* **16**, 7565-7579 (2004).

17 Bernard, R., Comtet, G., Dujardin, G., Huc, V. & Mayne, A. J. Imaging and spectroscopy of individual CdSe nanocrystals on atomically resolved surfaces. *Appl. Phys. Lett.* **87**, 053114 (2005).

18 Antonov, V. N., Swaminathan, P., Soares, J., Palmer, J. S. & Weaver, J. H. Photoluminescence of CdSe quantum dots and rods from buffer-layer-assisted growth. *Appl. Phys. Lett.* **88**, 3 (2006).

19 Nosker, R. W., Mark, P. & Levine, J. D. Polar surfaces of wurtzite and zincblende lattices. *Surf. Sci.* **19**, 291-317 (1970).

20 Jiang, Y. *et al.* Fermi-Level Tuning of Epitaxial $Sb_2Te_3$ Thin Films on Graphene by Regulating Intrinsic Defects and Substrate Transfer Doping. *Phys. Rev. Lett.* **108**, 066809 (2012).

21 Chung, M. F. & Farnsworth, H. E. Investigations of surface stability of II-VI wurtzite compounds by LEED. *Surf. Sci.* **22**, 93-110 (1970).

22 Rempel, J. Y., Trout, B. L., Bawendi, M. G. & Jensen, K. F. Properties of the CdSe(0001), (000-1), and (11-20) Single Crystal Surfaces: Relaxation, Reconstruction, and Adatom and Admolecule Adsorption. *J. Phys. Chem. B* **109**, 19320-19328 (2005).

23 Takahashi, T. & Ebina, A. Electronic surface states of II-VI compound semiconductors. *Appl. Surf. Sci.* **11-12**, 268-287 (1982).

24 Rempel, J. Y., Trout, B. L., Bawendi, M. G. & Jensen, K. F. Density Functional Theory Study of Ligand Binding on CdSe (0001), (000-1), and (11-20) Single Crystal Relaxed and Reconstructed Surfaces: Implications for Nanocrystalline Growth. *J. Phys. Chem. B* **110**, 18007-18016 (2006).

25 Manna, L., Wang, L. W., Cingolani, R. & Alivisatos, A. P. First-principles modeling of unpassivated and surfactant-passivated bulk facets of wurtzite CdSe: A model system for studying the anisotropic growth of CdSe nanocrystals. *J. Phys. Chem. B* **109**, 6183-6192 (2005).

26 Campbell, B. D. & Farnsworth, H. E. Studies of structure and oxygen adsorption of (0001) CdS surfaces by LEED. *Surf. Sci.* **10**, 197-214 (1968).

27 Ebina, A. & Takahashi, T. Studies of clean and adatom treated surfaces of II-VI compounds. *J. Crystal Growth* **59**, 51-64 (1982).

28 Siemens, B., Domke, C., Ebert, P. & Urban, K. Electronic structure of wurtzite II-VI compound semiconductor cleavage surfaces studied by scanning tunneling microscopy. *Phys. Rev. B* **56**, 12321-12326 (1997).

29 Siemens, B., Domke, C., Ebert, P. & Urban, K. Steps on CdSe (11-20) and (10-10) cleavage surfaces: Evidence for crack propagation in competing cleavage planes. *Phys. Rev. B* **59**, 3000-3007 (1999).

30 Ebert, P. Nano-scale properties of defects in compound semiconductor surfaces. *Surf. Sci. Rep.* **33**, 121-303 (1999).

31 Duke, C. B. Semiconductor Surface Reconstruction: The Structural Chemistry of Two-Dimensional Surface Compounds. *Chem. Rev.* **96**, 1237-1260 (1996).

32 Srivastava, G. P. Theory of semiconductor surface reconstruction. *Rep. Prog. Phys.* **60**, 561 (1997).

33 Chadi, D. J. Vacancy-Induced 2×2 Reconstruction of the Ga(111) Surface of GaAs. *Phys. Rev. Lett.* **52**, 1911-1914 (1984).

34 Kresse, G. & Furthmüller, J. Efficient iterative schemes for ab initio total-energy calculations using a plane-wave basis set. *Phys. Rev. B* **54**, 11169-11186 (1996).

35 Perdew, J. P., Burke, K. & Ernzerhof, M. Generalized Gradient Approximation Made Simple. *Phys. Rev. Lett.* **77**, 3865-3868 (1996).

# Chapter 6

# Conclusions and outlook

The simplest description for this project can be illustrated as the investigation of a topologically nontrivial film with two surfaces. The upper one is next to vacuum and the lower one is next to the substrate. This substrate-film-vacuum configuration may lead to three interesting research areas. Firstly, when the thick film forms, STM/STS can detect the local electronic properties solely from the upper surface, disregarding the influence of the lower surface or the interface below that. Secondly, when the film is thin enough, the contribution from the lower one becomes significant because the real-space distributions of wavefunctions of the lower SSs are more spread over the whole films and couple easily with those on the upper surface. Therefore, STM/STS can focus on the contribution of both surfaces if relatively inert substrates such as Si(111)-$\sqrt{3}\times\sqrt{3}$:Bi-β are used to obtain the near-freestanding film structure. Thirdly, if we dig deeper, a substrate with a polar surface might also play an important role in determining the physical properties of the film. These three aspects are the three main topics in this dissertation. Here, the thesis is wrapped up by including a summary of the main results as well as some directions for further investigations.

## 6.1 Contributions

Motivated by the unique electronic properties of Sb and its fascinating potential in TI related applications, this thesis mainly addresses the investigation of Sb films on inert Si(111)-√3×√3:Bi-β substrates. Specifically, for thick Sb films (~30BL) which can be treated as a bulk system, due to step edges on the surface, the topological suppression for scatterings between opposite spin directions can be revealed using FT-STS. However, this kind of 1D scattering lacks detailed direction information in momentum space, since it is only capable of detecting the scattering perpendicular to step edges, which corresponds to the $\overline{\Gamma}-\overline{\mathrm{M}}$ direction. In order to obtain the information along $\overline{\Gamma}-\overline{\mathrm{K}}$, the investigation of the 2D scattering via defects on terraces was also performed using FT-STS. We aimed at identifying the origins of distinct scattering channels both along $\overline{\Gamma}-\overline{\mathrm{M}}$ and $\overline{\Gamma}-\overline{\mathrm{K}}$, and thus unveiling the underlying scattering principles. Moreover, DFT simulations of the QPI according to the spin-angle dependence of scattering probability were also given, which are consistent with the experimental results. The agreement indicates that the SSs of Sb(111) are indeed TSSs which possess great backscattering suppression

Besides, the magnetic response of TSSs on Sb(111) is also investigated by depositing magnetic molecules MnPc. It is believed that the locally broken TR symmetry by MnPc should break the spin conservation for scattering events near them, and thus result in scattering patterns which are solely determined by the band structure without the influence of the associated spin texture. However, in our MnPc/Sb(111) system, the scattering patterns were unchanged even in a high coverage magnetic molecular density, indicating that MnPc molecules cannot break the local TR symmetry as expected. This might also be interpreted by the inability of detecting magnetic-impurity-induced backscattering by normal STM as illustrated in some theoretical work.

Besides the topologically nontrivial thick films of Sb(111), thin films are also worth studying because they can be more suitable building blocks than bulk ones in the real device architectures. In this regard, it is significant to investigate whether the topological properties are still valid when the dimensionality is dramatically reduced. However, in terms of Sb(111) growth, there remains some obstacles to obtain ultrathin films. Thus we firstly developed the growth method for Sb(111) ultrathin films using the cracked Sb source, which can generate Sb atoms. The Sb atoms are more suitable for formation of uniform thin films because they have a lower surface mobility to obtain 2D structures than $Sb_2$ and $Sb_4$ molecules in regular sources. Then using the FT-STS method again, we prove that on 9BL Sb thin films, part of SSs degenerate to QWSs and lose their topological properties. This evolutionary ***k***-dependent diminishing process for the spin polarization from $\overline{\Gamma}$ to $\overline{\mathrm{M}}$ is also revealed. Besides, DFT simulations of the QPI are consistent with our experimental observations. Moreover, if we compare the results on 9BLwith those on 30BL, it can be envisaged that this evolutionary process is also thickness-dependent, meaning that SSs of thinner films would give rise to larger QWSs contributions due to stronger inter-surface coupling effect. Therefore, on several representative thicknesses, the evaluation of the ratio between QPI intensities due to QWSs and TSSs was shown. We identified their origins by experimental and computational data. The result demonstrates the competing process between the intra-surface and inter-surface coupling effects, and unambiguously confirms our explanation on the evolutionary process of diminishing spin polarization, not only from $\overline{\Gamma}$ to $\overline{\mathrm{M}}$, but also from thick to thin films. However, because FT-STS measurements focus on the spatial distribution of scatterings and lack the particulars of LDOS, they are incapable of illustrating details of the band structure. Since STS data can give us the energetic distribution of LDOS more precisely, we also performed STS measurements on ultrathin Sb(111) films ranging from 6BL to 11BL, to investigate the subtle evolution of band structures in these films. Additionally, the difference between first-principles calculations for free-standing Sb films and the experimental results on the substrate of Si(111)-√3×√3:Bi-β, was found. It may be attributed to the substrate effect, especially when the Sb film approaches to 2D limit and becomes as thin as 6BL.

To understand the effect of substrate, the growth of CdSe on Si(111)-√3×√3:Bi-β was investigated using LEED and STM, because the charge on the polar surface (0001) may induce a larger electrical field, subsequently leading to new physical properties for the TI materials on top. In this sense, as an external factor, the enhanced substrate effect is worth studying, which can be manipulated effectively to tune the electronic properties of TIs in order to fabricate desired devices. Therefore, the growth method for the atomic flat CdSe(0001) films deposited on Si(111)-√3×√3:Bi-β were shown based on a two-step growth procedure. The kinetic growth process of CdSe(0001), and detailed analysis of the surface reconstruction have been performed, indicating the Cd-vacancy 2×2 reconstruction is the energetically favorite configuration for this polar surface, which might serve as the proper substrate for further investigation of TI materials.

## 6.2 Outlook

The further work in this specific area can proceed in the following directions, which are based on both theoretical and experimental knowledge. Firstly, thinner Sb(111) films are highly required. Due to some theoretical expectations[1,2], some obvious transitions between TI, semimetal and even 2D QSHI may take place if the dimensionality is further reduced. Efforts are still needed to fabricate ultrathin films below 4BL. Secondly, the magnetic impurity induced broken TR symmetry remains as an interesting problem till now[3-5]. Whether the unchanged feature by FT-STS is due to the weak magnetic moment of MnPc or the incapability of normal STM needs further investigations. If the latter is true, the employment of SP-STM is a good solution for better understanding of the principles. Thirdly, in the case of ultrathin Sb(111) films , an accurate interpretation for the substrate effect requires more investigations by both experiments and calculations. Different substrates are needed to compare with the present work. For example, using CdSe polar surfaces might realize the enhanced substrate effect if topologically nontrivial films such as $Bi_2Se_3$ or Sb are deposited on top. Besides, calculated STS spectra may also provide more direct evidence to explain this specific issue by introducing external electric fields across TI film structures, which is an effective simplification for the substrate effect.

## References

1 Zhang, P.-F., Duan, W. & Wu, J. Electronic and topological transitions in Sb (111) thin films. *arXiv:1203.3379v2* (2012).

2 Bian, G., Wang, X., Liu, Y., Miller, T. & Chiang, T. C. Interfacial Protection of Topological Surface States in Ultrathin Sb Films. *Phys. Rev. Lett.* **108**, 176401 (2012).

3 Valla, T., Pan, Z. H., Gardner, D., Lee, Y. S. & Chu, S. Photoemission Spectroscopy of Magnetic and Nonmagnetic Impurities on the Surface of the $Bi_2Se_3$ Topological Insulator. *Phys. Rev. Lett.* **108**, 117601 (2012).

4 Scholz, M. R. *et al.* Tolerance of Topological Surface States towards Magnetic Moments: Fe on $Bi_2Se_3$. *Phys. Rev. Lett.* **108**, 256810 (2012).

5 Honolka, J. *et al.* In-Plane Magnetic Anisotropy of Fe Atoms on $Bi_2Se_3$ (111). *Phys. Rev. Lett.* **108**, 256811 (2012).